SEA ICE THICKNESS AND THE DISTRIBUTION CONTRIBUTING TO THE MASS BALANCE OF THE SOUTHERN OCEAN

by

E. Rachel Bernstein

A thesis submitted to the Faculty of the University of Delaware in partial fulfillment of the requirements for the degree of Master of Science in Geography

Spring 2010

SEA ICE THICKNESS AND THE DISTRIBUTION

CONTRIBUTING TO

THE MASS BALANCE OF THE SOUTHERN OCEAN

by

E. Rachel Bernstein

Approved: _____

Cathleen A. Geiger, Ph.D.
Professor in charge of thesis on behalf of the Advisory Committee

Approved: _____

Tracy L. DeLiberty, Ph.D.
Chair of the Department of Geography

Approved: _____

Nancy M. Targett, Ph.D.
Dean of the College of Earth, Ocean, and Environment

Approved: _____

Debra Hess Norris, M.S.
Vice Provost for Graduate and Professional Education

ACKNOWLEDGMENTS

I would like to thank the members of my thesis committee for all of their help. Over the course of this research, they have provided me with thoughtful comments and constructive criticisms. First, I would like to thank my advisers, Cathy Geiger and Tracy DeLiberty. I have learned so much from them and I am looking forward to working with them in the future. In particular, I would like to thank Dr. DeLiberty for her patience and guidance as I learned to work with the information in the ice charts. I have to give special thanks to my primary adviser, Dr. Geiger, who has spent so much of her time with to help formulate the questions in this thesis and to help me develop the research and technical skills I needed, all via teleconference. I would also like to thank my committee member, Stephen Gaughan, for his help with database management in ArcGIS.

Additionally, I would like to thank the faculty, graduate students, and staff in the Department of Geography. I have to thank the graduate students especially for their guidance, moral support, and friendship.

Finally, I would like to thank my family: my parents, Richard and Ellen Bernstein, who have always motivated and encouraged me; my siblings and their families for always being there when I've needed them; and Hal, for his love and support.

This thesis is partially based upon work supported by the Delaware Space Grant College and Fellowship Program. I would like to thank the program for support from June 2009-August 2010.

TABLE OF CONTENTS

LIST OF TABLES

LIST OF FIGURES

ABSTRACT

Although sea ice concentration, extent, and type can be measured with acceptable accuracy by satellite or airborne remote sensing techniques, sea ice thickness measurements are difficult to obtain accurately, even in situ. Modeling sea ice volume and associated transport requires input data for ice motion, as well as for the distribution of sea ice thickness. There is a need to develop new sea ice models driven by the best available data. The majority of sea ice thickness measurements in the Southern Ocean are derived from drill holes, and more recently upward looking sonar and electromagnetic methods, but these data points are sparse. The most comprehensive sea ice thickness dataset for Antarctic sea ice available to date is the Antarctic Sea Ice Processes and Climate (ASPeCt) program, which includes 23,373 ship-based observations collected over two decades; however, this dataset has spatial and temporal gaps. This thesis uses the ice stage of development records from National/Naval Ice Center (NIC) operational ice charts as a proxy for sea ice thickness from four years (1995-1998). From the sea ice information within the ice charts, ice thickness and volume are derived to produce model-input-ready Southern Ocean sea ice thickness distributions on multiple temporal and regional scales. Evaluation of the basin-wide thickness distribution includes analysis of multiple sea ice thickness calculation methods and an examination of the seasonal and regional patterns of sea ice distribution.

Chapter 1

INTRODUCTION

Sea ice is an integral component of the climate system. Sea ice, as both a sensitive indicator of climate change and a source for positive feedbacks in the climate system, influences ocean and atmosphere temperature and circulation (Henderson-Sellers and McGuffie 1987). Sea ice acts as an ocean insulator (Allison 1997), and it effects the thermohaline circulation (Worby 1999).

U.S. National/Naval Ice Center (NIC) operational ice charts are the product of an inter-agency effort to construct data sources as mission planning and navigation safety aids. NIC operational products have only been marginally utilized for scientific research, and typically in the form of ice edge validation. The purpose for this work is for the first time to convert the chart product into a form suitable to import into models. To do this effectively for diagnostic modeling, the following four-step process is necessary.

1.) A sea ice model framework is developed.

2.) Ancillary data on sea ice motion are formulated as model input.

3.) Extrinsic sea ice properties of thickness and area (in the form of ice concentration and geographic extent from NIC ice charts) are formatted as model input.

4.) Finally, elements one, two, and three are integrated to execute the model.

For this master's thesis, efforts are concentrated on the first three steps with the anticipation that the framework established in the thesis will enable the fourth step as

part of the doctoral dissertation effort. The research outlines the processes of steps one and two which create the model structure. However, the depth of the thesis focuses on step three, the complex issue of incorporating NIC chart sea ice thickness and volume into a format that can be utilized for modeling. The thesis addresses three critical science questions.

1. *How can sea ice thickness information within operational ice charts be reconstructed into a format suitable for scientific numerical modeling studies without losing any of the original content?*

2. *What is the impact of A.)an integrated sea ice thickness distribution instead of the average sea ice thickness on the climatology and the inter-annual variability?, and B.) open water within the ice pack on sea ice thickness records?*

3. *What is the overall implication in terms of quantifying sea ice volume over the entire Southern Ocean?*

In this thesis, chapter 2 is a report on the current state of Southern Ocean sea ice thickness research and sea ice thickness in climate models. Chapter 3 explains the preliminary work completed for the model framework and transport component. Chapter 4 describes the sea ice thickness data. In chapter 5, the first science question is addressed by detailing the methods needed to transform polygonal area NIC ice chart data into a gridded format. In chapter 6, the second science question is examined through a series of comparisons on a weekly and regional scale. Weekly and regional scale volume results are shown in chapter 7. Chapter 8 is a summary of the thesis work and future plans for the dissertation.

The product of this thesis is a model-input-ready sea ice thickness distribution database founded on operational ice chart records. The designed relational database retains the variability and details of the ice charts, so it is expected to continue to benefit researchers with interests in basin-scale sea ice properties and processes.

Chapter 2

LITERATURE REVIEW

This chapter summarizes previous relevant sea ice literature focusing on characteristics and qualities specific to Southern Ocean sea ice, the importance of sea ice thickness, and standards for sea ice records. A brief overview of sea ice physical properties frames the importance and role of sea ice on the planet while a section on Antarctic sea ice emphasizes recent findings specific to the Southern Ocean. The framework for quantifying a sea ice thickness distribution and the importance of including the full distribution in climate models is explained. Sea ice standard observation methods are described and discussed with respect to the goals for this thesis.

2.1 Relevant Sea Ice Properties

Sea ice is an important indicator of climate change. Although sea ice is associated with positive and negative feedbacks, the positive ice-albedo-feedback mechanism is one of the strongest. Bright white snow and ice reflect almost all incident solar radiation and therefore have a high albedo. Formation of snow and ice increases surface, and likely, planetary albedo, which reflects more solar radiation and further decreases temperatures. Conversely, higher temperatures reduce ice cover and lead to increasingly higher temperatures (Henderson-Sellers and McGuffie 1987). Sea ice affects atmosphere-ocean heat and moisture exchange; the insulating blanket of sea

ice restricts heat loss from the warmer ocean to colder atmosphere (Allison 1997). Sea ice freezing and melting influences thermohaline circulation. It rejects salt as seawater freezes, contributes to the mixed layer formation and increases underlying ocean layer density (Worby 1999, Washington and Parkinson 2005).

2.2 Antarctic Sea Ice

Comprehensive climatology studies of Antarctic sea ice are scarce compared to those of the Arctic. In the Northern Hemisphere, ice thickness decreased by over a meter, or 40%, between the 1960s and 1990s (Rothrock et al. 1999), and over the past several decades there has been a definite negative trend in sea ice extent (Parkinson et al 1999). Sea ice behavior and change patterns in the recent past can be useful in determining the influence of sea ice on future climate (Partington et al 2003).

Sea ice in the Antarctic Ocean has some properties which distinguish it from sea ice in the Arctic Ocean. The types of ice that form in each ocean are different because the Arctic is mainly ocean surrounded by land, while the Antarctic is a continent surrounded by ocean. Because of the dissimilar ice formation patterns in the two oceans, and since the oceanic heat flux is larger in the Antarctic, the thickness of first year ice is thinner in the Antarctic. Snow accumulation also tends to be greater in the Antarctic because of snow blowing off the Antarctic continent and snow formation due to the moisture flux from the adjacent ice-free ocean. The thinner ice and greater snow accumulation often lead to an ice cover depressed below sea level (freeboard flooding), which leads to seawater freezing at the surface (Martin 2004). Winds and currents lead to pressure ridging and open water and move ice laterally from areas of freezing to areas of melting (Schmitt et al 2004). The influence of circulation patterns

in the Southern Ocean tends to direct ice northward where it melts in the ice free ocean, which limits multi-year ice formation (Wadhams 2000).

The Antarctic continent with the glacial (land) ice sheet has experienced a documented net warming trend over the last 50 years (Steig et al 2009). However, Southern Ocean sea ice extent and area are experiencing a net areal increase, and no significant net temperature trend has been documented (Cavalieri and Parkinson 2008). Regional climatic changes are occurring in sea ice in the Southern Ocean. Sea ice advance appears to be more sensitive to climate variability than to sea ice retreat. Wind driven sea ice changes are largely responsible for regional sea ice trends (Stammerjohn et al 2008). Polar sea ice transport is directly related to the air-sea heat exchange, ocean salinity variations and changes in surface albedo (Emery et al 1997).

The West Antarctic Peninsula region is the only sector to experience a documented warming trend over the past 50 years linked to anthropogenic climate change (Vaughan et al 2003). Recent studies have shown both surface air temperature and dynamic processes influence the reduction in sea ice. It is important to be able to determine if the changes are dynamically driven or caused by changes in temperature (Massom et al 2008). Despite warming atmosphere and ocean, sea ice is increasing on average. One explanation is convective overturning in the ocean layer under the ice reducing warm ocean waters near the ice layer, but this explanation alone is not sufficient and more research is needed to examine Antarctic sea ice volume changes and causes (Cavalieri and Parkinson 2008).

2.3 Sea Ice Thickness Distribution

Sea ice thickness distribution is important because when the thickness is known, it is also possible to determine the volume (Rothrock 1986). The concept of

the thickness distribution is valuable since the sea ice thickness determines how ice will respond to thermal or mechanical forcing. The ice compressive strength, growth rate, surface temperature, turbulent and radiative atmosphere-ice heat exchange, and salt content are all thickness-dependent (Thorndike et al 1975). The thickness affects (although it is by no means the only determinant) the upper ocean salt balance, productivity by modifying the habitats in which ice biota adapt and grow, light penetration, and components of the surface heat and momentum balance (Rothrock 1986).

Comprehension of ice pack properties thus depends on characterizing the thickness distribution. Thorndike et al. (1975) developed the mathematical framework to examine sea ice thickness distribution of an ice pack. In an area, *R*, the thickness distribution, *g(h)*, is

$$\int_{h_2}^{h_1} g(h)\, dh = \frac{1}{R} A(h_1, h_2) \tag{2.1}$$

Where *h* the thickness of the ice and $A(h_1,h_2)$ is the area of ice covered by ice extent region, *R*. Integrating the thickness distribution, *g(h)* over a thickness range gives the area the ice extent covered by a thickness range, and this is effectively the concentration. The primary equation of the change in the thickness distribution with respect to time is

$$\frac{\partial g}{\partial t} = -\nabla \cdot (\vec{v} g) - \frac{\partial}{\partial h}(f g) + \psi + F_L \tag{2.2}$$

where $\boldsymbol{v}$ is the velocity vector and *vg* is the flux of the thickness distribution. Thus, the rate of change in the thickness distribution, $\frac{\partial g}{\partial t}$, can be related to the divergence of

the flux as given in the first term of the equation. The second term explains the vertical thermodynamics and shows ice thickness changes thermodynamically at a rate of *f* which is dependent on the thickness at a given time and location. The third term describes the redistribution function. Redistribution includes mechanical forcing and the resulting changes to the ice thickness from divergence or ridging. The final term is the lateral melt, which describes that lateral melting is compensated by a change in the extent of the open water and ice area. While all terms in the equation explain the changes in the sea ice thickness distribution, only the growth and melt terms may affect the total volume of ice in a region. The combination of the non-uniform ice motion leading to mechanical processes of ridging and opening of leads and ice deformation caused by thermodynamic process of melt and growth resulting in mass changes in the ocean and atmosphere boundary layers form an ice field without uniform thickness (Thorndike et al 1975, Hibler 1980).

Ice thickness tends to stabilize near the thermodynamic equilibrium when unaffected by other processes, and the mechanical processes lead to extremes of open water and thick ice where the ice would otherwise remain at equilibrium thickness. Thorndike (1992) simplifies the original equation by recognizing that ice thinner than the thermodynamic equilibrium may ridge, and suggesting that the ridging rate is proportional to the deformation intensity. Also, advection may be removed from the terms of the equation by considering the thickness distribution region to be moving with the ice in a Lagrangian frame of reference (Thorndike 1992).

When deformation and growth rate as a function of time are known with an observed thickness distribution initial condition (and lateral melt is ignored), it is possible to project the future thickness distribution. At any given point, the thickness

is random, so it is possible to define a probability function to describe the probability that the thickness will be within a thickness range (Rothrock 1986). The probability function,

$$P = \int_a^b g(h)dh = probability\ that\ a < h < b \tag{2.3}$$

also shows that the mean value of the thickness distribution is explained as the integral of all thickness ranges over the entire area:

$$H = \int_0^\infty hgdh \tag{2.4}$$

This theory provides the foundation for the calculation of mean sea ice thickness (Rothrock 1986), and in this study the mean integrated thickness will be calculated from the sea ice thickness distribution derived from NIC ice charts.

2.4 Sea Ice in Models

Along with the atmosphere, ocean, and land, sea ice is one of the four basic components of climate models. Because of the sea ice properties and their feedbacks, the presence of sea ice in a specific area within a climate model can impact the model output atmospheric and oceanic responses. It is recognized that the ice roughness, open water and thinnest ice, and the ice boundary position are important parameters for climate modeling (Thorndike et al 1975). Hibler (1980) modeled seasonal equilibrium simulations by expanding the Thorndike et al. (1975) sea ice thickness distribution framework and combining it with an ice dynamics model and a mixed ocean layer with a varying surface heat budget. He found that the summer ice edge

and ridging and deformation are substantially linked to the heat exchange, and ice pack characteristics are highly sensitive to external forcing.

Modern climate models continue to focus on the impact of sea ice. The annual cycle of the thickness distribution of Southern Ocean sea ice in the sea ice simulation of the NCAR Community Climate System Model version 3 (CCSM3) has been examined (Holland et al 2006). When the parameterized ice thickness distribution is included, the simulation results in larger ice growth rates and thicker ice. There is also evidence that including the distribution modifies sea ice feedbacks (surface albedo, ice thickness strength and ice thickness growth feedbacks). When the CCSM3 operates with a sea ice thickness distribution, sea ice coverage is specified as sub-grid-scale fractions which represent the concentration of ice within the model's resolution grid. Sea ice thickness ranges plus open water vary over an annual cycle. An investigation of the lag structure across seasons in the sea ice thickness distribution shows that the fraction of the thinner ice categories increases as it gets cooler with the seasons reflecting new ice, but the lag also represents the fact that the thin ice will thicken with time and eventually become a part of a thicker ice category. The thicker ice categories do not show as strong of a lag structure because the thickest categories are primarily formed of multi-year ice and do not noticeably increase over one year. The open water fraction decreases in the early austral fall as the thinnest ice category forms and the thinnest ice category's coverage increases. As the ice continues to form and increase in both fractional coverage and thickness, it eventually becomes part of the second thinnest ice category. This causes the peak concentration in June in the thinnest ice category but a lag showing peak concentration in August for the next thinnest ice category and peak concentration in November for the following (Holland et al 2006).

There is evidence that the sea ice parameterizations in climate models have room for improvement. Strong inconsistencies between the changes in sea ice extent due to greenhouse gas loading in climate models and the observations of sea ice extent have been found (Stroeve et al 2007). The IPCC climate model ensemble mean time series greatly underestimates the observed response in the Arctic ocean. The rate at which the sea ice minimum extent is declining appears to be faster than the rate the models predict. (Stroeve et al 2007). This is still being investigated for the Southern Ocean.

2.5 Sea Ice Thickness Observation and Measurements

Although sea ice extent and concentration data are readily available on a large scale via satellite remote sensing records, accurate, basin-scale sea ice thickness information is sparse. It is fairly simple to take direct measurements of sea ice thickness. A team of researchers located on the ice set up an array of stakes and thickness gauges which can measure ice accumulation and melt, as well as changes in the snow over the ice. Although it is easy to gather these measurements and the equipment and technology has long been available, there are very few observational results available for those requiring broad mass balance field observations. Long term field camps are expensive to construct, and maintenance and operations at a cold weather site add further expense. The expansive areas covered by sea ice in the polar regions adds the complication and expense of more camps. The large area, cold, time, money, and the lack of in-situ measurements becomes less of a problem when using remote sensing to infer sea ice mass balance (Comiso et al 1986).

Satellite remote sensing of sea ice is possible using the visible, infrared (IR), and microwave wavelength ranges, which are chosen based on capabilities and

limitations. In the optical, or visible, spectral range, satellite remote sensing has been used to monitor sea ice for almost four decades. Data from NOAA's Advanced Very High Resolution Radiometer (AVHRR) in the visible and thermal infrared channels, as well as the Moderate Resolution Imaging Spectrometer (MODIS) on Terra and Aqua satellites are used to determine areas of sea ice cover. Detection of ice in the visible range is an indirect method which uses intensity of emitted radiation to detect the contrast of ice and water. Sea ice has a much higher albedo than water, so it is possible to determine sea ice extent from a visible image. Additionally, for sea ice without snow coverage, it is possible to approximate sea ice thickness based on the brightness value of the ice pixel where tonal changes are associated with ice age and thickness values. With these ice and thickness measurements, it is possible to determine total ice concentration, or mass balance. Errors in associating thickness from tone arise from ridges, melting, edges, and snow on the ice (Johannessen et al 2007).

In thermal infrared wavelengths, the difference between the temperature and emissivity of ice and water surfaces allows for the detection of sea ice. Determination of any sea ice characteristic is indirect and found in the same way as with visible wavelengths (Johannessen et al 2007). Although imagery from visible and infrared wavelengths can be a useful supplement for sea ice research, mapping of sea ice thickness from IR images is only possible using cloudless images, and although these images are found infrequently, they are still important for sea ice monitoring (Johannessen et al 2007). Today, remote sensing by imaging radar systems is the most useful method for sea ice observations regionally. For these systems, clouds and time of day have no effect on the utility of the image. Imaging radar is active, so the sensor

emits its own illumination in the microwave range of the electromagnetic spectrum which has several benefits in the polar regions. The wavelengths over 10,000 times longer than those in the visible spectrum penetrate fog, clouds and precipitation frequently over the poles, and, because the sensors are active, they operate independent of daylight, which is particularly important during polar winter. The radar emits electromagnetic energy which strikes the land surface and some of the energy reflected back to the radar sensor where the travel time, amplitude, and phase of the waves are recorded. Radar images are sensitive to surface roughness, detect moisture on the surface, use polarized signals and measure the polarization dependence of the reflected microwave pulse, and have geometric distortions in range (the direction perpendicular to the azimuth or orbit) where the image slopes towards the sensor (Johannessen et al 2007).

Three radar systems are used for sea ice observation: scatterometers, synthetic aperture radar (SAR), and side-looking real aperture radar (SLR). Over the last decade, scatterometer data for ice monitoring has been used over the entire Arctic and Antarctic, but regionally, SAR and SLR tend to be more effective (Johannessen et al 2007). With a higher azimuth resolution and radiometric accuracy, SAR data is the easiest to control, making it the most important system for sea ice observation regionally. In a SAR image, the backscatter value, feature texture, and radar image brightness are all used to determine ice type, form and roughness. With SAR, ice stage of development can be determined, and this can be used as a proxy for sea ice thickness (Johannessen et al 2007).

Among the SAR sensors on satellites today are three systems, which together offer improvements in sea ice monitoring. The European ENVISAT with an advanced

SAR, the Canadian RADARSAT-1 and RADARSAT-2, and the Japanese Advanced Land Observing Satellite which carries PALSAR all carry SAR sensors (Martin 2004). Passive microwave satellite data are effective independent of light and clouds, so the data provides a steady long-term, albeit low spatial resolution, record. With over twenty years of these measurements, the inter-annual variations in sea ice cover may be studied. Due to the variations in ice formation, microwave signatures of sea ice differ between the two locations (Martin 2004). Passive microwave data since 1978 have already shown a decrease in Arctic sea ice extent by 2-3 % per decade, and currently while Antarctic sea ice shows inter-annual and inter-seasonal variability, there is no statistically significant decreasing trend in sea ice extent (IPCC 2007).

Among the passive microwave remote sensing instruments used are the Scanning Multichannel Microwave Radiometer (SMMR) NASA launched in 1978 and the Special Sensor Microwave/Imager (SSM/I) launched in 1987 by the Defense Meteorological Satellite Program. Since then, NASA Goddard Space Flight Center scientists have combined the datasets for a comprehensive 30 year dataset (Cavalieri and Parkinson 2003). The dataset displays the substantial variability in the ice cover in regional, seasonal and inter-annual scales. From the records, 30 year sea ice extent trends have been determined for the Southern Ocean and the Arctic Ocean (Cavalieri and Parkinson 2003), and later extended for the Southern Ocean (Cavalieri and Parkinson 2008).

Although many sensors and techniques to determine sea ice thickness and infer the mass balance from aircrafts and satellites, capabilities exist to remotely sense sea ice thickness closer to the surface. One sensor is the upward looking sonar, which has been used less frequently than its satellite sensor counterparts. In areas where SAR

and AVHRR data provide information on areal distribution of ice properties, upward looking sonar is useful in confirming the presence of certain ice types. The upward looking sonar focuses acoustic pulsed energy into a narrow beam to measure elapsed time between the target and return signal. The threshold is set low enough to determine differences between air, air bubbles, ice, and even sediment and zooplankton. When compared with in-situ measurements and satellite images, the upward looking sonar allows improved data collection (Druker et al 2003).

The goal of remote sensing in sea ice research is to have more accurate, precise, and widespread sea ice thickness data to determine the sea ice mass balance. NASA's ICEsat satellite gathered data which helps to understand changes in sea ice thickness, but the satellite has only collected data from 2003 to 2009. The ICESat mission is first polar orbiting satellite with a laser altimeter which can provide surface elevation of the ice sheets and other surfaces (Schutz et al 2005). NASA is currently planning mission as a follow up called ICESat-II, which will launch in 2015, and in the meantime, the NASA Ice Bridge program will continue to monitor sea ice from aircraft.

The main data source for sea ice thickness from in-situ data around Antarctica comes from the ASPeCt (Antarctic Sea Ice Processes and Climate) program ship observations (Worby et al 2008). This is a dataset of tens of thousands of ship observations over several decades which have been compiled and used to examine the Southern Ocean sea ice thickness distribution. These points are the primary ground truthing points for other large-scale sea ice thickness studies. DeLiberty and others have a manuscript submitted (2010) which examines the sea ice thickness distribution, ice extent, ice area, and ice volume on a regional scale in the Ross Sea. This paper

uses thickness information derived from the NIC ice charts and makes comparisons with the ASPeCt thickness data. These thickness distribution studies provide the framework for the analysis in this thesis.

2.6 In the News

In recent years, the decline of Arctic sea ice extent has concern researchers, policy makers, security analysts, and industry specialists who all wish to determine the impact of diminishing summer sea ice extent in the Arctic. There are political implications (defense, ocean claims), economic pursuits (resource extraction, tourism and shipping potential), social considerations (indigenous peoples way of life), ecological damages (adaptation of polar marine species), and of course, scientific interest. Of particular attention is the 2007 record Arctic sea ice minimum extent attributed in the literature in part to warming temperatures but also to specific changes in ice drift such as the failure for ice arch formation that prevents the passage of sea ice from the Arctic to the Atlantic via the Nares Strait and through the Canadian Archipelago (Kwok et al 2010). Researchers are now attempting to model and predict the potential for an Arctic Ocean free of summer sea ice. IPCC climate models run with the 2007 and 2008 sea ice minimum extents as initial conditions have predicted an ice free Arctic before the end of the century, and potentially within the next 30 years (Wang and Overland 2009). These predictions have wide ranging social implications for groups with Arctic interests.

It is apparent that the sea ice is changing in a way which climate models are not predicting (Stroeve et al 2007). Thus, it will be important in the future to be able to quantify the changes in sea ice extent due to atmosphere and ocean circulation changes

and local effects (ice dynamics) versus those caused by temperature changes (thermodynamics) to enable more accurate future predictions of sea ice. Regardless of the cause of changes in sea ice extent, the effect is the same: thick multi-year sea ice has suffered with the recent loss in sea ice extent in the Arctic, and it will be years before it fully recovers resulting in substantially reduced mass balance and volume of sea ice in the Arctic (Kwok et al 2009). The lesson from analyses of the 2007 summer minimum sea ice record is that an accurate picture of the sea ice characteristics of a static period should account for changes in sea ice thickness, area, extent, volume, and motion. These metrics are necessarily linked. As the ice moves it ridges and rafts in areas where the ice is compressed, while forming open water leads where ice separates, and because thin ice melts more easily and quickly than thick ice, deformation affects thermodynamics.

This model framework developed in this thesis addresses the need for studies which account for changes in sea ice volume, thickness, area, extent, and motion. By tracking sea ice thickness and motion in a diagnostic model, changes in sea ice due to thermodynamics and mechanics are determined, and this process provides a broad view of the Southern Ocean sea ice transport.

Chapter 3

MODEL FRAMEWORK

This chapter describes the model development and progress on the model to the point of integrating sea ice thickness data. The framework for a diagnostic Southern Ocean sea ice volume and transport model is developed for this thesis with the model implemented in future work. The model volume and transport data are prescribed from carefully interpolated and detailed sea ice motion and thickness information. The process of tracking details of volume transport across model grid boundaries allows the determination of the changes in ice volume due to thermodynamic (growth and melt) or dynamic (mechanical redistribution, leads, and ridging) forces. Development of the model framework is explained in the first section. The sea ice drift data and drift data processing are explained in the second and third sections.

3.1 Model Framework and Design in PV-WAVE

The sea ice motion is specified from input drift data, and the sea ice thickness is specified from thickness derived from the NIC sea ice charts. The model framework is used to transform the inputs to a model grid, and then upscale the inputs to a regional grid, and calculate mass balance fluxes between flux gates (simply the boundaries between grid cells). The model is written in three parts: (a) a PV-WAVE code to project, organize, and spatially scale the drift vectors to the model grid; (b)

combinations of Python and PV-WAVE scripts to organize and scale thickness observations; and (c) a final PV-WAVE code to read inputs from the scaled thickness and drift to calculate Southern Ocean sea ice mass balance fluxes. A data file contains the Antarctica coastline coordinates to map for the model.

The model framework creates a grid around the Southern Ocean. This is a circumpolar grid ranging from 74°S to 54°S with cells every 10° longitude by 4° latitude. The large sectors used for regional mass balance flux calculations are demarcated along discrete east-to-west ranges. The sectors follow established regions. Six sectors are commonly used to describe the Southern Ocean sea ice zone: These are the Ross Sea, the Bellingshausen-Amundsen Sea, the Western Weddell, the Eastern Weddell, the Indian Sector, and the Pacific Sector. The Weddell Sea is traditionally broken into two parts because the Western Weddell Sea contains up to 80% of the multiyear ice within the entire sea ice zone around Antarctica. It retains sea ice year round, while the Eastern Weddell Sea exhibits more of a seasonally driven cycle. For this work, the Ross sea is separated into the Eastern Ross Sea tends to have more multiyear- thick ice than the Western Ross Sea so there are a total of seven sectors. These are the Western Weddell Sector from 60°W to 40°W, the Eastern Weddell Sector from 40°W to 20°E, the Indian Sector from 20°E to 90°E, the Pacific Sector from 90° to 160°E, the Eastern Ross Sector from 160°E to 170W°, the Western Ross Sector from 170°W to 130°W, and the Bellingshausen-Amundsen Sector from 130°W to 60°W. A polar stereographic projection with the World Geodetic System 1984 datum is used with 70°S defined as the latitude of true scale where the grid is tangent to the Earth's surface to minimize distortion in the marginal ice zone, and the

0° longitude is the central longitude. The grid and sectors are identified in figure **3.1** with the grid boxes outlined in green and the large sectors in red.

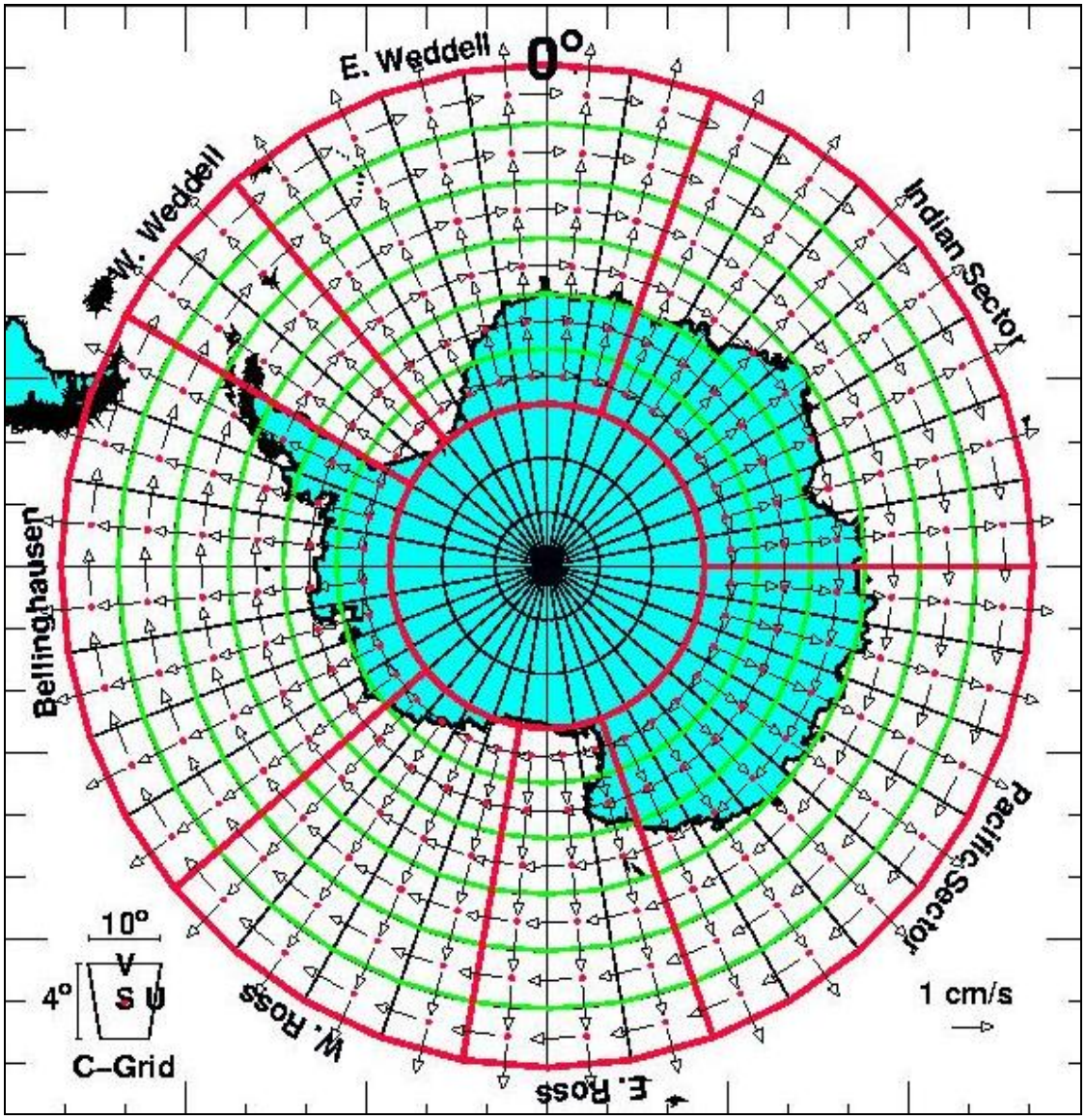

Figure 3.1: Development of a diagnostic sea ice volume and transport model. This Southern Ocean sea ice model calculates the transport of sea ice volume across flux gates on a large-scale grid (green) and regional scale (red).

All grid cells in the model follow a two dimensional grid configuration with transport calculated from the northern and eastern grid cell boundaries. Because the grid is not in Cartesian coordinates the grid cells are not square and uniform in size. A schematic of the model framework (figure **3.1**) shows the grids with the reference points from which other points are determined based on the longitude and latitude grid intervals (*dx* and *dy*). The initial reference point for this model is where the longitude, *x*, is 0° and the latitude, *y*, is 78°S. Input data are interpolated to the center point of the cell transport magnitude and direction are interpolated to cross the boundaries of the cell at the center of each side of the cell opposite the reference position. In the model, the grid center points are determined using the starting center point at 5°E, 76°S and then looping throughout the model domain to place center points at intervals of 10° longitude and 4° latitude. The corner points are determined in the same way, except the starting corner point is placed in the initial reference point. This is the basic model framework.

The model domain includes areas covered by land which are not involved in sea ice mass balance calculations. These areas are eliminated with a land mask in the model. The land mask is a separate file with a value of '0' or '1' given to each grid cell. If the majority of the grid cell is covered by land, the cell is a '0', if not, it is a '1'. The data within each grid is multiplied by the mask, so the cells with a majority land cover are removed from calculations.

More complicated masks are designed so that the model will only include the drift velocity and direction near the boundaries of the grid cell which are termed the flux gates. These are the U and V masks. The U and V masks are defined by the

creation of search boxes, which loop through the model grid cells and determine a U mask and V mask on the sides opposite the reference position. These masks become smaller boxes on the boundaries of grid cells. The U mask marks 2.5° longitude on either side of the Eastern longitude border of the cell, and the V mask marks 1° latitude on either side of the northern latitude border of the cell. These U and V Flux Boxes sort the relevant data points for use in the model. The flux boxes are shown in figure **3.1** as the as the "dummy" transport placeholder vectors.

Thickness and volume data on the model grid and regional scale are the primary focus of this study, so they will be described in the following chapters. Chapter four explains the NIC ice chart data history and current use, and chapter five details the specifics of transferring ice chart information to a model grid. Sea ice thickness and area from the NIC ice charts provides volume for the diagnostic transport model.

3.2 Sea Ice Drift Data

It is important to include the sea ice drift in studies of sea ice variability, particularly to help determine whether variability in the ice is due to thermodynamic or to dynamic processes. Sea ice motion is determined by multiple forces. In Antarctica, where winds of storm-intensity and cyclones are common, and where katabatic winds blow off the continent opening large areas of water near the coast in the austral winter, pressure ridging and open water form within the region covered by sea ice. Antarctic sea ice drift also has an important role in the climate system. By affecting transport of momentum between the ocean and atmosphere, it causes gaps and openings in sea ice which affects heat exchange between the atmosphere and ocean; and it influences ocean circulation by changing the vertical distribution of water density while at the

same time moving ice laterally from areas of freezing to areas of melting (Schmitt et al 2004). Polar sea ice transport is directly related to the air-sea heat exchange, ocean salinity variations and changes in surface albedo (Emery et al 1997).

Remote sensing methods have improved the availability of measurements in the Southern Ocean. However, polar sea ice movement observations are difficult to obtain. Satellite imagery coverage is limited by persistent cloud cover in using visible remote sensing information, and "point" data trajectories from manned ice drift camps, ship and iceberg drift, and deployed autonomous buoys, all of which only provide sparse data coverage (Emery et al 1997).

Passive microwave data from the 85.5 GHz band of the SSM/I provide comprehensive coverage starting in 1988 under most atmospheric conditions at a 15 km spatial resolution. The basic method to determine drift from SSM/I 85.5 GHz data uses cross correlation applied to daily averaged brightness temperatures and mapped to a 12.5 kilometer grid to detect surface feature displacement (Emery et al. 1997). This method shows the sub 12.5 kilometer grid scale motion, but the accuracy is affected by the physical ice pack conditions, the spatial resolution of the data, and surface melt and atmospheric water, and these motion fields cannot track small spatial scale and short temporal scale features(Emery et al. 1997). SSM/I derived motions fields are likely to be most accurate as large-scale drift representations in the winter when melt and atmospheric water are limited (Emery et al. 1997). A means to improve the accuracy of SSM/I drift vectors is to combine the SSM/I data with available in-situ data from the International Program for Antarctic Buoys. Pairs of daily composites of passive microwave radiometer images (SSM/I) interpolated with the drifting buoy data provide drift vectors (Wasserman et al 2006). Compared with sea ice drift vectors from buoy

data, drift vectors from SSM/I images agree in terms of patterns in direction, but the magnitude of the velocity is underestimated by approximately 40% (Heil et al 2001).

The Atlas of Antarctic Sea Ice Drift is a publicly available sea ice drift climatology data archive (http://imkhp7.physik.uni-karlsruhe.de/~eisatlas/) which incorporates sea ice drift measurement principles using both remotely sensed and in-situ data. All available drifting buoy data deployed in the Southern Ocean since 1985 are incorporated although they are only available at specific time and space coordinates. These are supplemented by the ice motion estimates from pairs of passive radiometer images to provide continuous coverage (Schmitt et al 2004). Because data storage of the sea ice thickness records becomes a complex issue due to size limitations, it is interesting to note the total size of this data archive for the study period is only 2.93 megabytes; storage is compact because all information is stored in data files. Figure **3.2** is a sample image from the Atlas of Antarctic sea ice drift.

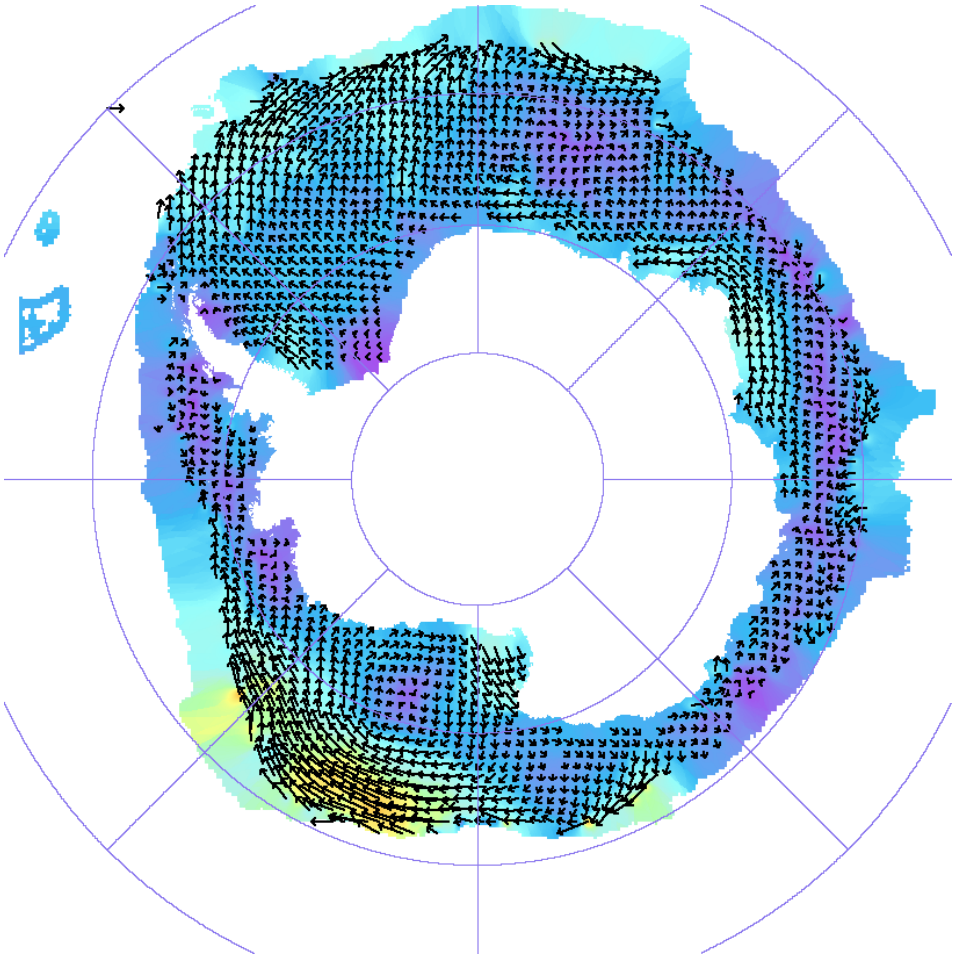

Figure 3.2: Sample motion vectors from the Atlas of Antarctic Sea Ice Drift. This is a plot of the 2-day drift average for October 1997 with ice velocity symbolized by the color gradient and arrows for direction and magnitude.

In this study, seasonal averages of ice motion from the Atlas of Antarctic Sea Ice Drift are used in two ways. First, the geographic representation of sea ice velocity fields are included to improve understanding of the ice thickness variability and anomalies on a seasonal scale, and second, the sea ice velocity fields, as well as the gridded thickness distributions, will be the input data for a Southern Ocean sea ice

volume and transport model, which will be addressed following the efforts in this work

3.3 Sea Ice Drift Data Processing with PV-WAVE

The SSM/I sea ice motion vectors are processed and interpolated to the model grid (figure **3.1**) with PV-WAVE code. Atlas of Antarctic Sea Ice Drift data files contain the geographic coordinate of the vector tail point (with a 12.5 kilometer spatial resolution), and the *U* and *V* displacement components of the vector in centimeters per second. This model uses data from the seasons March-April-May, June-July-August, and September-October-November for 1995, 1996, and 1997. For clarity in the model, any longitude between 180°W and 0° is converted to a value between 180° and 360°. The vector tail points and their displacements are converted into the standard SSM/I projection which is the polar stereographic projection (Gloersen et al 1992) with the World Geodetic System 1984 datum and 70°S as the true scale.

Within every grid cell in the model, a single *U* component and *V* component of a vector will be determined. Cell flux gates are identified as the area within one degree latitude of the northern boundary of the cell, and within 2.5 degrees of longitude on the eastern boundary of the cell. Where input drift data tail points are within a flux gate, those vectors are considered to be the input for determining the transport along that flux gate. This means that the vectors with tail points in the center of the grid are ignored. Drift data grouped within a specific are identified, and if there are more than three vectors in the flux gate, their displacements in the U and V direction are averaged. This average displacement becomes the displacement across boundaries of the grid cell. The center point of the flux gate becomes the new tail point for the vector. This process interpolates the sea ice drift across each cell

boundary. Because the data are plotted in geographic coordinates and may contain gaps associated with the presence of land, the motion vectors are repacked into a long one dimensional vector to plot each vector on a Cartesian projection with a geographic grid cell structure. The sea ice motion vectors interpolated to the model grid and prepared as input are displayed in figure **3.3**. Because ice drift products are not available for the summer, the motion is only shown for three seasons.

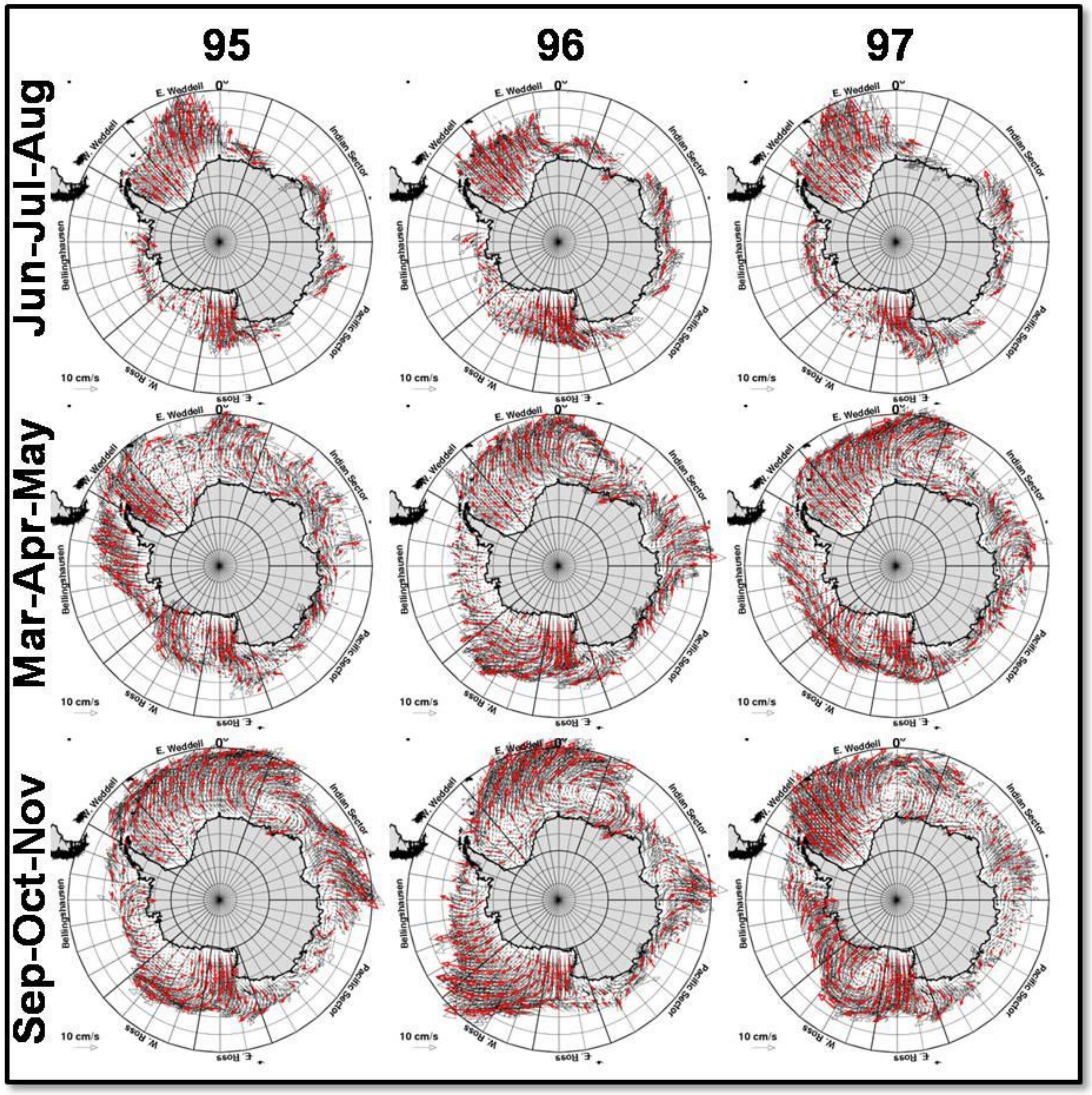

Figure 3.3: Processed sea ice motion vectors. The original sea ice motion vectors from the Atlas of Antarctic Sea Ice drift (black arrows) are overlaid with the motion vectors prepared for model input (red arrows).

Chapter 4

NIC DATA

4.1 Operational Ice Charts

This chapter describes the history, creation, and format standards for the NIC operational ice charts around Antarctica. The NIC produces weekly ice charts, which encompass the sea ice extent of the polar regions dating from 1972 to present day. When early National Oceanic and Atmospheric Administration (NOAA) and National Aeronautics and Space Administration (NASA) satellites began to provide remotely sensed data in 1972, the NIC began to create large-scale, high-resolution sea ice maps. By the late 1970s the NIC was consistently training ice interpretation analysts to determine sea ice conditions and record them on geographic paper charts following the formalized ice chart standards which co-evolved with the ice charts from the World Meteorological Organization (WMO). NIC ice charts were originally intended as safe navigation aids and were produced in paper format on hardcopy base maps. The charts included information on *ice concentration*; *ice stage of development* (where data availability justifies this record), the *ice edge* or the limit of all known ice, the limit of pack ice where ice has greater than 95 percent concentration, the limit of the *old ice* which survived a melt season, and any notable ice form including ice of land origin. On the paper charts, NIC analysts recorded this information in a compact symbol called the WMO "Egg Code" shown in figure **4.1**. The analyst determines the polygon

boundary as an area of homogeneous ice conditions, and within the polygon places an "Egg" with the information for up to three partial sea ice categories. These paper charts (figure **4.1**) provide the basis for migrating to a digital platform for creating the ice charts, as well as digitizing historical archives of ice charts. Sea Ice Data in Digital Form (SIGRID) format is a 1989 WMO system for transferring the charts as vector polygon datasets into a Geographic Information System (GIS). Computers and changing technology led to the creation of fully digital ice charts, but the fundamental process of determining ice characteristics by assimilating multiple satellite-based data sources remains unchanged (Dedrick et al 2001, Fetterer et al 2006). International ice chart analysts are still debating changes in the SIGRID code and interpretation of WMO definitions pertinent to the creation of their ice charts.

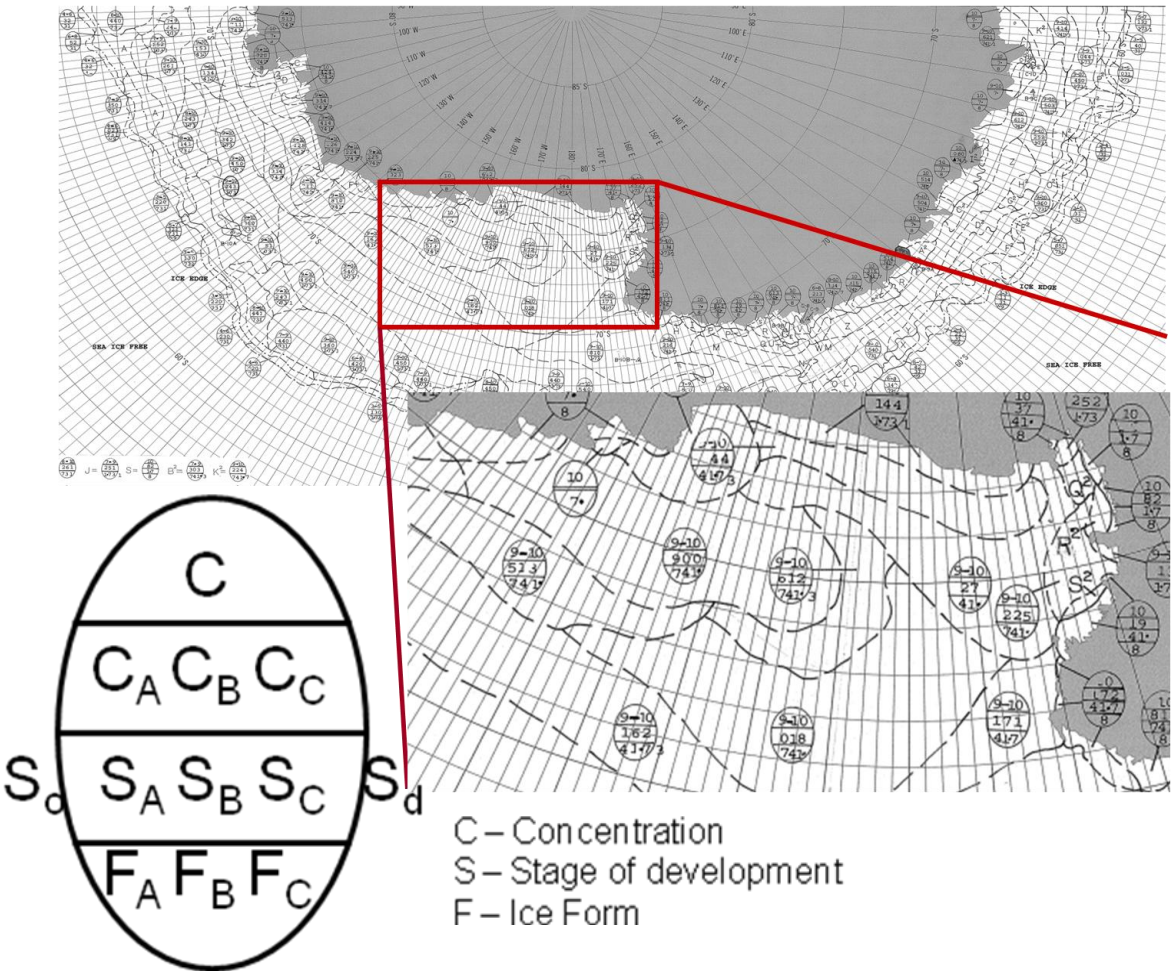

Figure 4.1: Sample Ice Chart. This figure shows an example of a scanned paper ice chart with ice types marked by the "Egg Code" within each polygon. Frequently information is missing in the eggs, particularly the form values, and the second or third partial concentration and stage of development values as evidenced in the sample ice chart eggs.

The historical digital sea ice archive from the NIC integrates visible and infrared imagery with the passive microwave imagery commonly used for ice monitoring, and the combination resolves some uncertainty from the ice concentration

data found in passive microwave data alone. There are also some higher resolution data sources with more detail, and the data record goes farther into the past than passive microwave data alone, which is important for climate research. The NIC specifically uses remotely sensed data from early NASA and NOAA satellites for larger scale, higher resolution sea ice mapping due to the coarse spectral and spatial resolution of early data. By 1979, more detailed information on ice stage of development and the associated partial ice concentrations were available due to the introduction of the Advanced Very High Resolution Radiometer (AVHRR) sensor on NOAA's polar orbiters and the Operational Linescan System (OLS) sensor on the Defense Meteorological Satellite Program satellites, as well as enhanced knowledge of ice flow appearance in optical imagery related to ice stage of development and ice thickness information from shore stations (Dedrick et al 2001).

Hence, NIC charts comprise multiple sources for satellite data, so spatial, temporal, and radiometric resolutions vary, as well as the portion of the electromagnetic spectrum in which the sensors detect reflected emitted energy. Analysts develop charts by taking advantage of the uniqueness of each sensor. There are many remote sensing data sources used to create a NIC chart. Passive microwave imagers include the Special Sensor Microwave Imager (SSM/I) from 1987-present, the Electrically Scanning Microwave Radiometer (ESMR), and the Scanning Multi-frequency Microwave Radiometer (SMMR) from 1979-87. Visible and Infrared Imagers include the Very High Resolution Radiometer (VHRR), Advanced Very High Resolution Radiometer (AVHRR), Operational Linescan System (OLS-fine), and human observers on (USN/USCG) aircraft. Active Microwave Imagers and Altimeters include Synthetic Aperture Radar (SAR) on RADARSAT-1 and ERS-1,

Side-Looking Airborne Radar (SLAR) on aircraft and Radar Altimeter on GEOS-3, GEOSAT, and ERS-1 (Dedrick et al 2001).

The NIC ice charts were publically released in 2000 in a digital spatial archive as a resource for polar researchers. Comparisons between NIC ice chart sea ice extent and concentration with historical sea ice information from the passive microwave record yields acceptable results, so the NIC ice chart data archive has the potential to extend the passive microwave record back in time and provide additional data for sea ice researchers (Dedrick et al 2001).

Although sea ice thickness cannot be determined directly from remotely sensed data, the ice stage-of-development is used as a proxy for a range of ice thicknesses (DeLiberty et al 2010). The University of Delaware digitized the 1997 paper ice charts, attributed the ice charts with the egg code information for 1995-1997, and acquired the digitized 1998 charts. All four years encompass the Southern Ocean. An extensive quality control operation was completed to check spatial and tabular accuracy of each weekly ice chart.

The ice concentrations and stage of development values as symbolized in the "Egg Codes" on the charts are reassigned values based on their associated digital SIGRID code as specified by WMO nomenclature conventions. The concentration values are then reassigned a number between 0 and 1 to give the concentration of the ice partial in a polygon in tenths. The stage of development values, according to WMO nomenclature, are associated with various thickness ranges, so these values are given thicknesses between 0 and >120 cm with associated ranges from 0 to 100 cm depending on the development stage. Ice development stages are found in table **4.1**.

This table identifies the process of using WMO standards for stage of development as a proxy for sea ice thickness (WMO 1970).

Perhaps most important to this study are the six types of first year ice which allow differentiation within the 30-120 cm range of thicknesses. However, in the Southern Ocean, the NIC distinguishes the subtypes of first year ice only between the years 1995 and 1998, despite the precedent to consistently identify subtypes in the Arctic. Thus, only the Antarctic ice charts between the years 1995 through 1998 contain sufficient stage of development information to create a thickness distribution.

For this study, digitized, attributed, and quality controlled ice chart data are stored in one ESRI personal geodatabase for each of the four years. The geodatabases include a single feature class for every ice chart, and the combined database storage size for the original databases is 1.2 gigabytes. These and all other computed feature class layers are placed in a spatial reference framework consisting of Lambert Conformal Equal Area projection and the WGS 1984 datum. The personal geodatabases were prepared through work previously completed at the University of Delaware (DeLiberty et al 2010).

Table 4.1: WMO Stage of Development.

Name	Description	Egg Code	SIGRID Code	Thickness Range
Ice Free	Water beyond the area of all known ice	None	None	No Ice
Open Water	Open water within the ice pack	"0"	00	No Ice
New Ice	Ice crystals are weakly frozen together. Includes "frazil" (fine spicules or plates of ice suspended in water); "grease" (coagulated frazil crystals); "shuga" (spongy white ice clumps of accumulated ice)	"1"	81	<5 cm
Nilas	A thin elastic covering of ice can bend with waves has a matt surface includes "dark nilas" (dark color and <5cm thick); "light nilas" (light color and >5cm thick); "ice rind" (brittle,	"2"	82	<10cm
Pancake Ice	30-300cm diameter circles of ice with thicker brims formed from the force of striking against other ice	"0" (in form of ice code)	0 (in form of ice code)	<10 cm
Young Ice	ice in the transition between nilas and first-year ice inlcuding "grey ice" (less elastic and tends to raft under pressure); "grey-white" ice (tends to ridge not raft under pressure)	"3" (young ice); "4" (grey ice); "5" (grey-white ice)	83 (young ice); 84 (grey ice); 85 (grey-white ice)	10-30 cm
First-Year Ice	ice which has grown over not more than one winter and subdivided into categories and thickness ranges	"6"	86	30-200 cm
First-Year Ice stage	"thin first-year ice/ white ice"; "thin first-year ice/ white ice first stage"; "thin first-year ice/ white ice second stage"	"7"	87	30-70 cm
First-Year Ice stage	"Medium first-year ice"	"1 dot"	91	70-120 cm
First-Year Ice stage	"Thick first-year ice"	"4 dot"	93	>120 cm
Old ice	ice surviving at least one summer melt includes "second-year ice" (summer melting produces pattern of regular puddles; "multi-year ice" (survives at least 2 summers, hummocks smoother than second-year ice, almost salt-free)	"7 dot"	95	>120 cm
Land-Fast Ice	Ice of land origin	"Δ"	98	No sea ice

Chapter 5

TRANSFER OF NIC CHART DATA TO MODEL GRID

Chapter 5 addresses the first science question asked in the introduction:

1. *How can sea ice thickness information within operational ice charts be reconstructed into a format suitable for scientific numerical modeling studies without losing any of the original content?*

The NIC data are available as GIS layers in a vector (polygon) format., but because numerical modeling is not standard in a GIS platform. Through a combination of ArcGIS tools and geoprocessing with Python scripts, the NIC ice chart data are made readily accessible for modeling studies in a gridded framework that can be used directly as climate model input. This chapter describes the data structure and processing steps to incorporate the NIC ice chart data into sea ice modeling and climate studies.

5.1 Data Processing with ArcGIS tools and Python Scripts

This section explains all the methods utilizing ESRI software and imbedded tools to analyze thickness distribution and spatial extent of sea ice in the Southern Ocean. The ESRI Desktop ArcGIS-ArcInfo (version 9.3.1) tools shown in table **5.1** are used to transpose the NIC polygons to the model grid.

Table 5.1: ArcGIS Tool Details

Name	Toolbox	Input Files	Output Files	Function
Dissolve	Data Management	Feature Class	New Feature Class	aggregates features based on a common field
Union	Analysis	Multiple Feature Classes	New Feature Class	overlaps all input features, computes spatial intersections, and writes all features to output
Intersect	Analysis	Multiple Feature Classes	New Feature Class	computes spatial intersections like the *union* tool, but it only writes the overlapping features to output
Copy Features	Data Management	Feature Class	New Feature Class	replicates a feature class; useful when environment settings of a feature class need to be changed
Clip	Analysis	Multiple Feature Classes	New Feature Class	creates an output feature class where one of the input features is limited to the spatial extent of a "clip feature class"

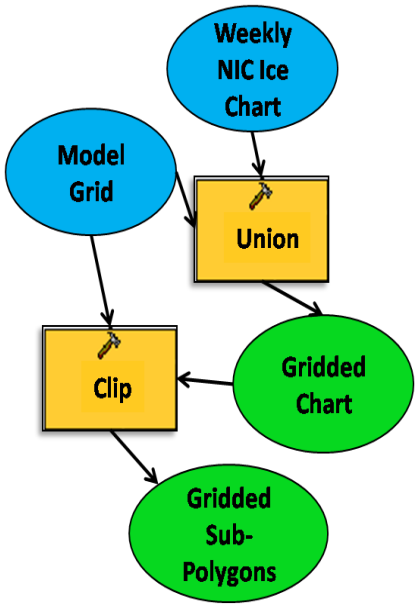

5.2 Batch Geoprocessing with Geodatabases

Thickness data from NIC ice charts are stored in separate weekly vector polygon feature classes an individual geodatabase file for each year. Batch geoprocessing with the Python scripts allows the use of all of the functionality of ESRI tools over any number of feature classes, which in this case is 208 for all weeks. Compared with the processing of individual feature classes, batch processing saves time, and it reduces the human errors involved with repeating a process. Geoprocessing scripts can be run outside of the ArcGIS environment. In this work, batch geoprocessing is the primary means to transform data stored in a polygnonal format and convert into a regular gridded format suitable as model input.

In addition to the NIC weekly ice chart feature classes, two polygon layers are created: a model grid layer and a sector region layer shown in figure **5.1**. These are

both created from text files containing the coordinates of vertices of the polygons for each grid cell and region, respectively, and using the ESRI *create feature class from text files* tool. The automatically-created Z values (to measure elevation) and M values (to measure distance) impede processing and are unnecessary for two-dimensional polygon data, so they are removed by disabling the "output has z values" and "output has M values" environment settings options. The *copy features* tool is used because output copied features do not have Z and M values after the environmental settings have been changed. The grid layer contains the same model grid as the model shown in figure **3.**1, and the region layer shares the same sectors. Duplicate model grid and region files created in PV-WAVE and ArcGIS allow for the eventual integrating of the GIS information into the mode. The grid cell and region layers delineating the study area are shown in figure **5.1**.

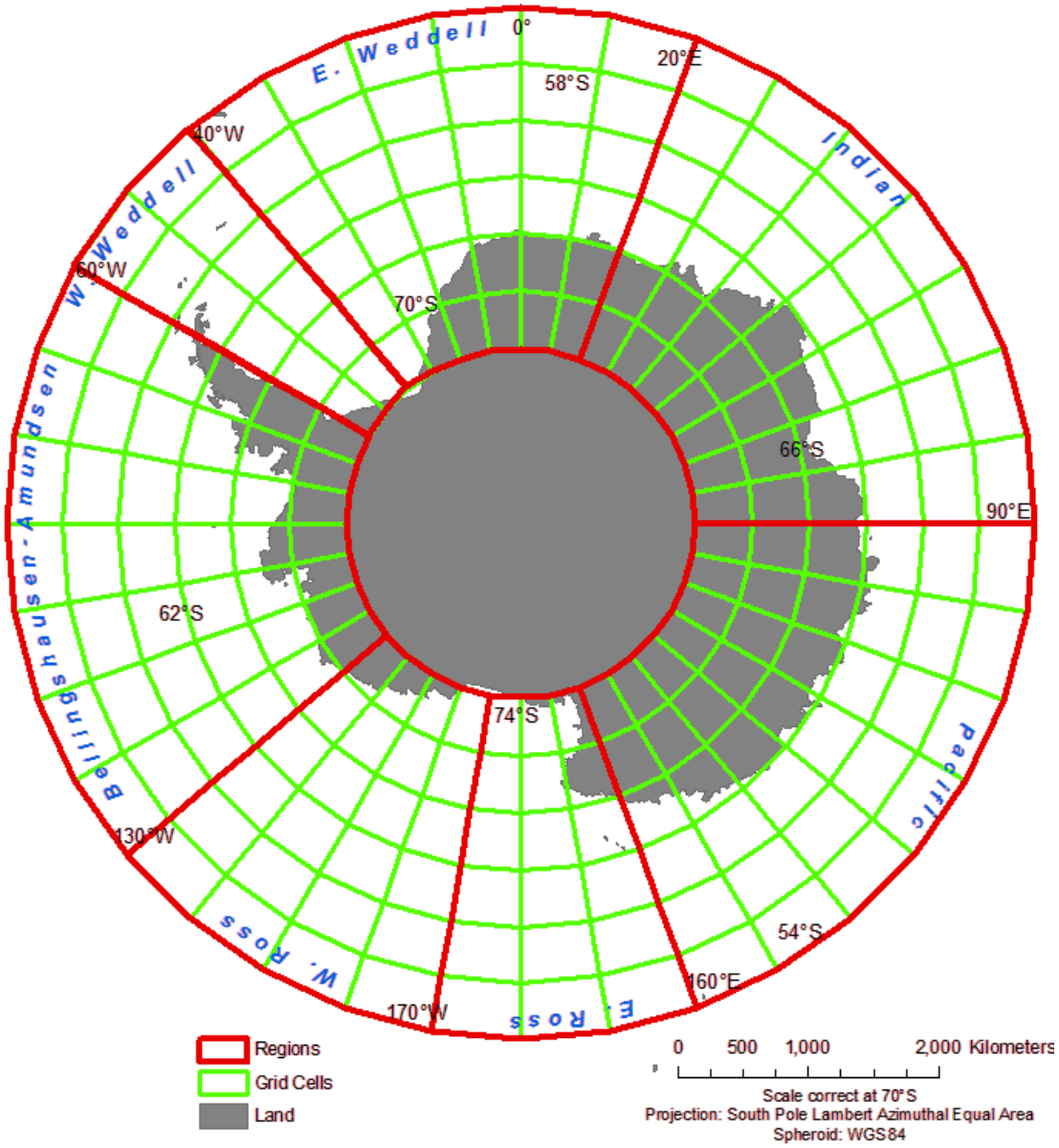

Figure 5.1: Study area and scale. This figure shows the Antarctica continent (gray) overlaid by the 10° longitude and 4° latitude grid (green) and the labeled regional sectors (red).

The *union* and *clip* tools in ArcGIS are effective in breaking up the NIC ice chart polygons into the gridded modeling framework. The Python scripting language with the "arcgisscripting" module allows the repeated use of these tools on a large dataset. For this study, a Python script is created to cycle through the four yearly geodatabases each containing weekly feature classes. The script uses the ArcGIS *union* tool to overlay the weekly NIC ice chart with the model grid, and then *clips* the gridded chart to the model grid. The product of these operations is a feature class covering the study area with the polygons from the NIC ice charts broken into grid cells. The output feature classes are larger and require more memory than the input feature classes because the *union* tool creates more polygons. Because feature classes are added, not replaced, a more effective data storage medium is necessary to ensure no loss of data.

The geodatabase in ArcGIS is a storage unit for a collection of datasets. The personal geodatabase stores all datasets in a single Microsoft Access file which makes it an effective storage unit on Windows platforms. However, the personal geodatabase has only a 2 Gigabyte size limit, and each personal geodatabase containing one year of NIC ice chart data approaches the limit. The size of the personal geodatabases prior to the study for all four years is 1.2 gigabytes, and because each process creates new feature classes, the storage size is at least doubled for every process. Therefore, data is transferred from the personal geodatabase to the file geodatabase for the remainder of this project. The file geodatabase is a storage unit that was new with ArcGIS version 9.2 (ArcGIS version 9.3.1 is used in this study) that technically has no limit to the file geodatabase size, which allows a feature class to reach over one terabyte and enables up to 65,534 fields in a table or feature class. The functionality of a file geodatabase is

not restricted by any operating system. For ease in future processing each week of NIC ice chart data in the defined grid were transferred to a single file geodatabase. The new file geodatabase is large enough to hold all four years of data in addition to new output feature classes and additional fields in the attribute tables. The final geodatabase size after all processing is 24.8 gigabytes, and it is interesting to note that the processing is neither slow nor cumbersome.

5.3 Determining Sea Ice Thickness on a Grid Cell Scale with Two Methods

In order for the NIC ice chart data to be valuable as model input, the information within each polygon in a grid cell must be transferred with minimal loss to the model grid. The records in the NIC charts cannot be expressed as a single sea ice thickness value without loss of information, so two scaling calculations are explored to determine how the information may be expressed most accurately. The subsections below proceed by building on the previous work of DeLiberty et al (2010) which computed an average sea ice thickness (DeLiberty et al 2010). In this effort, the originally reported ice chart thickness distribution is carried to each level of the model grid or region before computing an integrated thickness rather than propagating a series of ever-smoothing averages. Section 5.3 concludes with figures of the full sea ice thickness distribution focused geographically.

5.3.1 Previous Sea Ice Thickness Calculations from the UD Archive

Exploration of NIC ice charts at the University of Delaware prior to this study included the determination of the average sea ice thickness of every polygon in the NIC charts. This calculation is based on the egg code/SIGRID concentration and stage of development records. The concentration records correspond to codes *CT*,

CA, *CB*, and *CC* for the total concentration, and the partial concentration of up to three ice types, respectively, and the stage of development records correspond to codes *SA*, *SB*, *SC* for the partial stage of development for up to three ice types. The previous work (DeLiberty et al 2010) documented the physical interpretation of these records with the concentration in tenths noted as *TC*, *C1*, *C2*, and *C3*, and the mean sea ice thickness as *S1*, *S2* and *S3*. With these values, an area-weighted mean thickness value in centimeters was determined for every polygon, and chronicled in a field called *thick*. The computation of average sea ice thickness, *thick*, for polygon, *n*, follows the equation

$$thick_n = c_{1n} * s_{1n} + c_{2n} * s_{2n} + c_{3n} * s_{3n} \quad (5.1)$$

The average sea ice thickness (polygon thickness on a grid cell scale) is necessary for comparisons between the integrated and average thickness computation methods. The field *thick* is stored in all ice chart feature classes.

5.3.2 Sea Ice Thickness Distribution of a Grid Cell

The full sea ice thickness distribution for each grid cell in the study area are calculate using input weekly NIC ice chart feature classes divided into the established grid. The output data are new feature classes created for every original feature class containing 11 new fields named *Bin0* through *Bin9* plus a field for the total *Bins*. These new fields become containers for the percentage of any ice type coverage found in a grid cell where these bins represent ranges of sea ice thickness and the open water within the ice pack (table **5.2**), as well as a bin for the "ice free" areas beyond all known ice, glacial ice (ice of land origin), land, and a small percentage tagged as no data where ice type coverage could not be determined. The field containing the total

bin percentage is included as an error check to ensure the sum of all cell bins equal 100 percent.

Table 5.2: Grid Cell Coverage Including WMO Ice Types and Corresponding Thickness Ranges

Bin	Sea Ice Thickness Range [cm]	WMO Sea Ice Type & Other Coverage
Bin0	--	Ice Free
Bin1	0	Open Water
Bin2	0-10	New Ice, Nilas
Bin3	10-30	Young Ice
Bin4	30-70	Thin First-Year Ice
Bin5	70-120	Medium First-Year Ice
Bin6	>120	Thick First-Year Ice, Old Ice
Bin7	--	Land
Bin8	--	Undetermined
Bin9	--	Glacial Ice

Every sub-polygon is associated with a particular grid cell via an *i* index value for longitude and a *j* index value for latitude. There 36 possible longitude values (from the circumpolar grid demarcated every 10°) and 6 possible latitude values (from 54° S to 78° S demarcated every 4°) totaling 208 grid cells. The Python script cycles through every gridded sub-polygon feature class, and while in the feature class (an individual week), it uses a search query to select every polygon tied to a particular grid cell.

When a GIS process changes the area of polygons of feature classes stored in a geodatabase, the areas are automatically calculated and recorded in a field called Shape_Area. Hence, the area of each sub-polygon is automatically generated when the feature classes are overlaid with the grid cells through the *union* process. Total area of the grid cell is determined from the sum of all of the areas of all sub-polygons within the grid cell as specified by

$$Cell\_Area_{ij} = \sum_{n} Shape\_Area_{nij} \tag{5.2}$$

and

$$Polygon\_Fraction_{nij} = \frac{Shape\_Area_{nij}}{Cell\_Area_{ij}} \tag{5.3}$$

The *ij* subscripts are unique grid cell identifiers, and *n* is an index from one to the number of sub-polygons in a cell.

The script fills the output bin fields by determining the grid cell coverage through a series of conditional if statement blocks. Within the conditional blocks, the partial concentrations of ice type coverage categories in the grid cell are added together. Special care is taken to ensure the land, glacial ice, and ice free ocean beyond the ice extent areas are placed into the correct bins. Ice-free areas to be placed into *Bin0* are not associated with any data on the NIC ice charts because the term ice free by definition includes only ocean beyond the ice extent. Where there are ice free polygons within a grid cell, the polygon grid cell area fractions are added together.

Determination of coverage within the ice pack becomes more complicated. Where the total concentration of an identified polygon is zero, the fraction of the grid cell covered by that polygon is placed in the open water bin named *Bin1*. Open water is also found in polygons with ice types recorded. In these cases, open water is identified with the equation

$$Open\_Water_{nij} = \left(1 - \sum_{x=1}^{3} \frac{c_{nijx}}{10}\right) * Polygon\_Fraction_{nij} \quad (5.4)$$

where *x* identifies up to three partial concentrations, *c*, and the subscripts *nij* identify the sub-polygon. After the open water concentrations of all sub-polygons in the cell are recorded, they are added together for the total open water concentration in the cell filling the *Bin1* field.

Ranges of sea ice thickness are placed into five sea ice bins defined as *Bin2*, *Bin3*, *Bin4*, *Bin5*, and *Bin6*. Although thickness ranges vary for each bin, the method is constant. For each bin, the thickness is greater than the lower bound, and less than or equal to the upper bound (values matching the upper limit are placed into the bin). Thus, sea ice with a thickness of 70 cm falls only into Bin 4 for thin, first-year ice. The ice thickness range is determined using the fields which transform SIGRID stage of development codes into median thickness values with associated ranges of *s1*, *s2*, and *s3* (refer to table **5.2** for thickness and stage of development codes). Where the median thickness is within a bin's range, the partial concentration of those ice types for the grid cell are added together.

$$Bin_{bij} = \sum \frac{c_{bxnij}}{10} * Polygon\_Fraction_{nij} \quad (5.5)$$

The above equation expresses how a range of ice thickness is placed into a *bin*, where *b* is a value from two through six to identify the thickness range of the bin, *x* is the partial number which ranges from one to up to three, *n* identifies sub-polygons, and the *ij* notation marks the grid cell.

In the table formed after the *union* of ice charts with the model grid layers, land is uniquely identified through a pattern of field values. All SIGRID fields contain values of -1, and all fields created through previous work at the University of Delaware, including the fields holding numerical values for sea ice concentration and stage of development, contain null values (for information not within the ice chart). Where these two conditions are found, land polygons are placed into the *Bin7* container by summing the polygon fractions.

Datasets as large and complex as the NIC ice charts tend to have occasional areas without data. If an area within the study extent cannot be classified in a bin it is marked as null and placed into *Bin8*. In addition, polygons labeled with the SIGRID code stage of development value equal to 99 are considered of undetermined ice type, and these are marked as no data and placed into *Bin8*.

The SIGRID stage of development value equal to 98 designates glacial ice or ice of land origin. Areas with ice of land origin are placed into *Bin9* in the same manner that is used to place area with specified thickness ranges into sea ice bins. The *Bin9* fraction of a grid cell is the sum of the polygon fraction of the grid cell covered by all partial concentrations connected with the partial stage of development 98.

Figure **5.2** gives a simple example of transformation from polygon thickness distributions to a model grid. After all coverage fractions are determined for a grid cell, the total coverage of the cell is calculated as the sum of all other bins. This is designed as an error check to ensure all cells have 100% coverage.

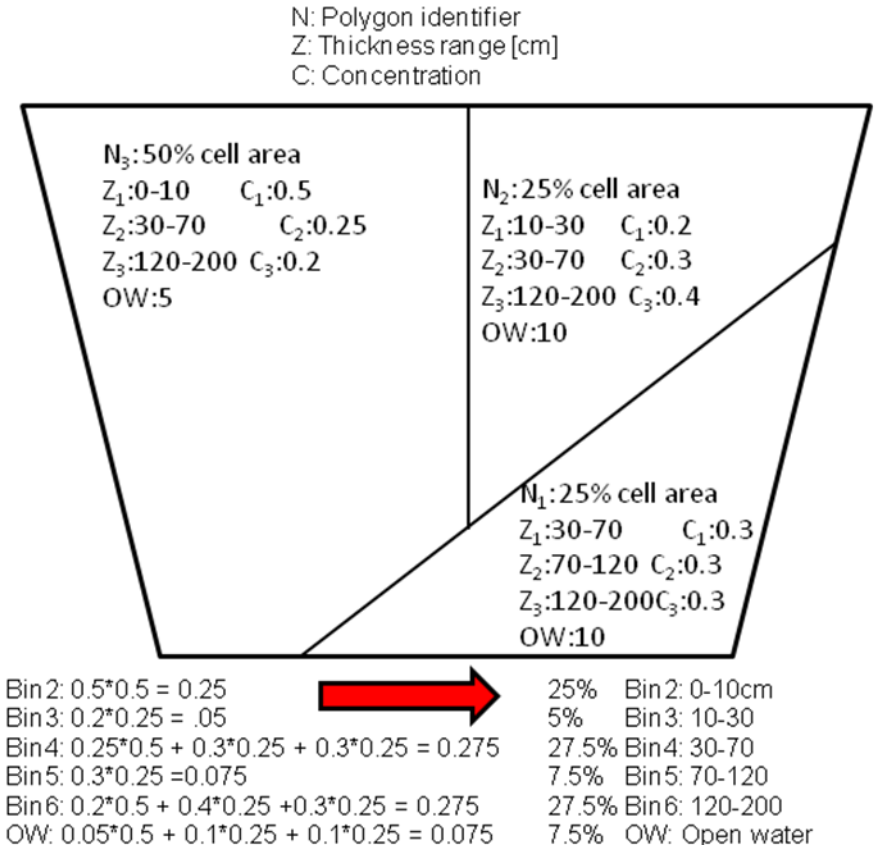

Figure 5.2: Consolidating thickness distributions within a model grid cell. This is a simple example of upscaling the thickness distributions of the sub-polygons in a model grid cell to determine the overall thickness distribution of the cell. The percent coverage of any bin is the sum over all sub-polygons of the product of the associated concentration and polygon area fraction.

To store the *bin* values for each model grid cell in the output file, a search cursor scans the output grid file to determine where the grid cells are associated with the same *ij* notation. In an ArcGIS geographic view, the output feature classes appear to display simply the model grid, but the associated attribute tables contain the spatial location, area of each grid cell, and the percentage of ice-free, open water, each ice thickness range, land, glacial ice, and "no data" within the cell. Because the *ij* index

associates a row with a cell location the model grid, it is no longer necessary to continue to use the spatial components of the feature class; only the table is needed. This effort utilizes the power of relational database structuring. The *ij* index is consistent through all methods in this study, so that index is sufficient to spatially link the data in the output attribute tables to a model grid developed with the PV-WAVE programming language.

For analysis and modeling, the grid cell locations and cell coverage by bins are the critical data. A Python batch-processing script loops through every week of data, exports the important data fields from the feature class attribute table, and saves them as ASCII text files. For data accessibility in PV-WAVE, another Python script to rename the files to an explicit time designation denoting the year and week to temporally match individual weeks and seasons during the four years as shown in table **5.3.** After this final step with Python, the full thickness distribution may be analyzed outside of ArcGIS. This allows the use of the table values without the spatial information, which reduces processing time and space.

Table 5.3: NIC Ice Chart Time Table

Week	NIC 95 date	NIC 96 date	NIC 97 date	NIC 98 date	Season
1	950105	960104	970103	980105	DJF
2	950112	960111	970110	980112	DJF
3	950119	960118	970117	980119	DJF
4	950126	960125	970124	980126	DJF
5	950202	960201	970131	980202	DJF
6	950209	960208	970207	980209	DJF
7	950216	960215	970214	980216	DJF
8	950223	960222	970221	980223	DJF
9	950302	960229	970228	980302	DJF
10	950309	960307	970307	980309	MAM
11	950316	960314	970314	980316	MAM
12	950323	960321	970321	980323	MAM
13	950330	960328	970328	980330	MAM
14	950406	960404	970404	980406	MAM
15	950413	960411	970411	980414	MAM
16	950420	960418	970418	980420	MAM
17	950427	960425	970425	980427	MAM
18	950504	960502	970502	980504	MAM
19	950511	960509	970509	980511	MAM
20	950518	960516	970516	980519	MAM
21	950525	960523	970523	980525	MAM
22	950601	960530	970530	980601	MAM
23	950608	960606	970607	*NoData	JJA
24	950615	960613	970613	*NoData	JJA
25	950622	960620	970620	980622	JJA
26	950629	960627	970627	980629	JJA

Table 5.3.1: NIC Ice Chart Time Table Cont'd

Week	NIC 95 date	NIC 96 date	NIC 97 date	NIC 98 date	Season
27	950706	960703	970704	980706	JJA
28	950713	960711	970711	980713	JJA
29	950720	960719	970718	980720	JJA
30	950727	960725	*NoData	980727	JJA
31	950803	960801	970731	980803	JJA
32	950810	960808	970808	980810	JJA
33	950817	960815	970815	980817	JJA
34	950824	960822	970822	980824	JJA
35	950831	960829	970829	980831	JJA
36	950907	960905	970905	980907	SON
37	950914	960912	970912	980914	SON
38	950921	960919	970919	980921	SON
39	950928	960926	970926	980928	SON
40	951005	961003	971003	981005	SON
41	951012	961010	971010	981012	SON
42	951019	961017	971017	981019	SON
43	951026	961024	971024	981026	SON
44	951102	961031	*NoData	981102	SON
45	951109	961107	*NoData	981109	SON
46	951116	961114	*NoData	981116	SON
47	951122	961121	*NoData	981123	SON
48	951130	961128	*NoData	981130	SON
49	951207	961204	*NoData	981207	DJF
50	951214	961212	*NoData	981214	DJF
51	951221	961219	*NoData	981221	DJF
52	951228	961226	*NoData	981228	DJF

5.3.3 Seasonal Maximum and Minimum Sea Ice Extent

For geographic visualization of the sea ice conditions, it is valuable to know the seasonal absolute minimum and maximum spatial extent of the sea ice in the Southern Ocean. A simple method to determine the sea ice minimum and maximum extent requires only the NIC ice charts as input data and three tools in ArcGIS: the *Dissolve*, *Union*, and *Intersect* tools. The first step to determine the sea ice minimum and maximum is to use the ArGIS dissolve tool. Each weekly ice chart is input to the *Dissolve* function, and output denotes the outline of the sea ice extent determined from the ice chart. All weeks from a given season (as specified in table **5.**3) are input to the ArcGIS *Union* tool. The *Union* tool overlaps all dissolved weekly ice chart extent layers and outputs the spatial extent to determine the maximum extent. The *Dissolve* tool is run again on the unioned output to remove any internal polygons, leaving only the maximum extent. The seasonal weekly ice charts are input to the ArcGIS *Intersect* tool which outputs the overlap (areal extent of sea ice which overlap during the designated season). The *Dissolve* tool removes any internal polygons and leaves only the outline of minimum extent. The seasonal extent and climatology are shown in figure **5.3**.

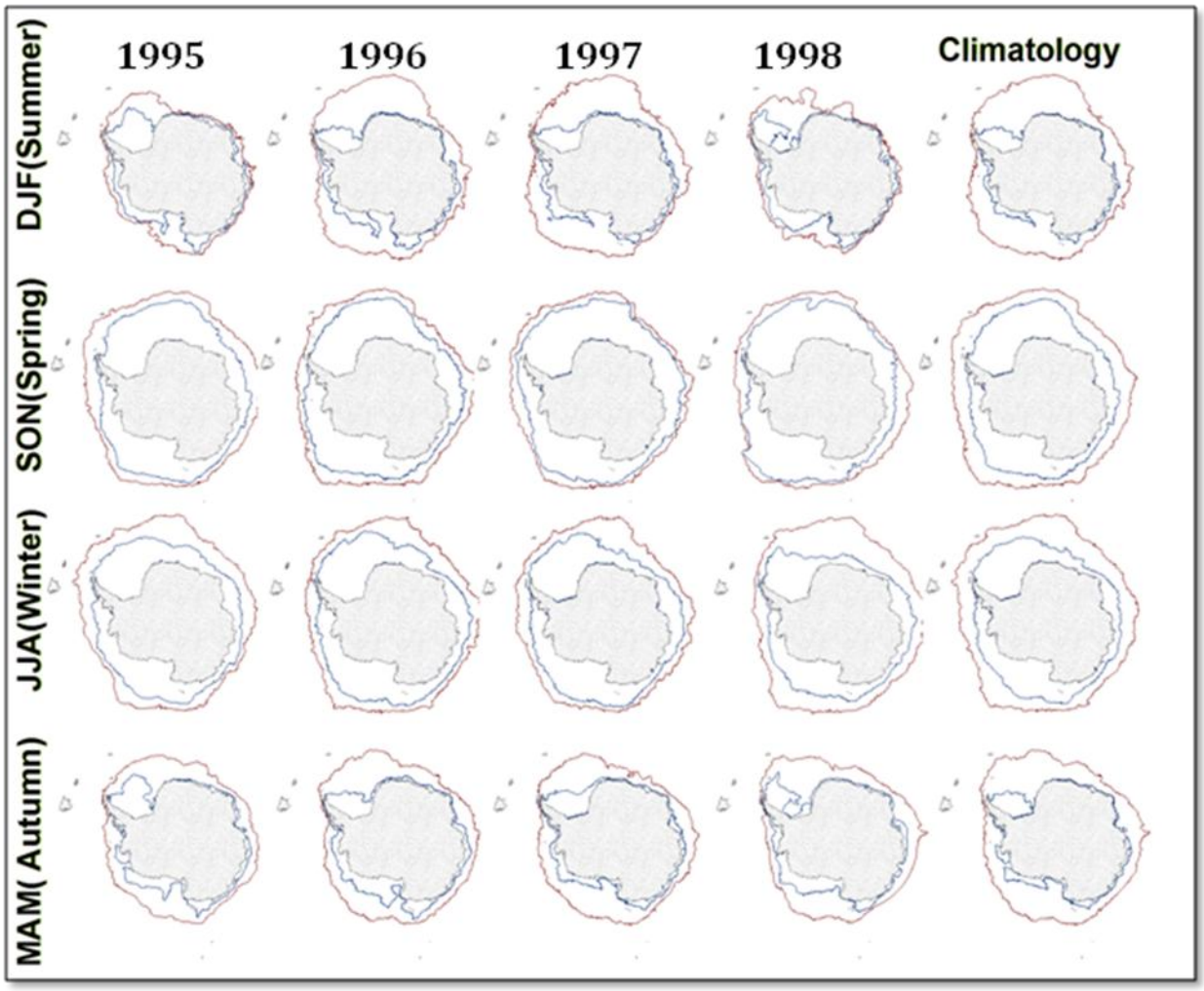

Figure 5.3: Seasonal minimum (blue) and maximum (red) sea ice extent by year and climatology.

The seasonal minimum and maximum sea ice extent outlines highlight several interesting characteristics of the Southern Ocean sea ice. For the four years, summer is the season with the largest inter-annual variability in maximum sea ice extent which may indicate the importance of retaining multi-year ice through the summer melt period. The spring minimum and maximum extents are the most similar and show the

least inter-annual and intra-seasonal variability of all seasons. The consistent sea ice ranges may be due to the lack of melt in the Southern Ocean due to the continuation of cold temperatures. Inter-annual variability in sea ice in spring may be predominantly due to deformation over the winter. Inter-annual changes in winter sea ice extent are likely due to changes in the rate of ice freezing. The autumn maximum sea ice extent follows the summer ice extent closely, but it is interesting to note that the summer maximum extent is larger than the autumn maximum extent for the years 1996 and 1997.

The absolute minimum and maximum sea ice extent by climatology shows two trends. The range of sea ice extent over any season is considerable with the largest range found in summer followed by the range in autumn, then winter, and spring. There is a considerable sea ice extent in the West Weddell Sea between the Antarctic Peninsula and the Ronne Ice Shelf as evident from the Weddell Sea ice extent year-round (Ackley et al 2001).

5.3.4 Sea Ice Thickness Distribution Preliminary Analysis

A comparison of the thickness distribution and average thickness method is shown in figure **5.4**. The average thickness by polygon is broken up into the model grid cell to illustrate an individual grid cell's sea ice information. From this sample, it is evident that a thickness distribution provides a clearer representation of sea ice thickness conditions and variability than the average thickness value.

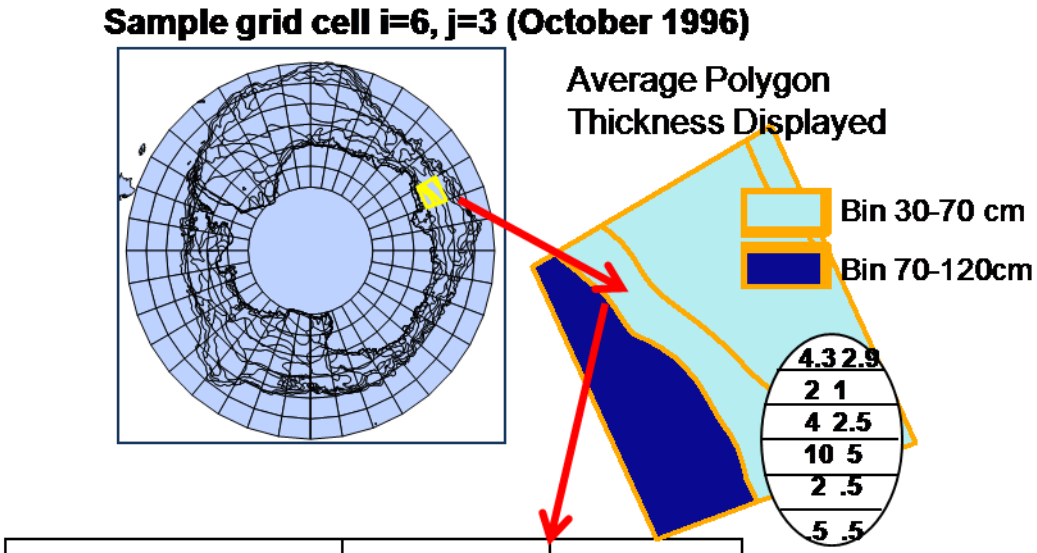

Thickness(cm)	Fraction	%
0-10	0.08	8.04
10-30	0.19	19.86
30-70	0.63	63.40
70-120	0.01	1.07
OW	0.07	7.61
	Total	100

Figure 5.4: Average Thickness vs. Thickness Distribution Variability. A sample grid cell from the spatial intersection of NIC chart and model grid for the week of 10 October 1996 shows two computational methods to express sea ice thickness on a model grid.

Exploration of the meaning of the full sea ice thickness distribution requires an understanding of all the information in the ice charts combined with information at the grid cell scale. A visualization of this information is found in figure **5.5**. This figure shows the average polygon thickness of an entire ice chart with two sample cells

identifying their respective thickness distribution and "Derived Egg Code" values. The derived egg code is simply all the information on sea ice thickness and distribution found in the original egg code but displayed in terms of thickness and associated ranges. Black dots on the ice chart are ASPeCT observations coincident with the 1995-1998 time period. The spatial distribution of the ASPeCT observations shows the utility of the additional information supplied by the NIC charts. The NIC charts provide spatial and temporal information to fill gaps in other data sources.

The two sample cells show the numerous sub-polygons that lie within a model grid cell, and that this variability may not be appropriately understood with a single average thickness value. Thus, from these cells the thickness distribution is determined and symbolized with a stacked bar identifying thickness ranges. One major feature apparent on the stacked distribution is the open water fraction. This fraction is virtually unidentifiable on a chart of average thickness, yet this fraction impacts sea ice dynamics and thermodynamic processes.

Figure **5.5** illustrates the process of creating the gridded thickness distribution. A weekly ice chart with polygons symbolized with average thickness values is broken up into grid cells (orange lines) and sectors (red lines). Inset cells show how the information within sub-polygon features are integrated into a cell with ranges of thickness. The derived egg code indicates the detail of the thickness and concentration data which may be drawn from the original egg codes. Figure **5.6** shows the derived thickness distributions for four sample ice charts with one chart in every season to visualize the model-input-ready thickness distribution data on the smallest temporal (weekly) and spatial (gridded) scales available for this study.

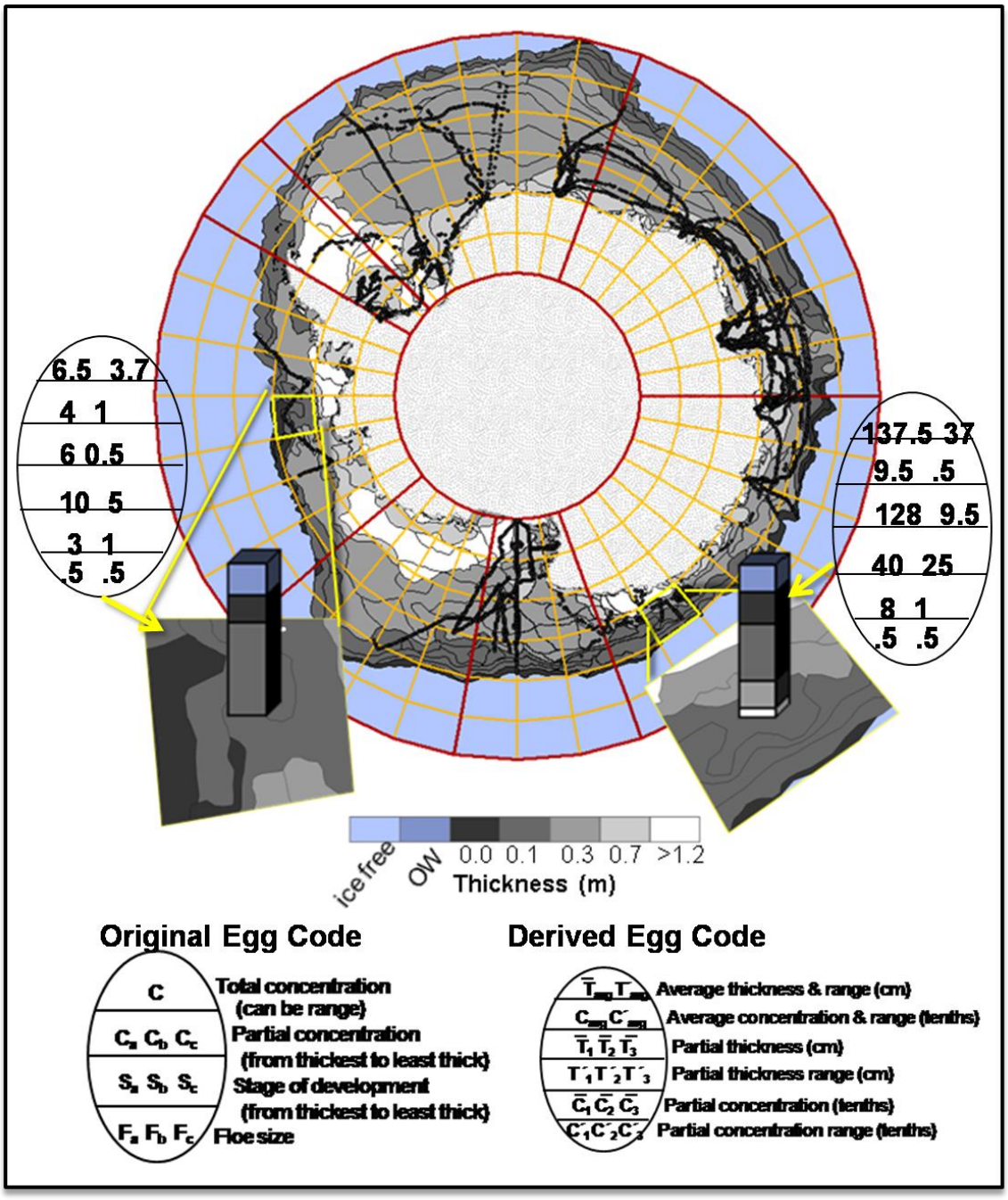

Figure 5.5: NIC chart derived average thickness and thickness distribution on a grid.

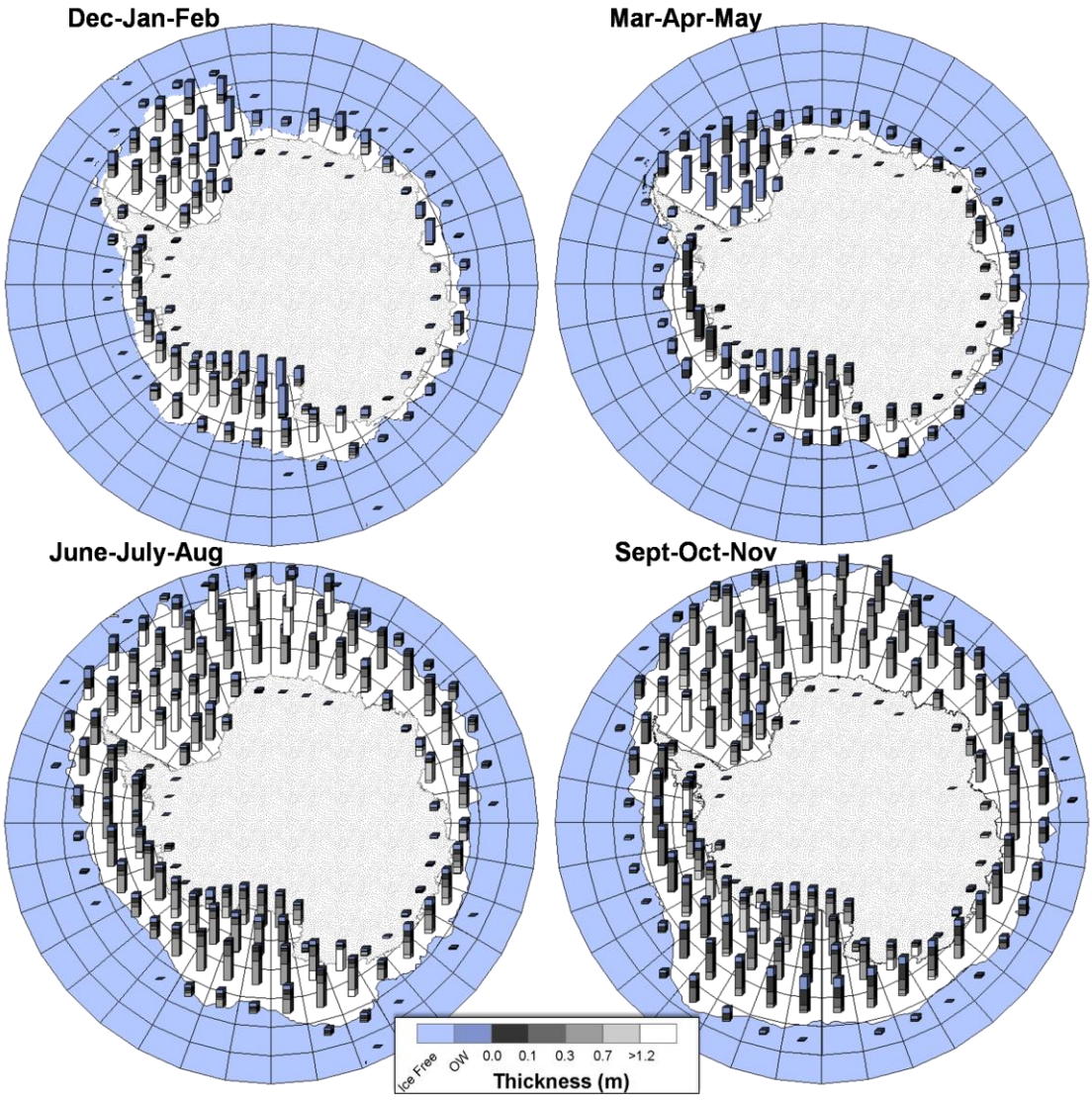

Figure 5.6: Weekly samples of sea ice thickness distribution on a model grid for four seasons. The white area represents the sea ice extent. The stacked bars is located within any grid cell with some fraction of sea ice coverage, and the bars show the thickness distribution by sea ice thickness range and open water fraction.

Figure **5.7** shows the average thickness distribution by season and sector. There are a number of features in this climatology which follow trends uncovered in Worby

et a. (2008). In the summer months of December, January and February (DJF), there is a period for extremes. The mean thickness values are the highest of all four seasons because the multi-year-thick ice remains in the summer, while very little thin ice is retained. The thin ice bin accounts for a very small percentage of the total ice. In the autumn months of March, April and May (MAM), new thick ice formation from freezing is evident. Thin ice begins to account for a greater percentage of the ice pack. In the winter months of June, July and August (JJA), redistribution of thin ice into thicker ice categories is apparent. The winter also shows the least variability between ice thickness categories. The spring months of September, October, November (SON), like the months of autumn, are a transition period, and similarities between the two seasons are expected. Autumn has more thin ice due to the formation of new ice, and spring has a higher quantity of thicker ice, likely due to deformation over the winter.

Some trends in regional variability are observed in figure **5.7**. The western Weddell Sea shows the least variability, with the main feature being the high percentage of thick ice year round. The eastern Weddell Sea, Indian Ocean sector, and Pacific Ocean sector have similar thickness distributions year round. There is some thicker ice in the eastern Weddell from ice advecting from the West Weddell Sea, and there is thicker ice in the Pacific caused by ice advection from the eastern Ross Sea. The Bellingshausen-Amundsen Sea also exhibits year round thick ice, particularly through the thick ice retained throughout summer.

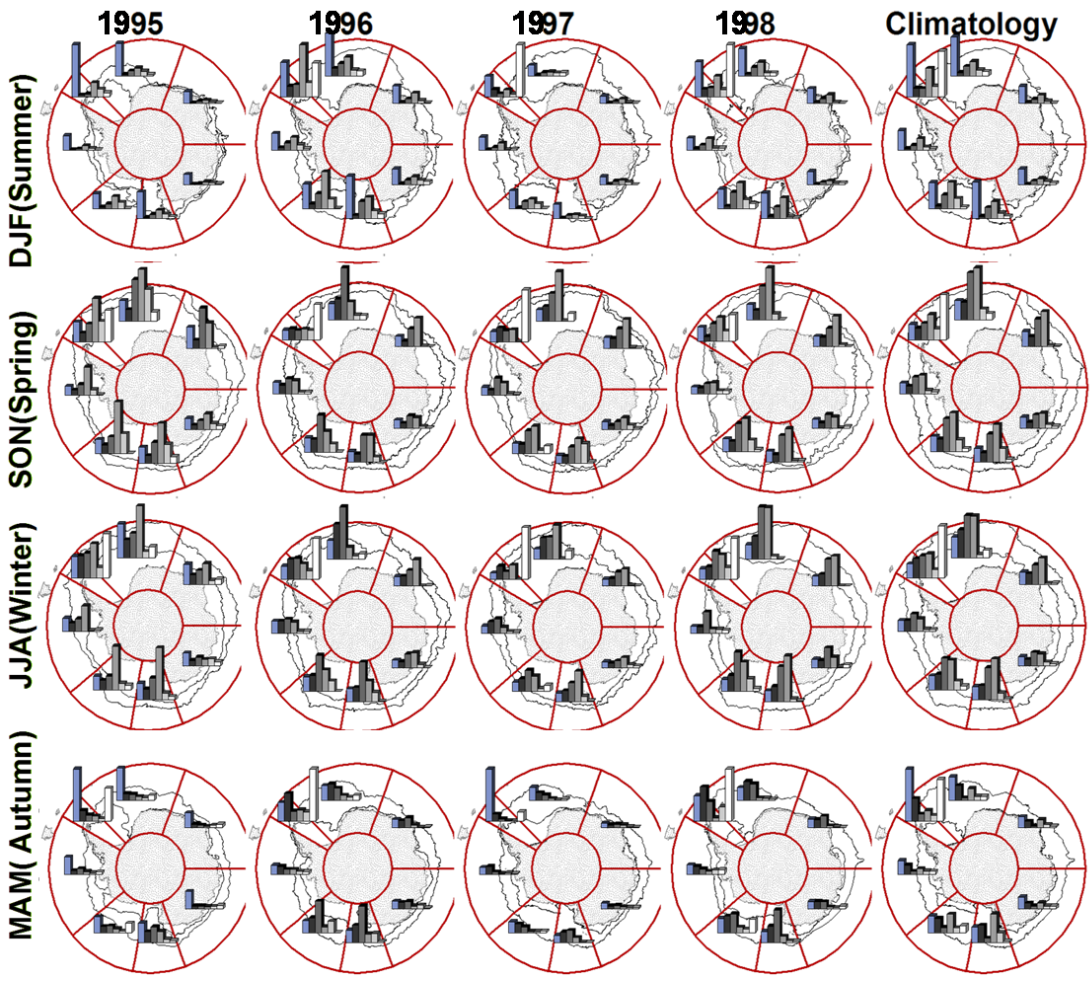

Figure 5.7: NIC-derived sea ice thickness distribution by season and the four-year climatology. Seasonal minimum and maximum extents are plotted around the continent.

5.4 Chapter Summary

This chapter examined the processes by which the NIC ice charts are prepared as thickness distribution input data for modeling studies. Batch geoprocessing with Python scripts spatially intersects the ice chart polygons with grid cells and calculates the fraction of coverage by bin based on an area-weighted integration of concentration

and thickness ranges. This chapter provides the visualization necessary to understand how the weekly thickness distribution becomes model-input information. Initial analysis of the thickness distribution with ArcGIS shows the general geographic patterns of the thickness distribution by sector as well as the seasonal cycle of the sea ice by specific years and climatology.

Chapter 6

METHOD IMPACTS ON SEA ICE THICKNESS

This chapter addresses the second science question asked in the introduction:

2. What is the impact of A.)an integrated sea ice thickness distribution instead of the average sea ice thickness on the climatology and the inter-annual variability? and B.) open water within the ice pack on sea ice thickness records?

6.1 Computing Integrated and Average Thickness with and without Open Water

Before examining the sea ice thickness computation methods, it is useful to examine the accepted sea ice terminology. The term *sea ice extent* is defined by the World Meteorological Organization (WMO) as the area of all known ice, but this is not necessarily the standard. While the NIC does record ice extent as the area of all known ice, the National Snow and Ice Data Center (NSIDC) accepts the ice extent to be the area encompassing regions with 15% or greater sea ice concentration. To clarify, the WMO definition of ice extent is used for this study, so *ice extent* includes the open water fraction within the ice pack. The term *sea ice area* refers to the ocean area physically covered by sea ice only. Beyond the ice extent the ocean is referred to as *ice free*, so that the term open water is reserved for the water within the ice pack. This open water fraction is critical. It is clear that averaging over the larger area associated with open water without changing sea ice thickness will necessarily smooth

the mean thickness. However, it is still important to track the open water fraction. Open water locations experience direct atmosphere-ocean heat fluxes, and are critical locations for new ice to form.

It is also useful to consider the terms used here to describe the two thickness methods. *Integrated thickness* and *average thickness* in this case describe two ways to compute a statistical mean value from a distribution. If a probability density function has a Gaussian or normal distribution, then the mean, median, and mode are essentially the same value. Sea ice thickness varies with thermodynamic changes and deformation, and although the probability density function of a thickness distribution is defined (Rothrock 1986), the function is not likely to be normal. Thus, it is important to seek a representative mean thickness value which accounts for the myriad variability of sea ice thickness over an area.

The average thickness values of the NIC ice chart polygons have already been determined through previous work (see section **5.3.1**). An examination of propagating the average polygon thickness to the model grid yields two equations for average thickness for the area of the ice only (AT) and average thickness for the area of the ice and open water (ATOW). In the following equations, the polygon area for the ATOW calculation includes all ice and open water, and for the AT calculation includes only ice area in the polygon.

$$ATOW_{ij} = \frac{\sum_n (thick_{nij}\, PolygonArea_{nij})}{GridCellArea_{ij}} \tag{6.1}$$

$$AT_{ij} = \frac{\sum_n (thick_{nij} * PolygonIceArea_{nij})}{GridCell\_IceArea_{ij}} \tag{6.2}$$

In the average thickness equations, the grid cells are identified with an *ij* identifier for grid cell, and the sub-polygon in the grid cell as *n*. This process calculates the area-weighted thickness average for a cell, but it does not conserve any information from the partial ice type thickness or concentration.

Another mean thickness calculation is proposed to compute an integrated thickness. This calculation aggregates individual concentrations by thickness range and propagates the thickness ranges to the model grid cell. In this method the concentrations are averaged but the thickness information within the cell is retained. The integrated thickness is calculated over the ice area (IT) and the entire ice plus open water area (ITOW). The IT and ITOW calculations are simplified as the sum of product of bin concentrations and the median thickness value for the bin. Every grid cell, *ij*, has a known area, A_{ij}, up to five ice categories ($k=[2,6]$) plus open water ($k=1$), *k*, and each of those ice categories has a thickness a range with a median value, Z_{ijk}, and a concentration, C_{ijk}. Mathematically, IT and ITOW are expressed as

$$IT_{ij} = \frac{\sum_k (Z_{ijk} C_{ijk} A_{ij})}{(\sum_{k=2}^{6} C_{ijk})\, A_{ij}} \tag{6.3}$$

$$ITOW_{ij} = \frac{\sum_k (Z_{ijk} C_{ijk} A_{ij})}{(\sum_{k=1}^{6} C_{ijk})\, A_{ij}} \tag{6.4}$$

where the denominator is the total fraction of the cell covered by either ice only or ice plus open water.

The PV-WAVE interactive programming language provides full mathematical support as well as excellent graphics, so this software is used. The PV-WAVE scripts examine sea ice thickness distribution and average thickness through the comparison of 1) regional thickness and thickness anomalies from multiple computational methods and 2) the effect of tracking the open water fraction within the ice pack versus tracking only the sea ice thickness fractions.

The programming script reads data from all text files based on the year and week of the year and carefully tracks missing weeks. For the 216 grid cells that compose the model grid, there are records of the longitude (*i*) index, the latitude or (*j*) index, and all of the bin types**.** The four-year weekly climatology is found by temporally averaging all weeks corresponding to a given time of year (these are each row in table **5.3**). Because some weeks are missing, a counter determines the number of weeks available for the climatology calculation. Weekly grid cell anomalies for the sea ice thickness distribution (*Bin1* though *Bin6* for open water and all ice bins) are computed as the difference between the weekly value and the weekly climatological mean. Positive anomalies indicate larger than average values, and negative anomalies indicate smaller than average values. The script calculates the four methods yielding a single thickness value for a grid cell based on the full distribution (AT, ATOW, IT, ITOW). It then finds the climatological means for the four methods and their anomalies for comparison with the full thickness distribution.

6.2 Results of Science Question 2 by Sector

This section explores the impact of calculating IT versus AT on the variability retained in the sea ice thickness values for a grid cell, and the contribution of tracking

the open water fraction on the thickness values. Results for each sector are shown in a series of three figures for every sector, each with two plots.

The first figures for the sector show the 1995-1998 thickness distribution as stacked bars. The ice extent plot [a] displays the total ice area plus open water and bases this calculations upon the total ice plus open water area (i.e., 100% ice extent). Thus, the stacked thickness distribution represents the percent of each sea ice thickness range within the sea ice extent of a particular week. The two dotted lines overlaid on the thickness distribution climatology are the ITOW and ATOW values. The ice area plot [b] includes only the areas covered by sea ice, so the stacked distributions represent the percentage of ice type cover out of the total ice coverage. The two dotted lines overlaid on the thickness distribution climatology are the IT and AT thickness values.

The second set of figures show the sea ice thickness distribution by week for all 208 weeks from January 1995 – December 1998. Weeks for which no ice chart is available are excluded from analysis and the missing time period is marked with a no data placeholder on the plot. For the weekly regional plots, the stacked sea ice distribution for ice extent [a] and ice area [b] are determined as they are for the climatology plots. For ice extent, 100% of the area of interest is the area of the total ice coverage plus the open water, and for ice area 100% of the area of interest is only the area of the ice coverage. AT, IT, ATOW, ITOW lines are plotted over the distributions.

The final set of regional figures display the weekly anomalies of the thickness distribution, the average thickness, and the integrated thickness. The anomalies for the open water fraction are only included in the ice extent plots [a].

For every sector, certain trends are exposed through these figures. The IT and AT values vary depending on the inclusion of open water. Open water contributes to the area or fraction of the cell coverage, but it has a zero thickness contribution. The effect of open water on the two calculations is different; compared to AT, the ATOW is only a smoother line with a lower thickness value, but they have similar general curve shapes and temporal peaks. However, compared to IT, ITOW varies considerable by season and sector. Seasonal patterns of the sea ice thickness distribution are apparent, but event-driven anomalous thickness patterns are also retained. The integrated thickness value is almost always higher than the average thickness value, and the primary exception is where there are large open water fractions. IT is always larger than AT, and ITOW is mainly smaller than ATOW in the summer when there are large open water fractions. On a climatological scale, ATOW and ITOW follow each other more closely than AT and IT. Ocean-wide trends are also found in the anomaly plots. Towards the end of 1995 and the beginning of 1996, there is an anomalously large thickest ice category in the thickness distribution. It is suspected that some sector-wide trends are associated with circulation changes in some years. These will be briefly examined by sector in the following sections.

6.2.1 Sea Ice Thickness Distribution in the Eastern Weddell Sea Sector

This analysis begins with the Eastern Weddell Sea Sector because it contains some features which appear across much of Southern Ocean. The region-specific results for the Eastern Weddell Sea sector are given in figures **6.1** – **6.3**. Despite the small area and proximity of the two Weddell Sea regions, the appropriateness for separating the two sectors for analysis is apparent. The Eastern Weddell Sea is less

dominated by thick ice, and the seasonal freeze and melt cycles of the thinner ice categories are more noticeable.

In the climatology plots, the AT/ATOW (thick dashed line) in the ice area plot exhibits a fairly steady seasonal thickness. IT/ITOW, however, really captures the sea ice variability. Note that this is a thickness and thickness distribution per area which means that in the summer the thin ice melts and the thickest ice categories are retained. The mean thickness in the summer should reflect that, and the IT without open water does.

An interesting result appears clearly in this sector from a comparison of the ice extent versus ice area plots by week for all four years. This pattern is not obvious when examining the West Weddell Sea due to the predominant thick ice fraction, but it occurs throughout the Southern Ocean. The AT value shows a decided seasonal peak and trough pattern in the East Weddell more so than in the West Weddell.

The ITOW of the ice extent is not identical to the ATOW, but the two are in phase in terms of the time of the peaks and troughs. However, the IT of ice area peaks later than the AT (not in phase). Average thickness peaks around October while the integrated thickness peaks after February. This is interesting because it highlights what these values actually reflect; they are a thickness per area, and as such they should be highest when the thin ice categories are minimized and the thickest ice only remains. It is interesting to note the difference in IT and AT in the summer. There is large polynya in the Weddell sea that is characterized here by the open water summer fraction.

In the anomaly plots the thickness distributions are shown in the solid lines and the integrated and average thickness in the dotted lines with the distribution anomalies

axis ranging from zero to plus or minus 20%, and the thickness axis ranging from zero to plus or minus two meters. Time (weeks in four years) is along the x-axis.

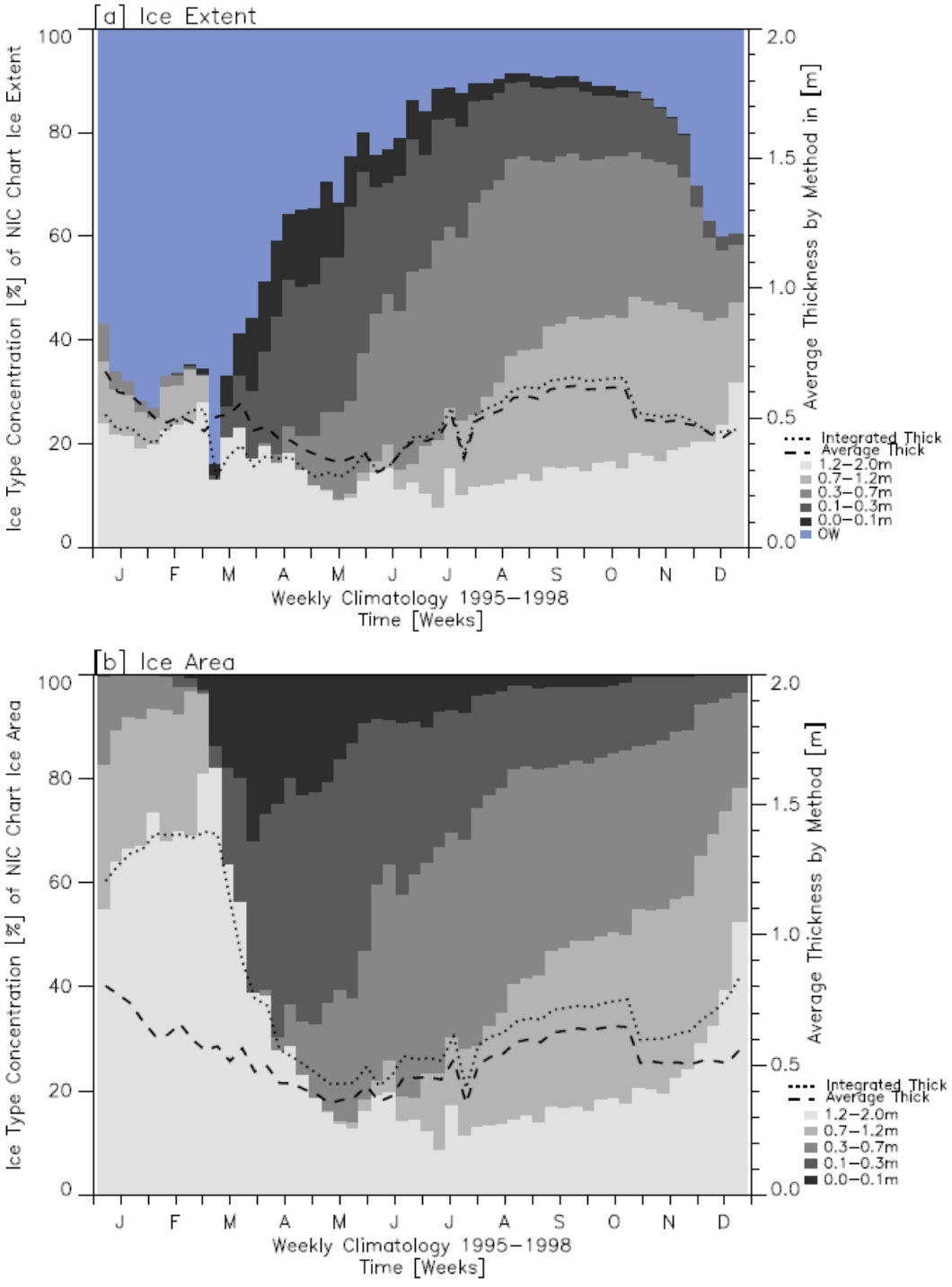

Figure 6.1: E. Weddell Sector Sea Ice Thickness and Distribution Climatology for Ice Extent[a] and Ice Area[b].

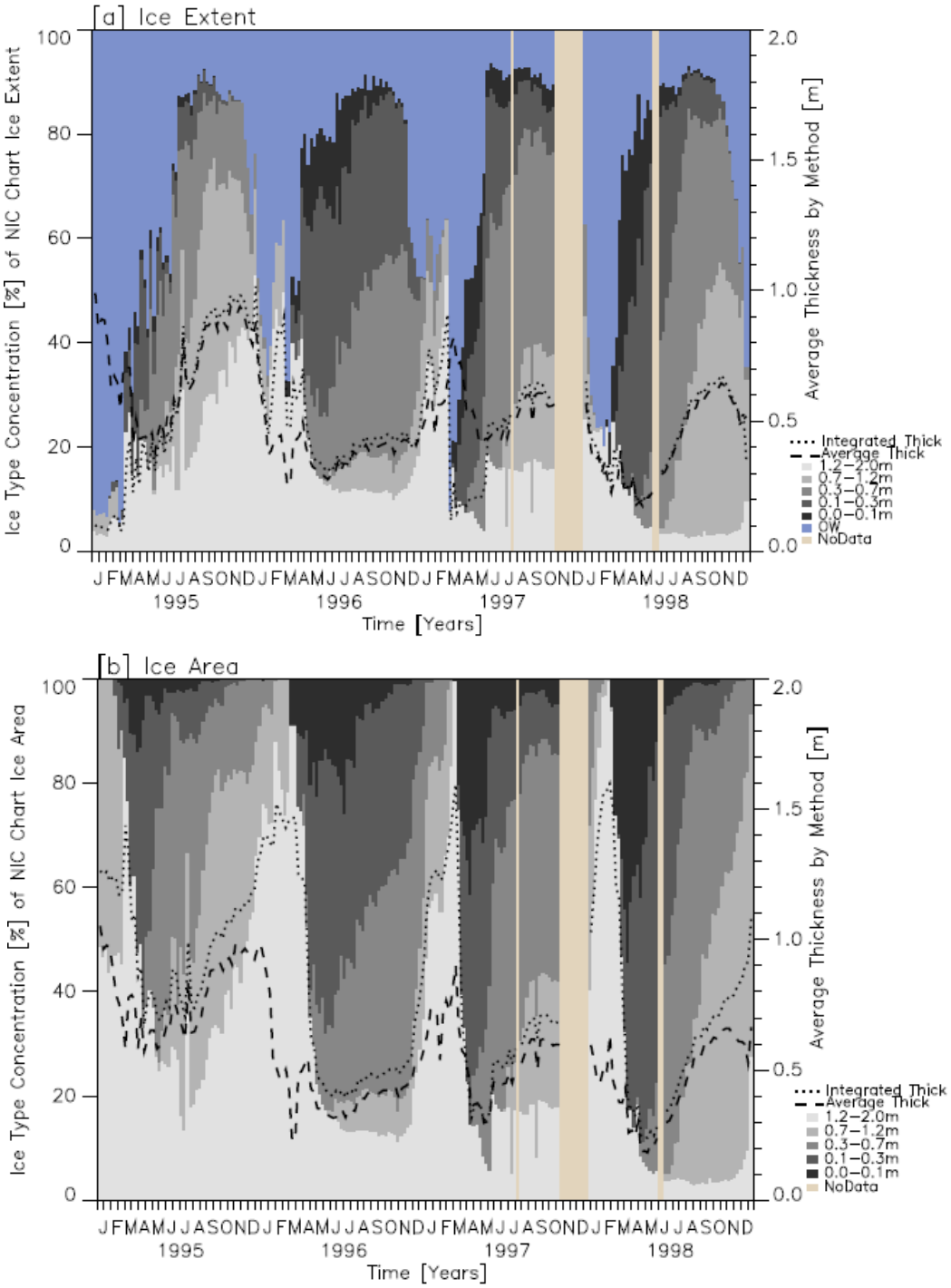

Figure 6.2: E. Weddell Sector Sea Ice Thickness and Distribution for Ice Extent[a] and Ice Area[b].

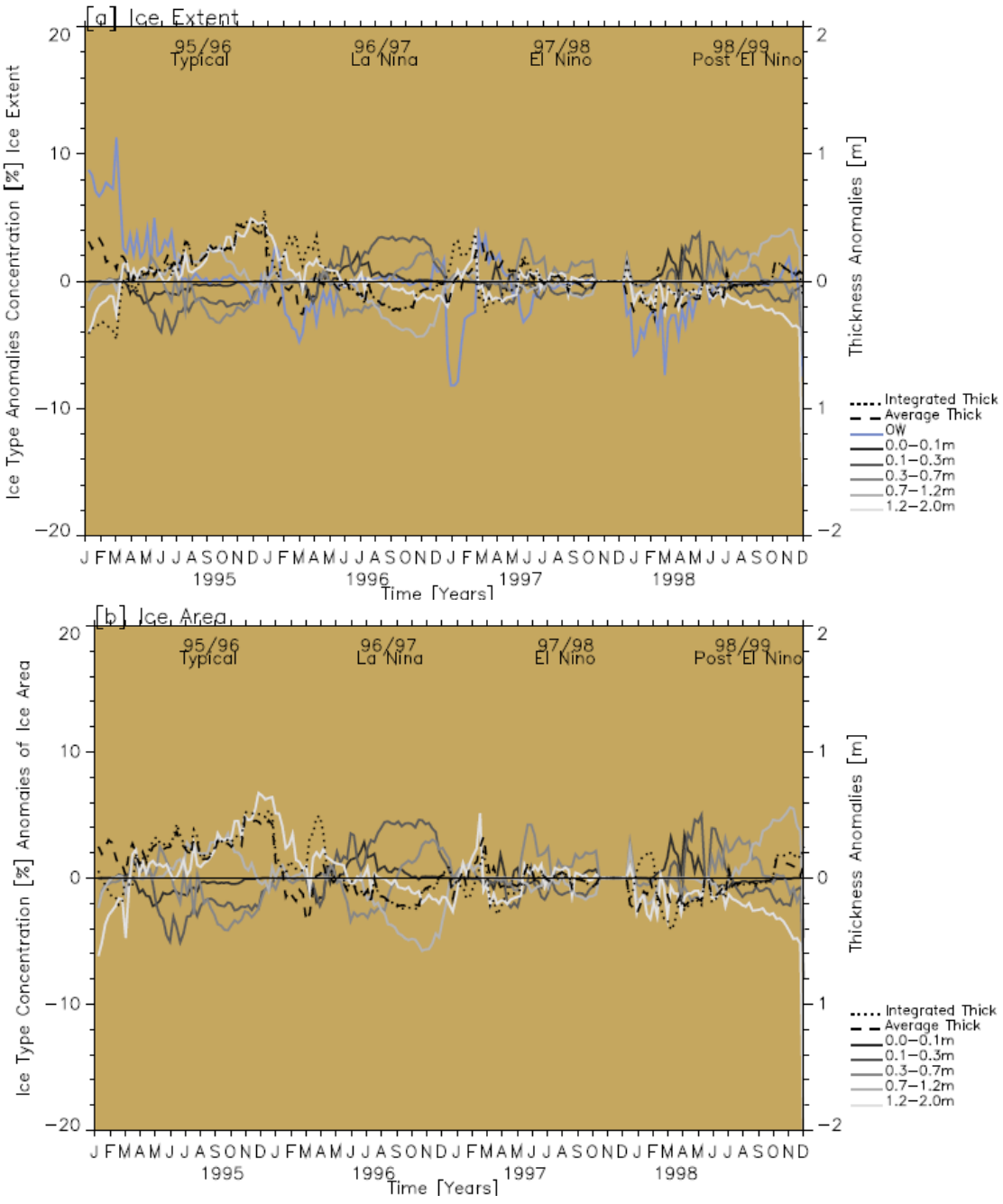

Figure 6.3: E. Weddell Sector Sea Ice Thickness and Distribution Anomalies for Ice Extent[a] and Ice Area[b].

6.2.2 Sea Ice Thickness Distribution in the Indian Ocean Sector

The region-specific results for the Indian Ocean sector are given in figures **6.4 – 6.6**. In the Indian Ocean sector, the seasonal cycle of the AT is fairly uniform for all years, but the IT is less clear. IT shows considerably more weekly variability than the AT value, which further supports the idea that the integrated thickness calculation captures more detail, emphasizing the variability. IT also follows the lag in maximum thickness first considered in the East Weddell Sea. Here the average thickness peaks in October or November, yet the IT without open water peaks some time in the summer. This sector shows a marked seasonal cycle through plots of the thickness distribution, AT/ATOW, and IT/ITOW.

In the anomalies plot, one notable feature is the anomalously large open water fraction in 1995 just before winter. This is an interesting feature to compare against other data source. Also notable are the anomalously low thick ice and large open water fractions in April 1998 when very little thick ice survived the summer and the distribution was dominated by thinner ice types.

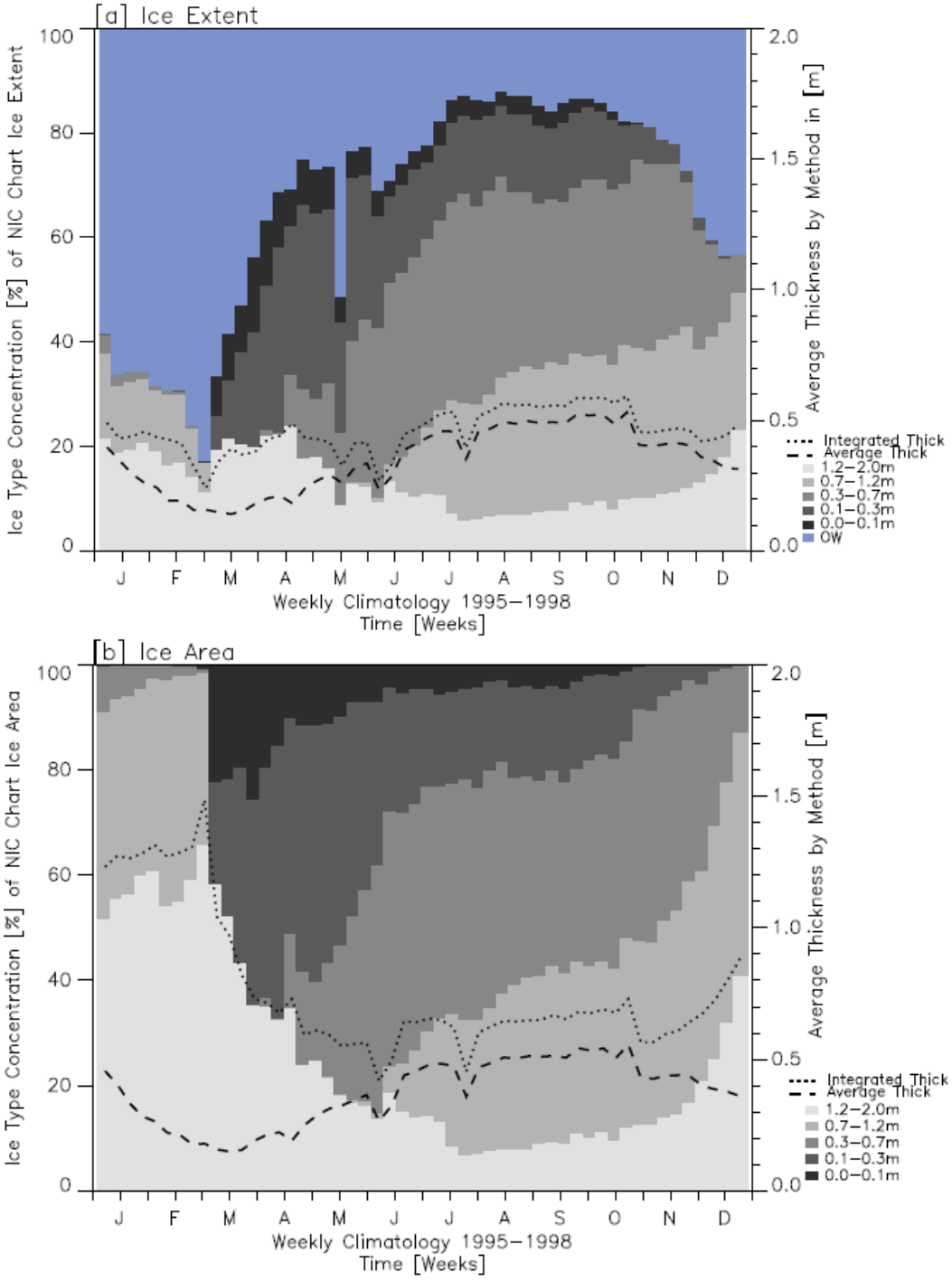

Figure 6.4: Indian Sector Sea Ice Thickness and Distribution Climatology for Ice Extent[a] and Ice Area[b].

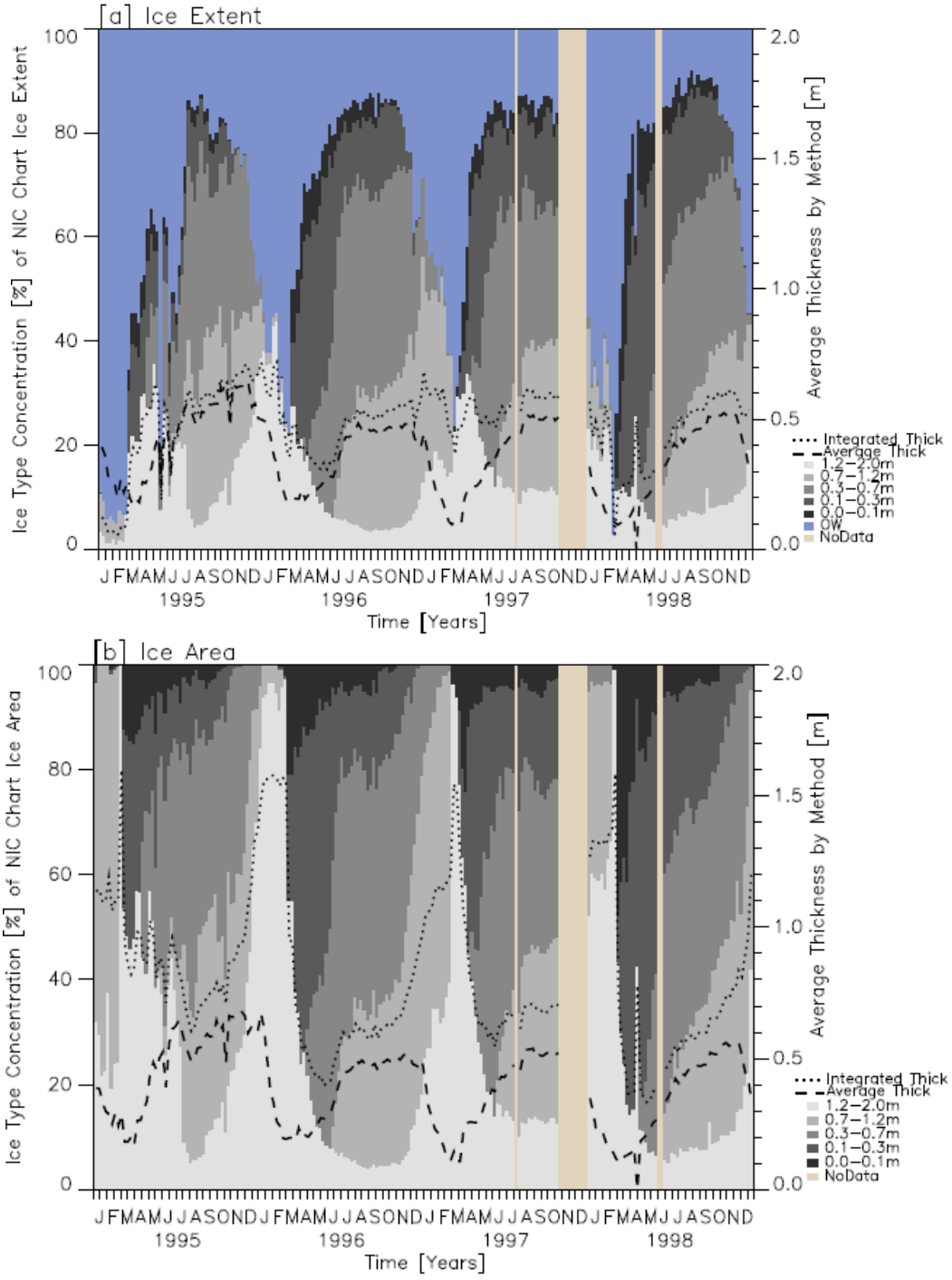

Figure 6.5: Indian Sector Sea Ice Thickness and Distribution for Ice Extent[a] and Ice Area[b].

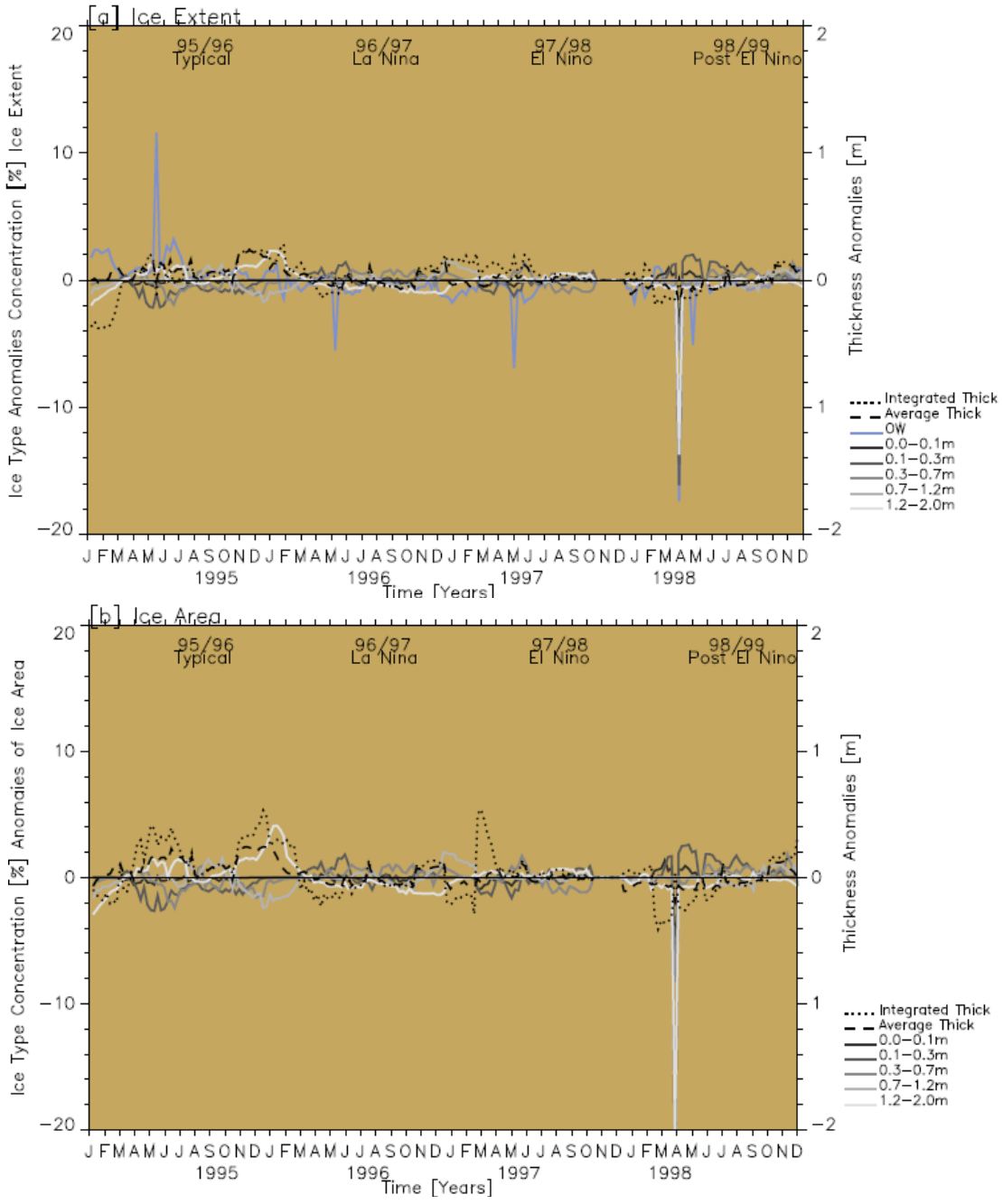

Figure 6.6: Indian Sector Sea Ice Thickness and Distribution Anomalies for Ice Extent[a] and Ice Area[b].

6.2.3 Sea Ice Thickness Distribution in the Pacific Ocean Sector

The region-specific results for the Pacific Ocean sector are given in figures **6.7 – 6.9**. Although the Indian and Pacific Sectors together represent the largest geographic East-West area extent of any two sectors, they are the most similar in thickness distribution and mean thickness values in the climatology as well as the weekly distributions. This is expected as the similarity of the two sectors has been previously documented (Worby et al 2008).

The two regions show the same seasonal cycle in the thickness distribution and AT/ATOW. They also both show the characteristic IT peak lag from AT. The notable anomalies apparent in the Indian Ocean Sector also appear in the Pacific Ocean sector, except here, they occur in slightly different weeks.

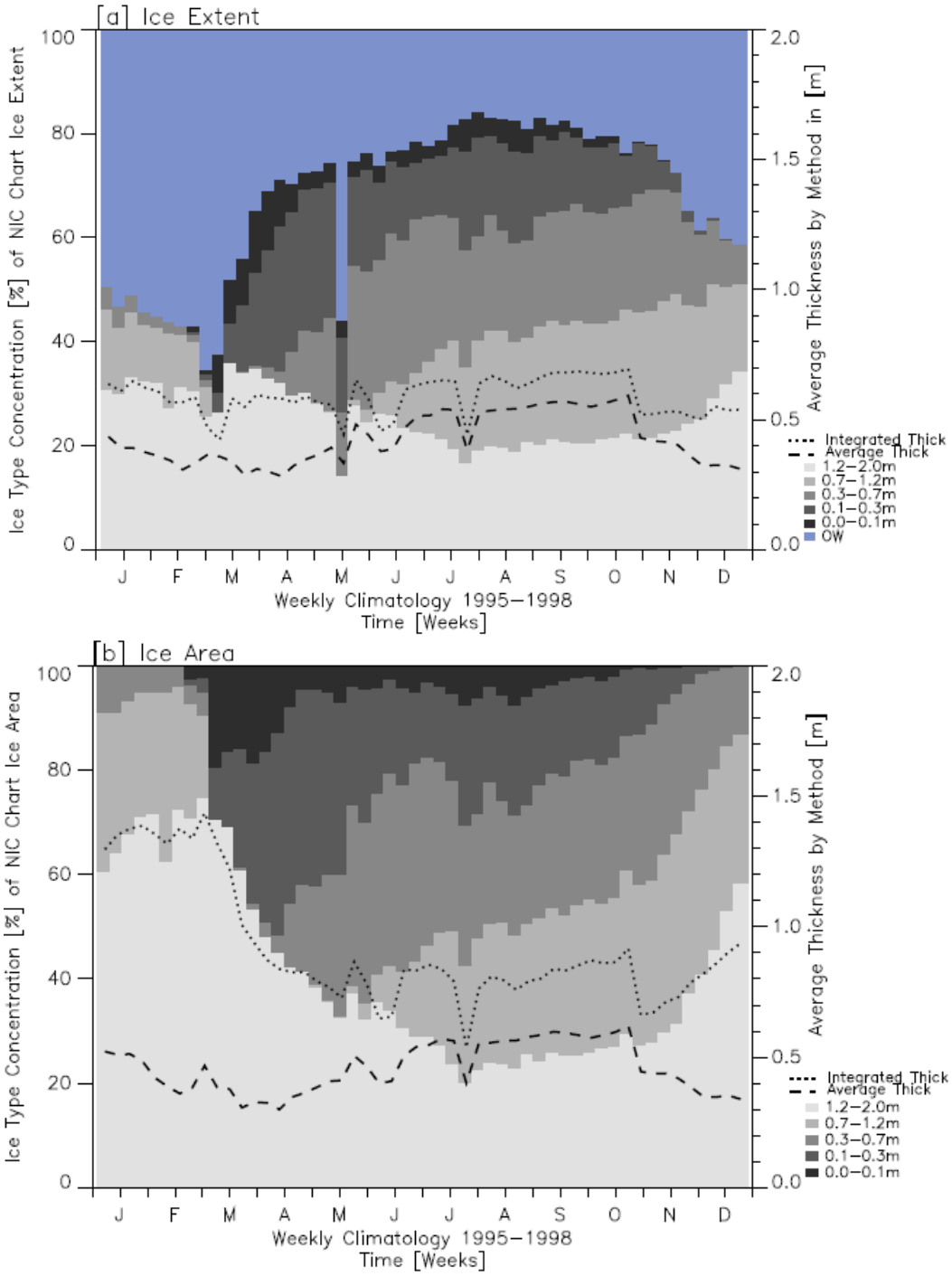

Figure 6.7: Pacific Sector Sea Ice Thickness and Distribution Climatology for Ice Extent[a] and Ice Area[b].

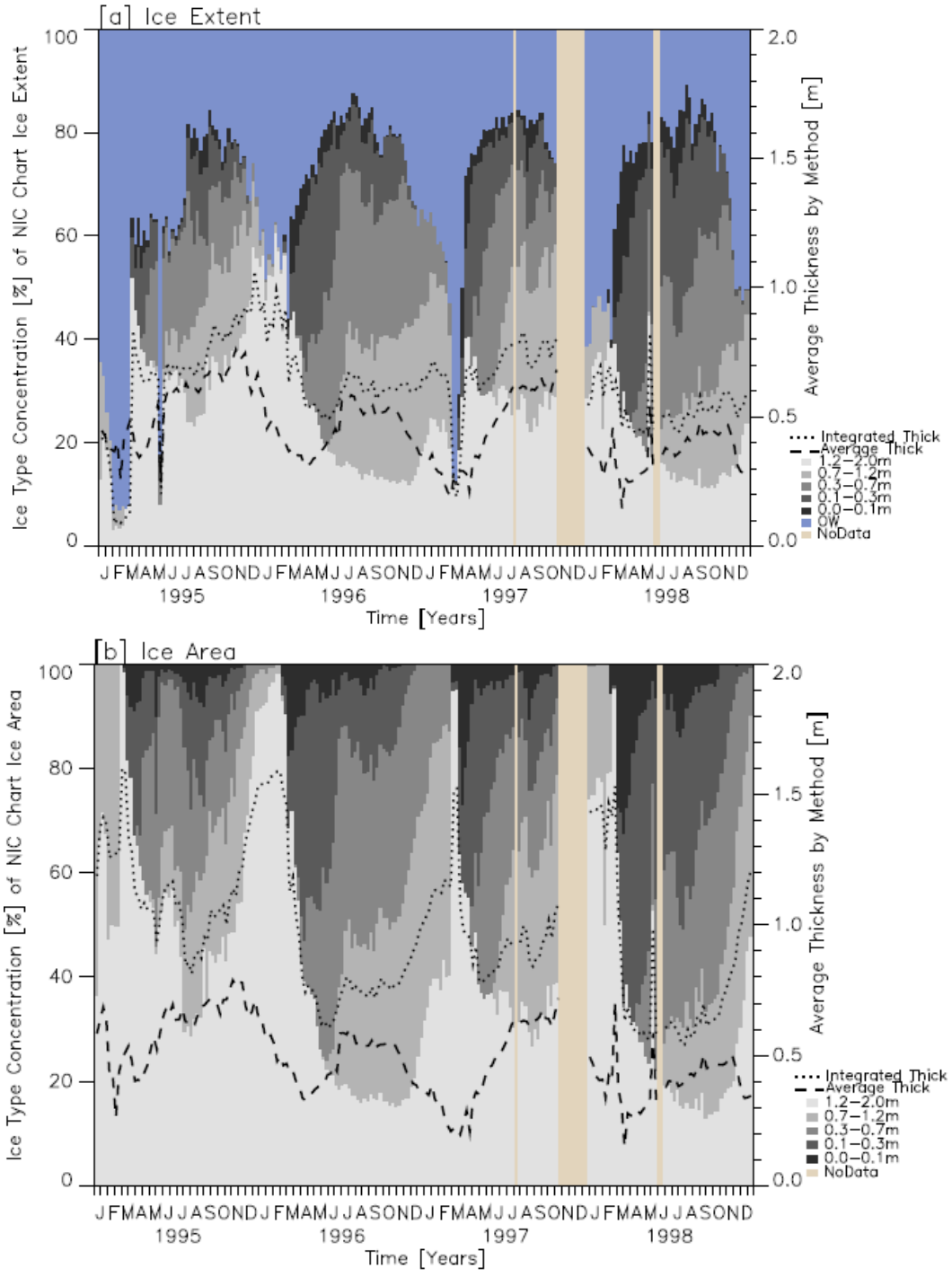

Figure 6.8: Pacific Sector Sea Ice Thickness and Distribution for Ice Extent[a] and Ice Area[b].

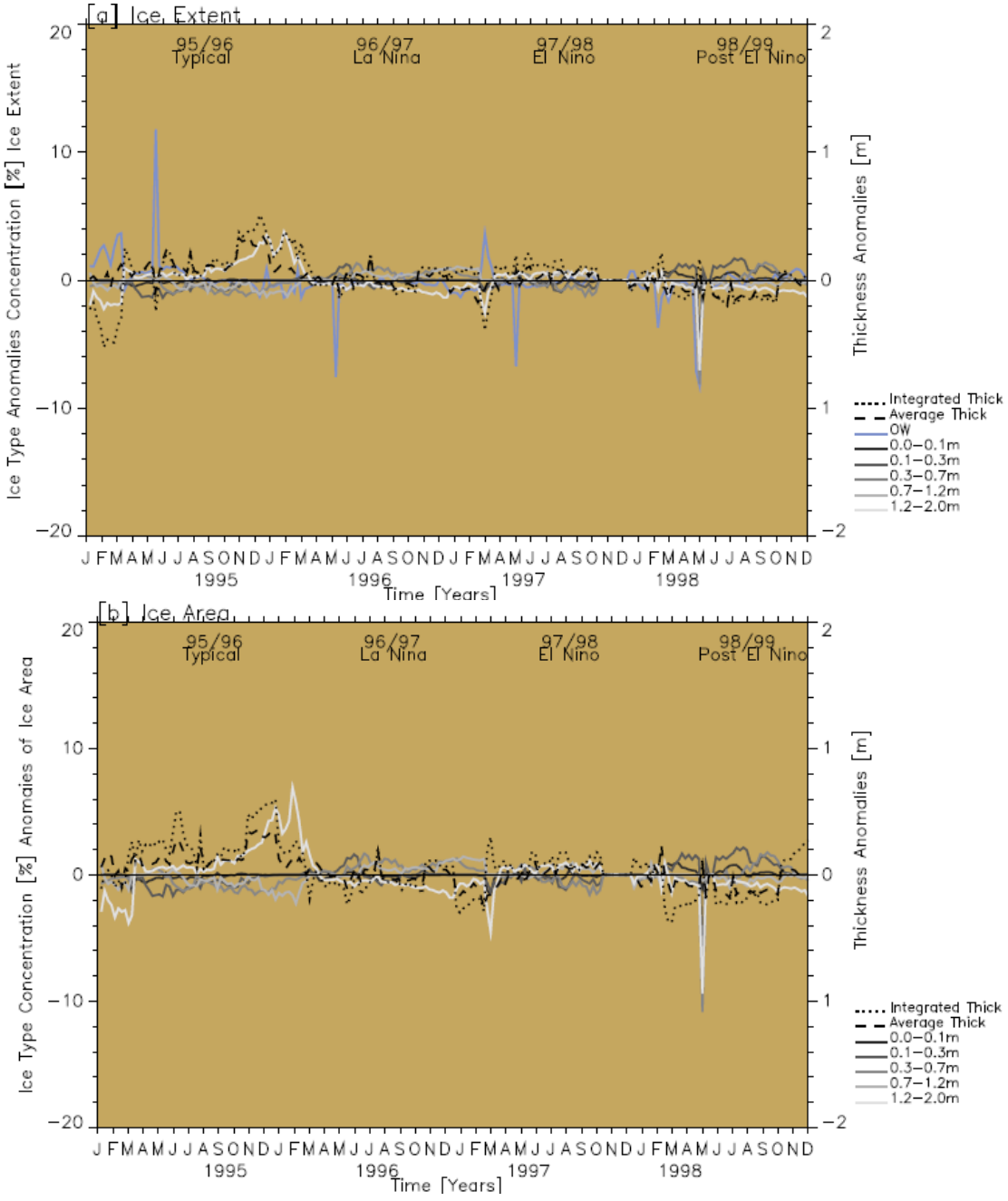

Figure 6.9: Pacific Sector Sea Ice Thickness and Distribution Anomalies for Ice Extent[a] and Ice Area[b].

6.2.4 Sea Ice Thickness Distribution in the Eastern Ross Sea Sector

The region-specific results for the East Ross Sea sector are given in figures **6.10** – **6.12**. The seasonal cycle of thickness distribution is very clear in the Eastern Ross Sea. Following the summer melt period when only thick ice and open water are major features, the thin ice categories start to develop in autumn. The fraction dominated by the thinnest ice categories decreases by winter, while the fraction dominated by the middle thickness categories increases. This highlights the growth of ice thickness and the redistribution of ice into thicker categories as the winter persists. At the end of the winter there is a sudden, pronounced decrease in the fraction of all ice types except for the thickest ice which remains year-round.

The East Ross Sea 1996 – 1997 open water bin negative anomaly is due to the larger than average summer ice extent with more thin ice retained than normal. In the ice area anomaly plot, this feature is identifiable through the integrated thickness per area value. In the summer 1996 – 1997 the higher thin ice fraction leads to a smaller than AT/ATOW.

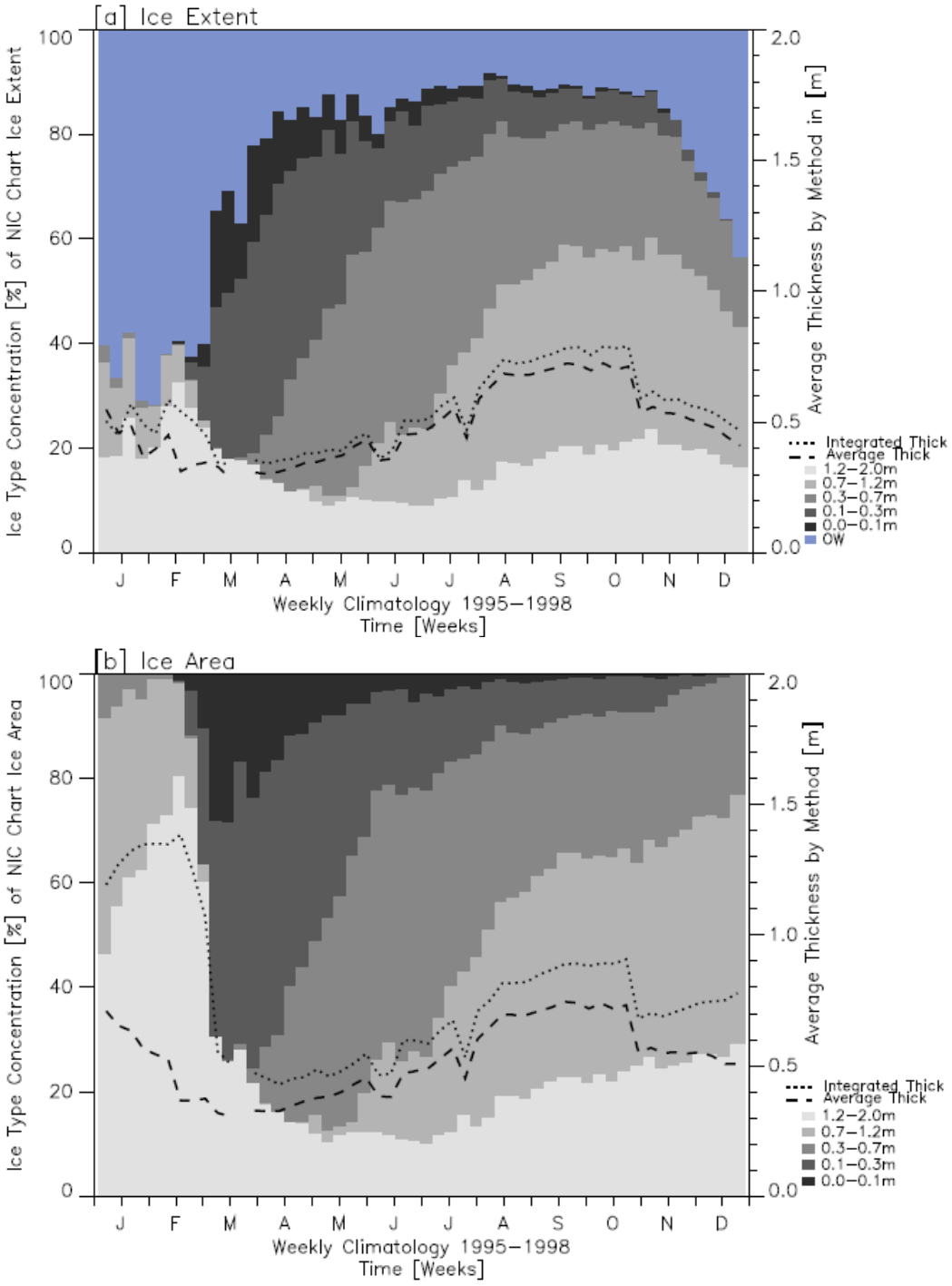

Figure 6.10: E. Ross Sector Sea Ice Thickness and Distribution Climatology for Ice Extent[a] and Ice Area[b].

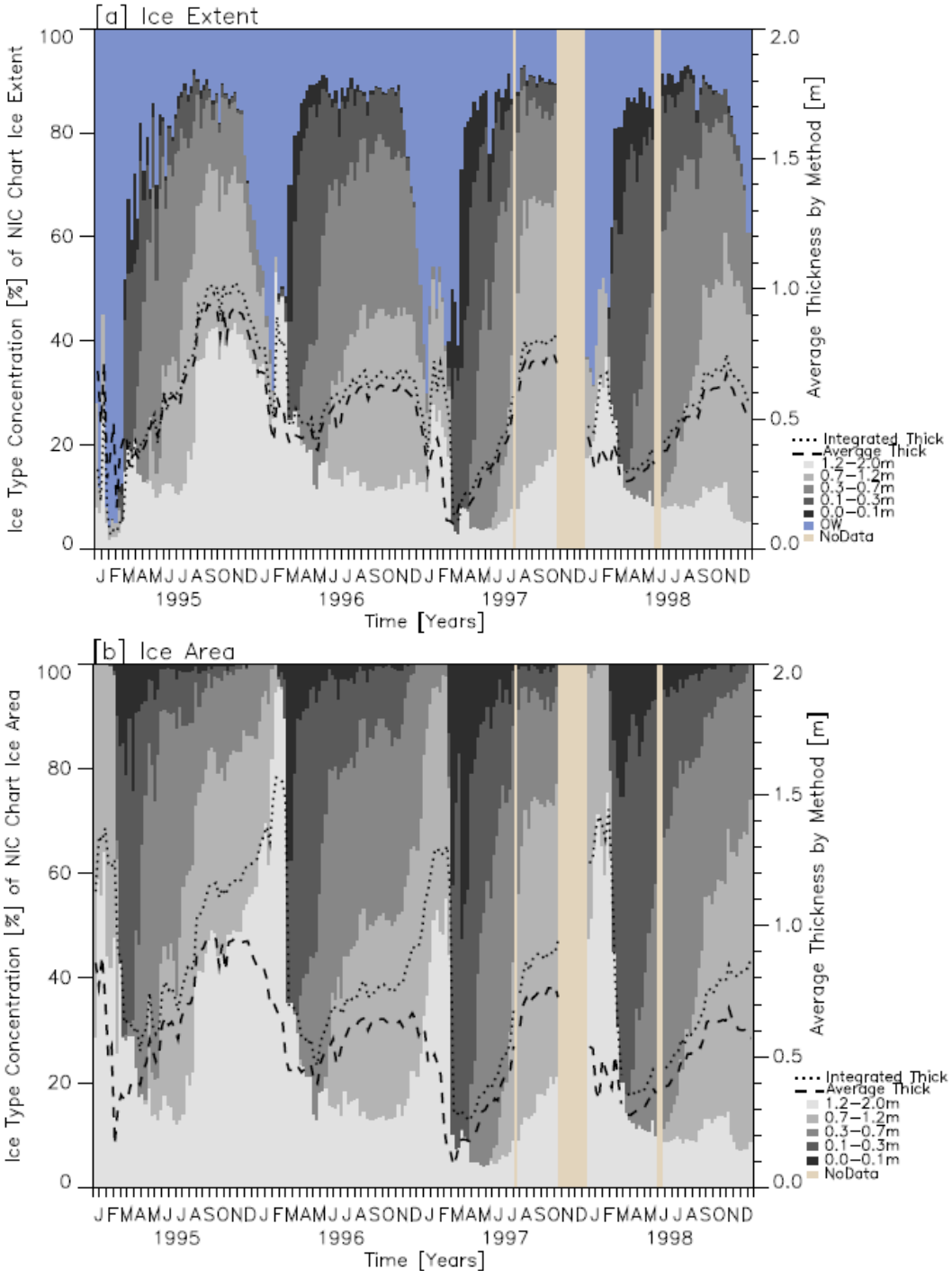

Figure 6.11: E. Ross Sector Sea Ice Thickness and Distribution for Ice Extent[a] and Ice Area[b].

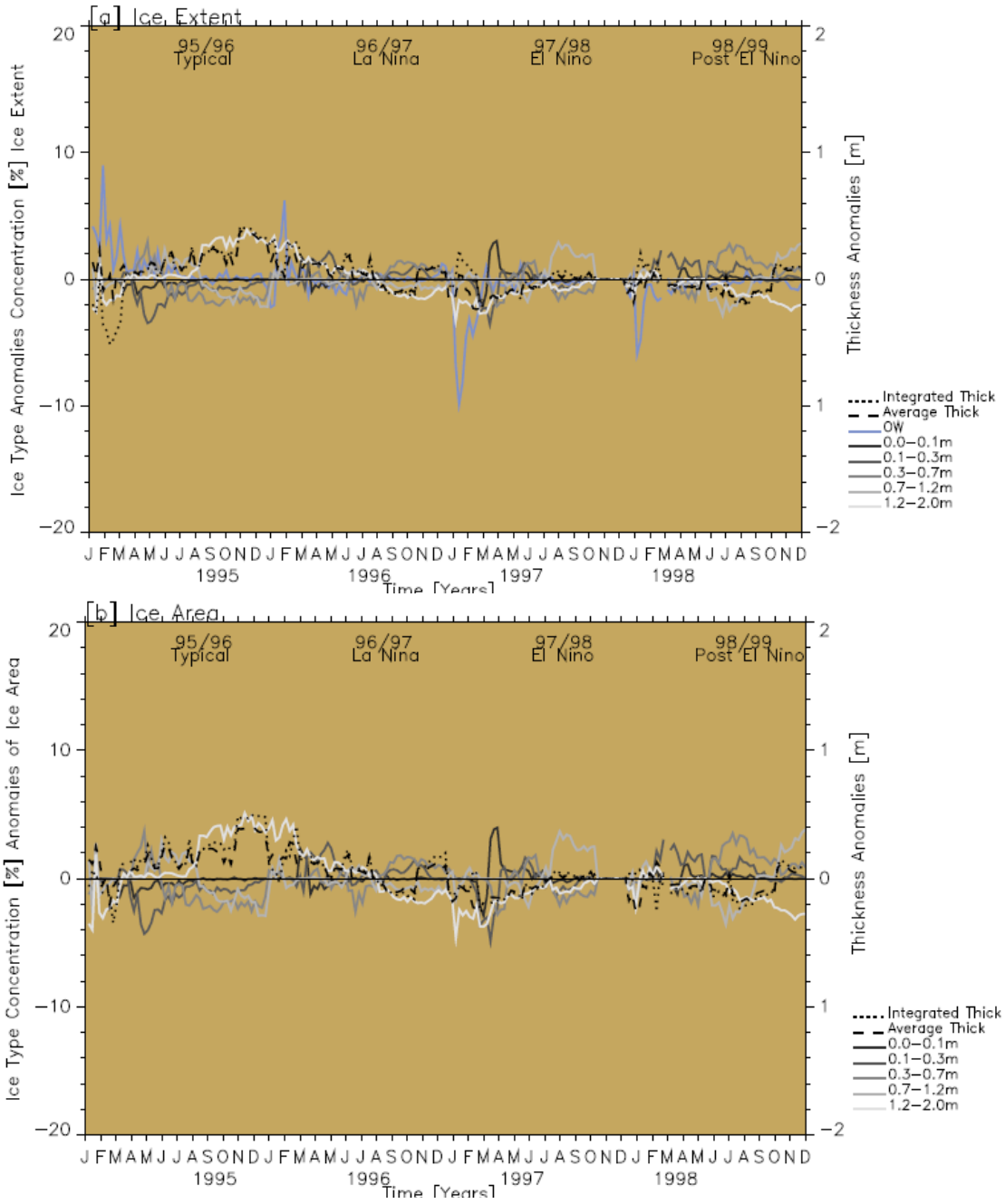

Figure 6.12: E. Ross Sector Sea Ice Thickness and Distribution Anomalies for Ice Extent[a] and Ice Area[b].

6.2.5 Sea Ice Thickness Distribution in the Western Ross Sea Sector

The region-specific results for the Western Ross Sea sector are given in figures **6.13** – **6.14**. While the Eastern Ross Sea exhibits some of the same patterns as the Indian and Pacific Ocean sectors (pronounced seasons, 1998 average thickness anomaly), the Western Ross Sea sector behaves as a transition sector from the cyclical sea ice thickness by seasons to the east, and the stable conditions dominated by year-round thick ice to the west in the Bellingshausen, Amundsen, and Western Weddell Seas.

In the Western Ross Sea, seasonal cycles in the average thickness per area value are slightly less pronounced than in the East Ross Sea. Particularly in 1996, a fairly even division of ice thickness categories show more stable ice distribution conditions than in the Eastern Ross Sea Sector. The thick ice fraction is larger in the Western Ross Sea, than in the previous sector. ATOW and ITOW appear very stable year round. The only distinct seasonal pattern occurs in the sea ice thickness distribution without open water where the thin ice melt leads to a high percentage of thick ice in the summer.

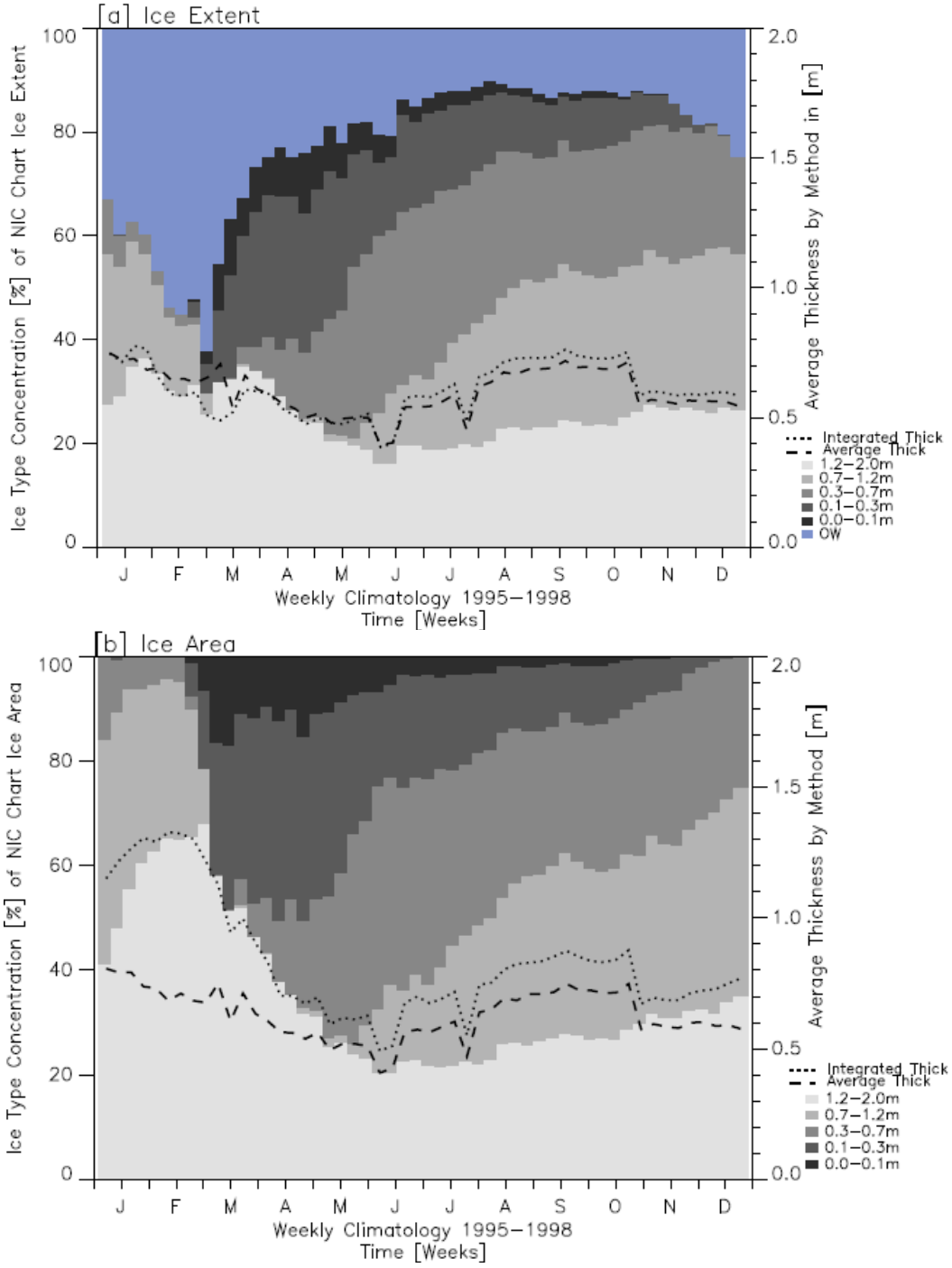

Figure 6.13: W. Ross Sector Sea Ice Thickness and Distribution Climatology for Ice Extent[a] and Ice Area[b].

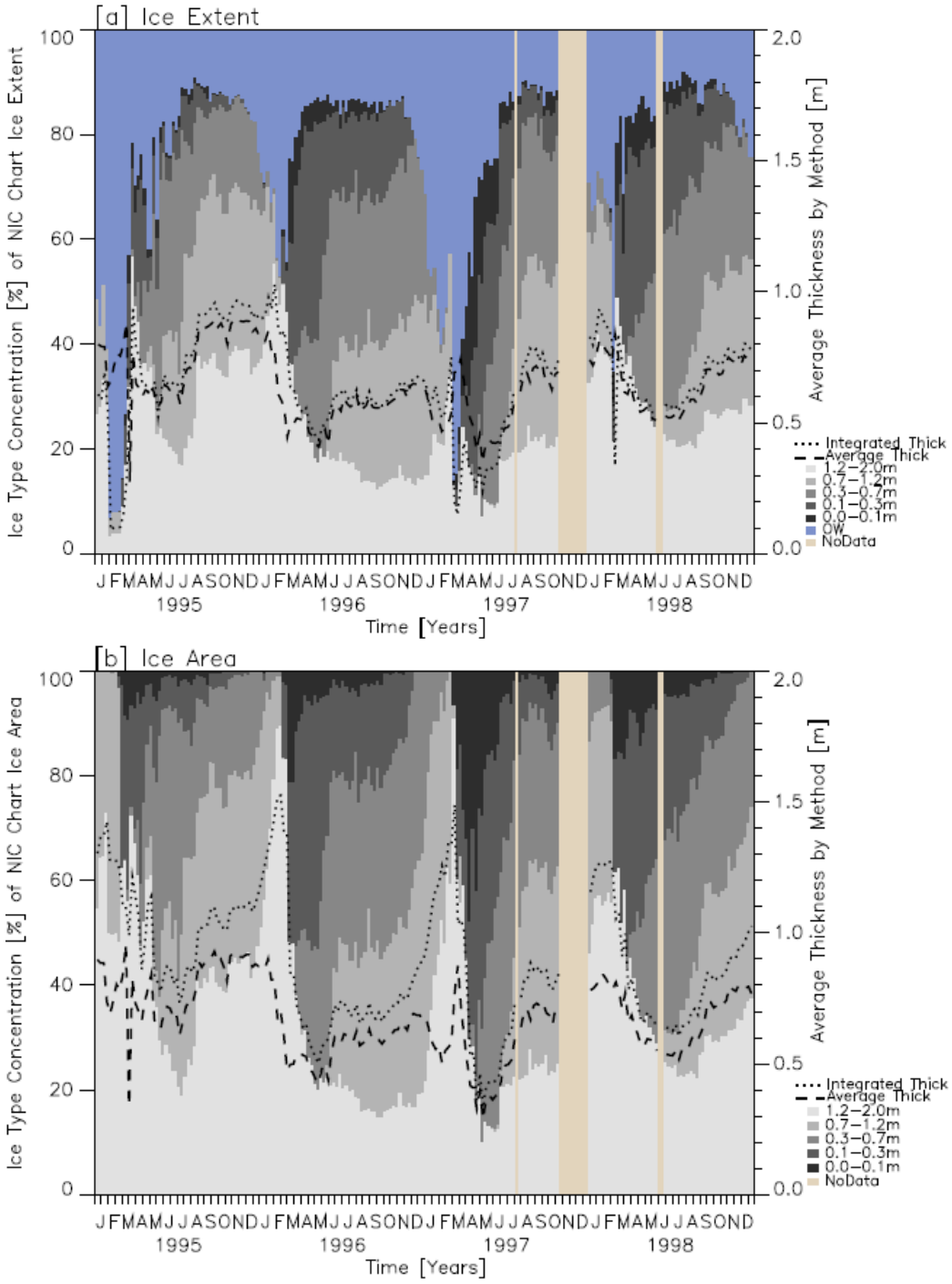

Figure 6.14: W. Ross Sector Sea Ice Thickness and Distribution for Ice Extent[a] and Ice Area[b].

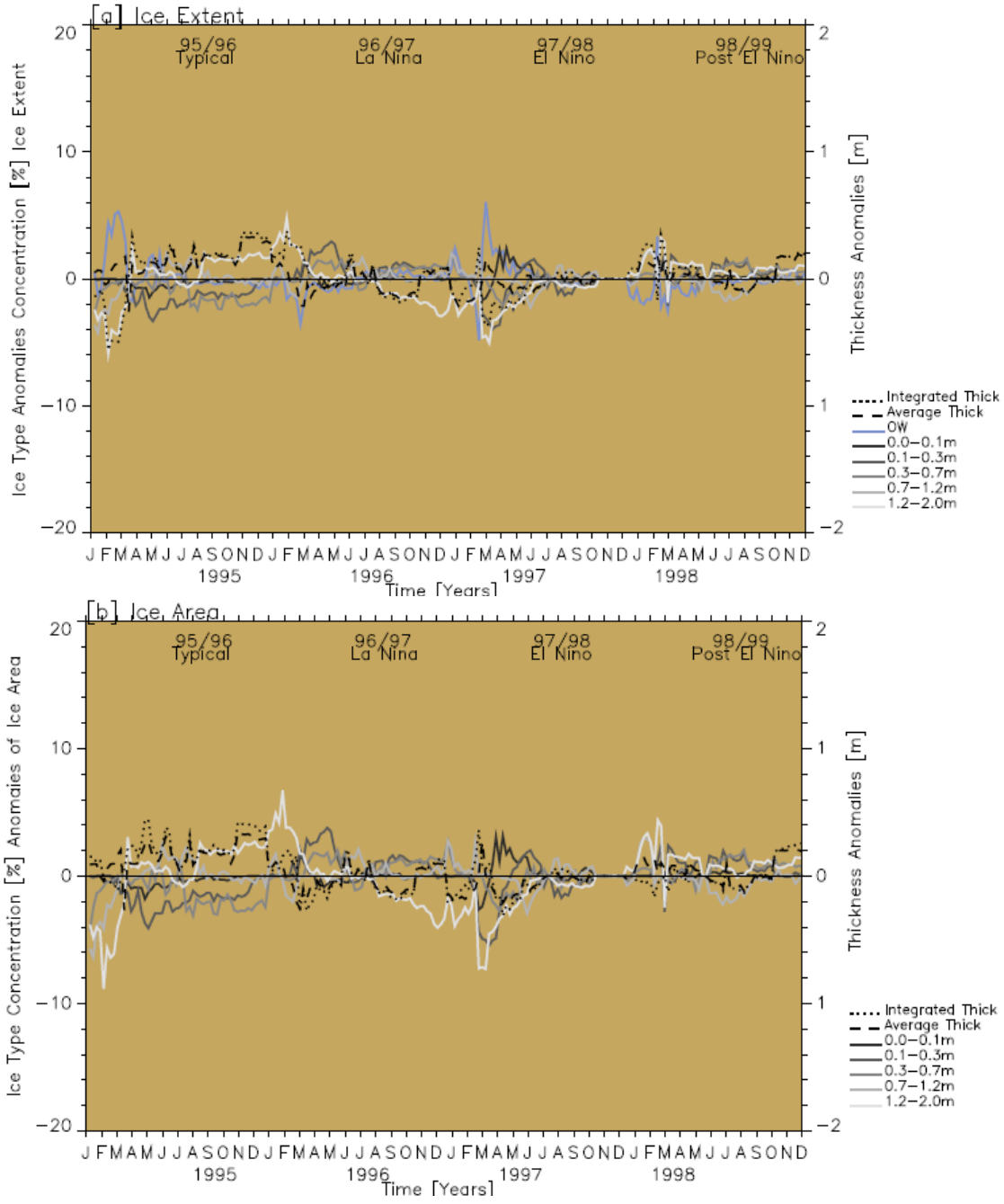

Figure 6.15: W. Ross Sector Sea Ice Thickness and Distribution Anomalies for Ice Extent[a] and Ice Area[b].

6.2.6 Sea Ice Thickness Distribution in the Bellingshausen-Amundsen Sea Sector

The region-specific results for the Bellingshausen-Amundsen Sea sector are given in figures **6.16** – **6.18**. The Bellingshausen-Amundsen Sea Sector has been identified as retaining a large quantity of thick ice year round (Worby et al 2008) and while thick ice does remain year-round, the fraction is not as high as the thick ice fraction observed in the West Weddell Sea. This sector shows similar patterns to the Western Ross Sea sector. No major anomalies stand out in this sector, but in 1995 minimal thin ice formation appears in the thickness distribution record, and every summer except 1996 shows a several week dip with a high open water fraction.

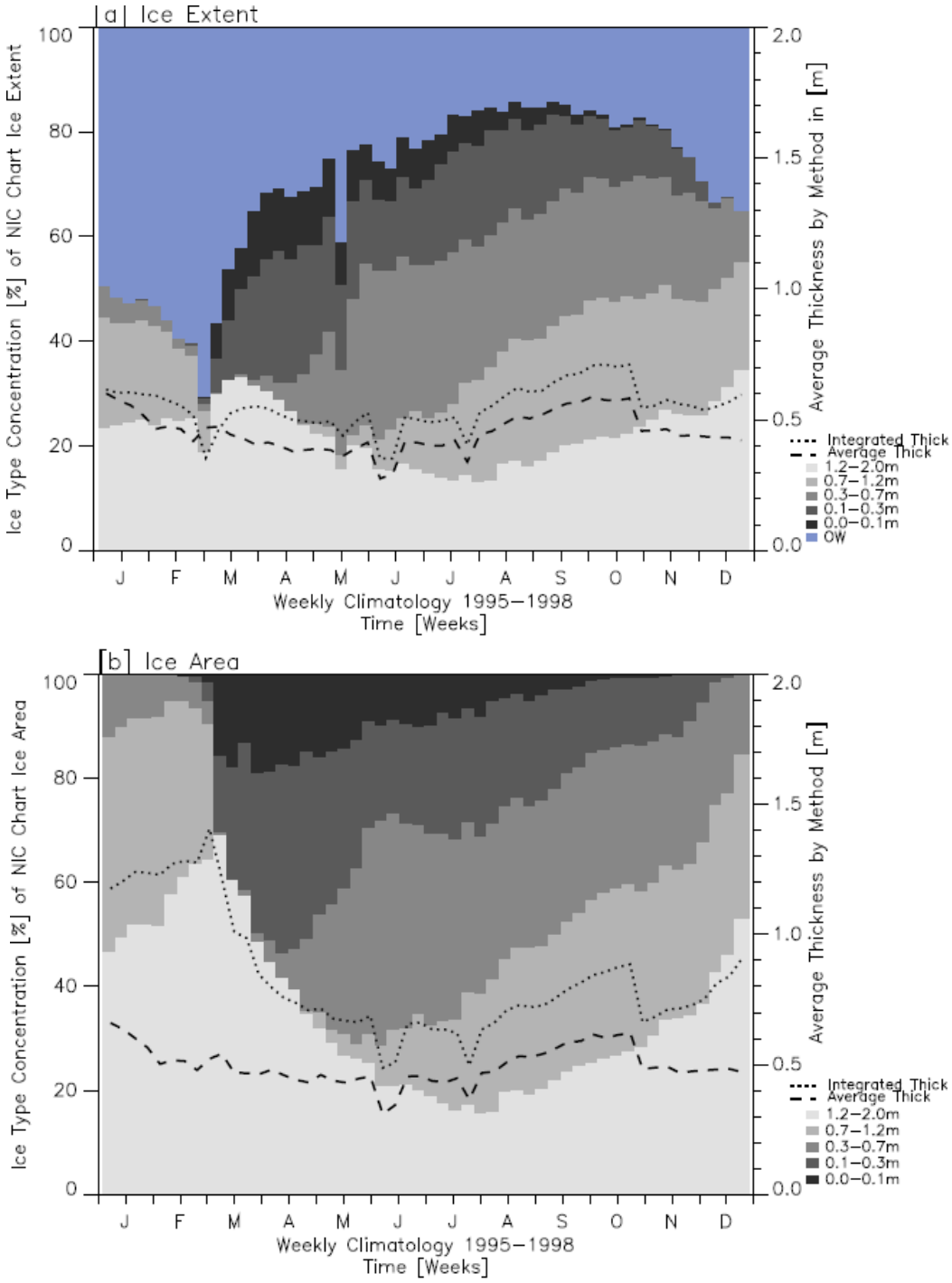

Figure 6.16: Bellingshausen Sector Sea Ice Thickness and Distribution Climatology for Ice Extent[a] and Ice Area[b].

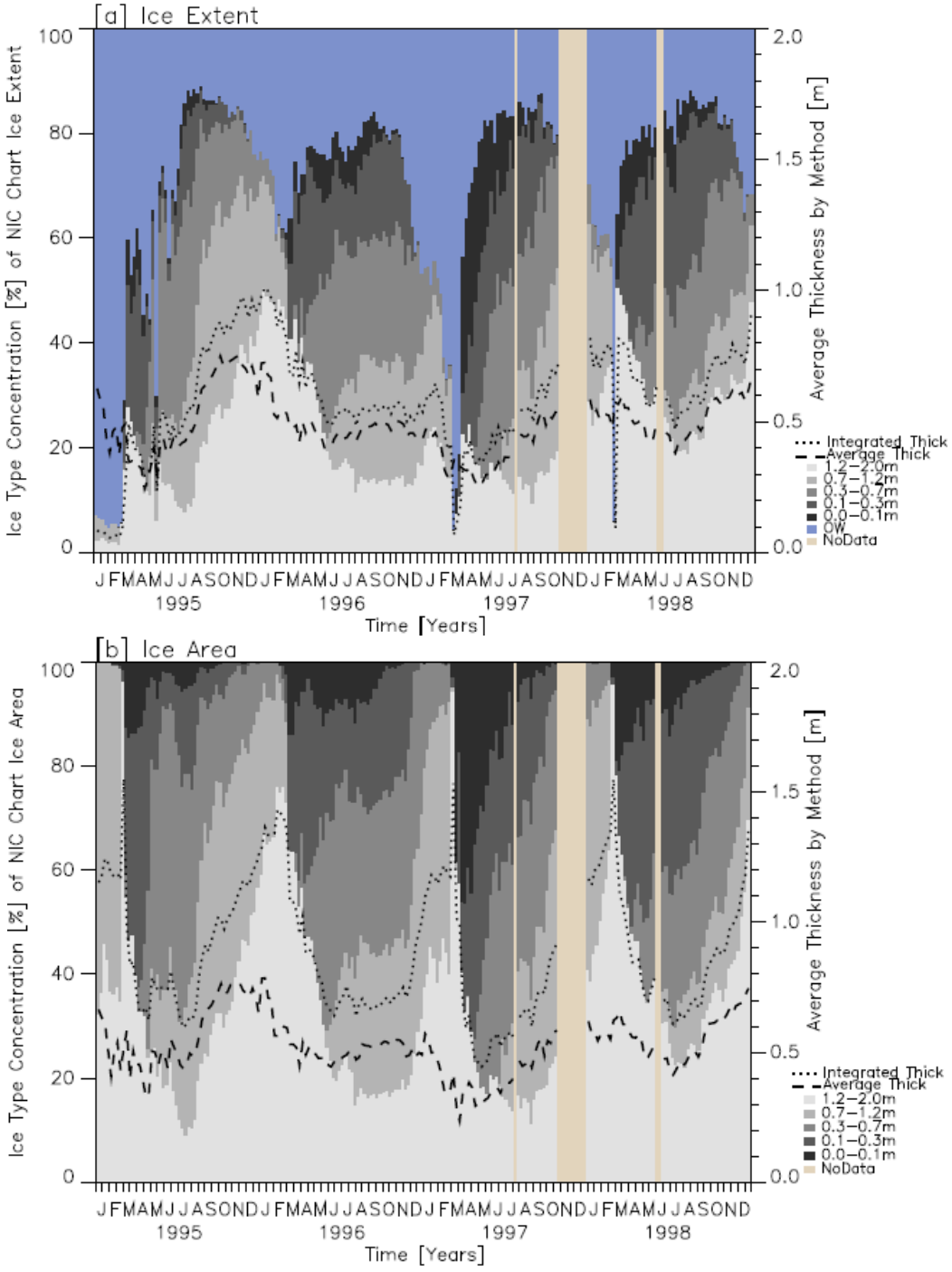

Figure 6.17: Bellingshausen Sector Sea Ice Thickness and Distribution for Ice Extent[a] and Ice Area[b].

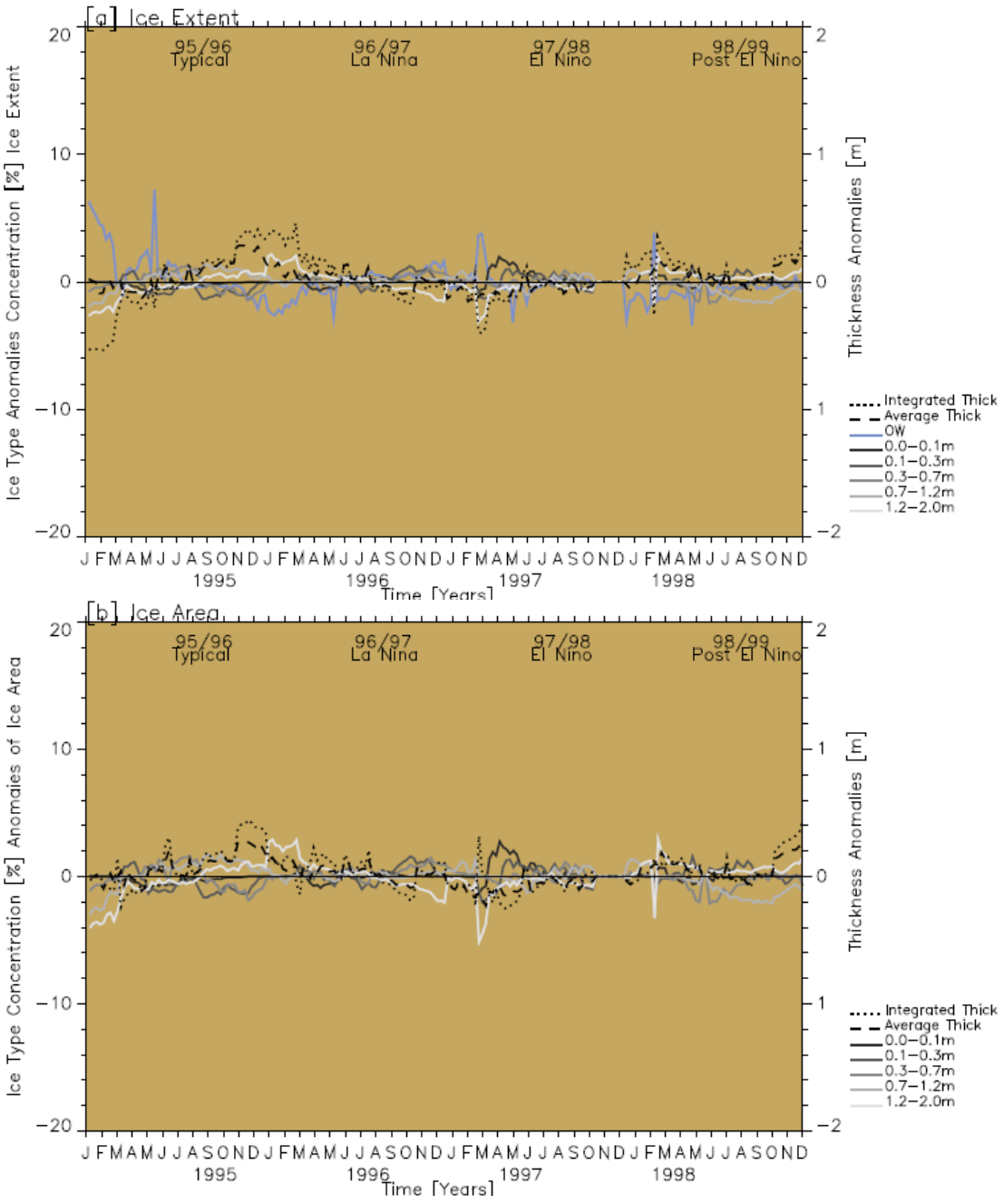

Figure 6.18: Bellingshausen Sector Sea Ice Thickness and Distribution Anomalies for Ice Extent[a] and Ice Area[b].

6.2.7 Sea Ice Thickness Distribution in the Western Weddell Sea Sector

The region-specific results for the West Weddell Sea sector are given in figures **6.19 – 6.21**. The Western Weddell Sea is last because it is the most anomalous sector. In this sector, the most pronounced example of how the average thickness smoothes over areas of open water leads may be seen in figure **6.20 [a]**. In this sector the largest thickness distribution anomalies are the thickest ice bin and open water. Here, the Ronne polynya opens up in the summer and the area is covered by a high open water fraction. In the West Weddell Sea, thick ice and open water anomalies appear to be in phase so that where there are positive open water anomalies there are negative thick ice anomalies and vice versa. This anomaly trend occurs to some extent in other sectors, but it is most prominent in the West Weddell Sea where thick ice and open water dominate the ice extent coverage in the summer. This is because the highest quantities of thick ice of all sectors are retained year-round, and the trend shows the high variability of open water fraction due to the behavior of the Ronne Polynya in the summer.

The two catastrophic shifts in IT/ITOW, and all ice categories except open water in summer of 1995 and 1997 are real (not NIC chart error). These reflect activity leading to the opening of a large polynya. It is interesting to recall that the 1997 – 1998 period was strongly affected by ENSO. Those circulation patterns tend to effect the Weddell Sea by opening up large leads. The missing data weeks here should exhibit some anomalously high open water fractions, and more information on the missing data weeks is needed for further analysis.

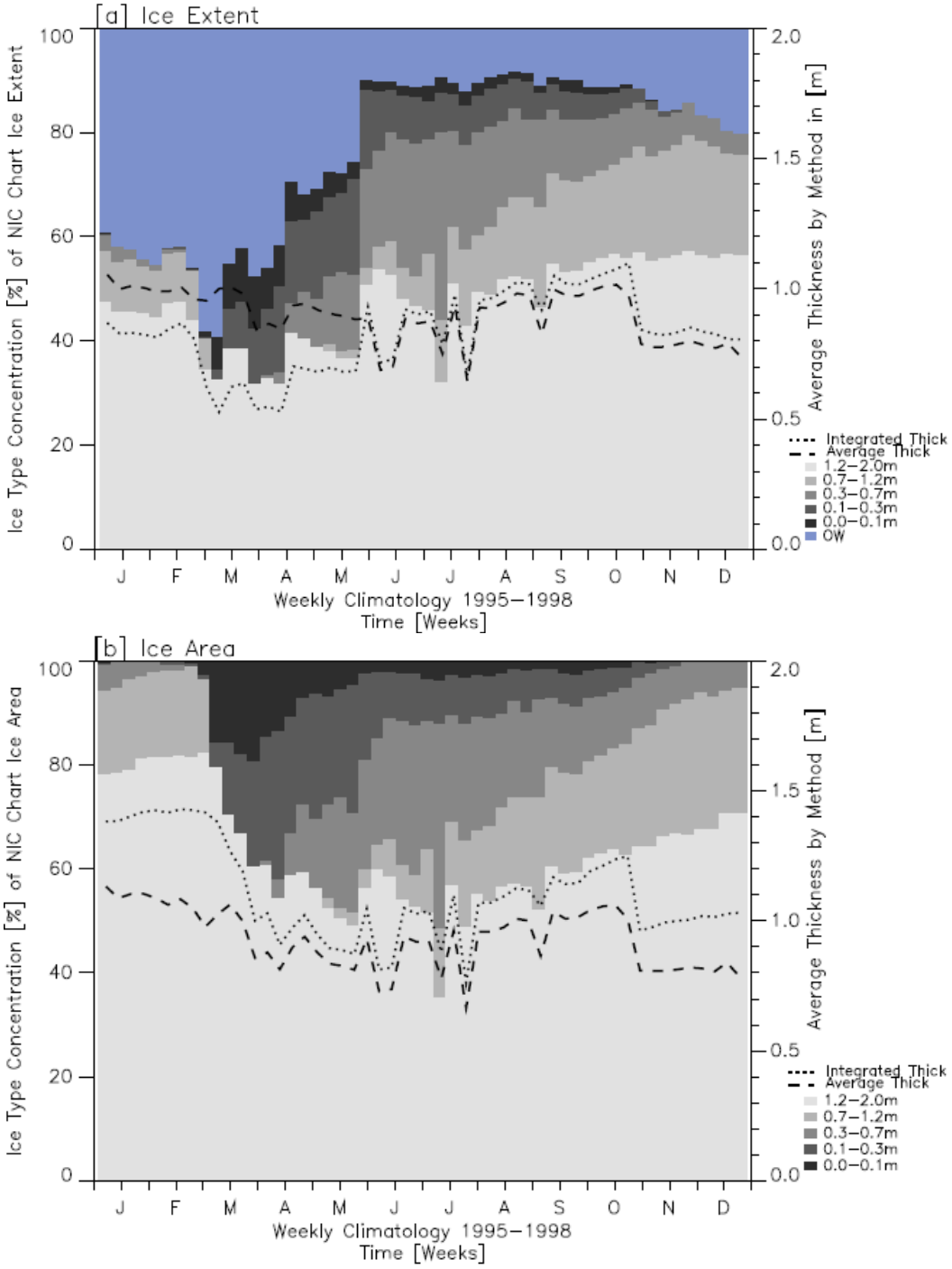

Figure 6.19: W. Weddell Sector Sea Ice Thickness and Distribution Climatology for Ice Extent[a] and Ice Area[b].

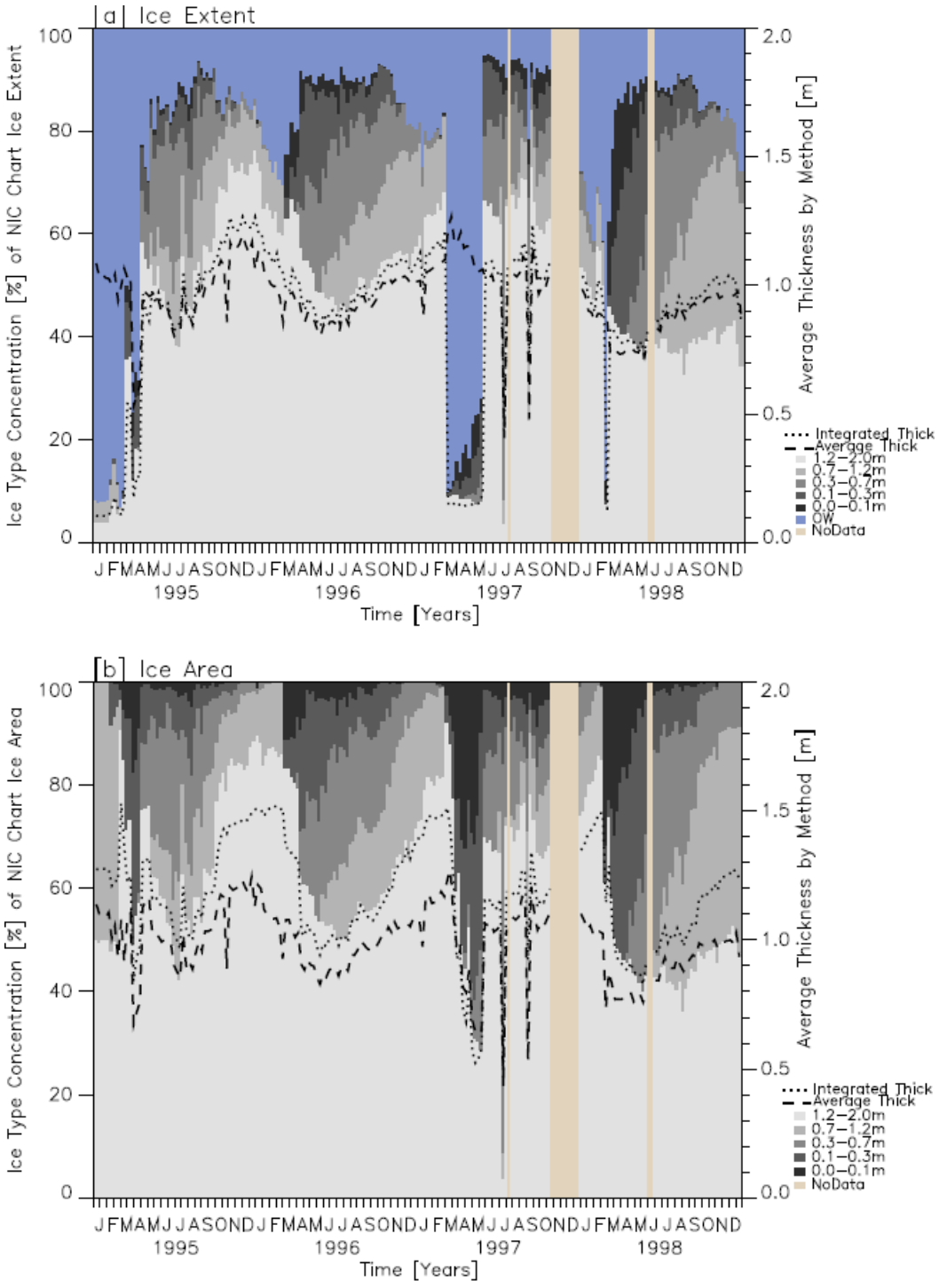

Figure 6.20: W. Weddell Sector Sea Ice Thickness and Distribution for Ice Extent[a] and Ice Area[b].

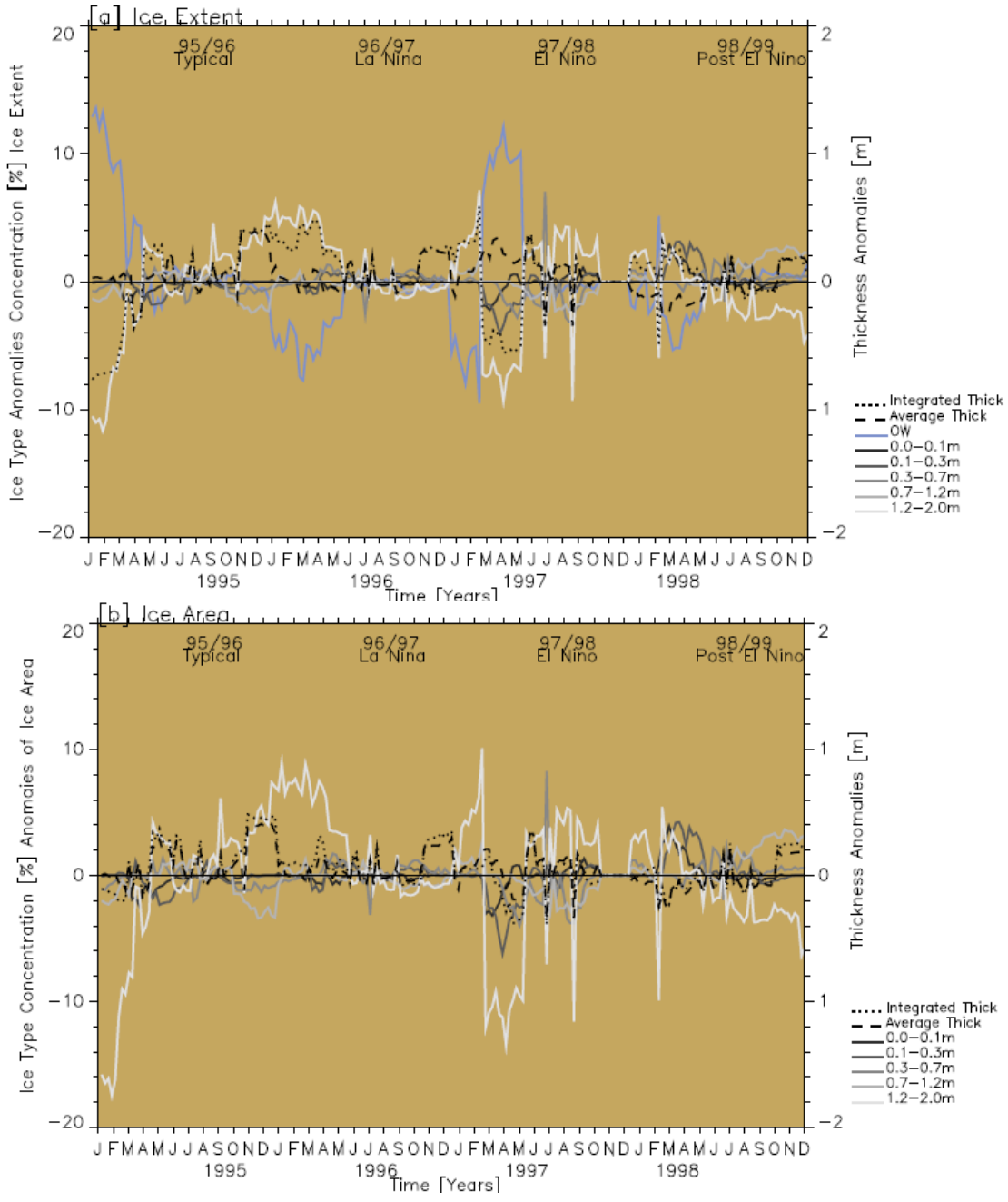

Figure 6.21: W. Weddell Sector Sea Ice Thickness and Distribution Anomalies for Ice Extent[a] and Ice Area[b].

6.3 Results of Science Question 2 by Thickness Method

The previous section examined the sea ice thickness distribution and the methods for calculating sea ice thickness per area with focused results by region. The visualization focused by region provided several illustrations of the differences between AT, ATOW, IT, and ITOW. The IT and AT values vary depending on the inclusion of open water, which contributes area but not thickness. The integrated thickness value is almost always higher than the average thickness value, and the primary exception to this occurs with the large open water fractions. This section further examines the differences between ITOW and ATOW as well as IT and AT by focusing on comparisons of the method with all of the sectors on the overlaid together on the same plot.

Thickness comparisons by method plotted for all seven sectors are shown in figures **6.22** and **6.23**. The difference of the thicknesses over all ice and open water and the average thickness shows a striking feature with the positive values for all sectors except for some negative values during the summers of 1995, 1997, and 1998. These negative values reflect the opening of large leads and polynyas in some sectors at that time period which the averaged thickness value cannot capture. The largest discrepancies occur in the Weddell Sea where the average thickness shows a fairly steady year-round high value for average thickness, and the integrated thickness shows more seasonal variability.

The difference of the thickness from integrating over only ice and the average thickness yields an entirely positive difference plot. Without open water, thickness values are higher year round, yet the integrated thickness value shows a more pronounced seasonal variability when compared with the relatively stable average thickness. This leads to the distinct cyclical pattern in the difference plot; the

differences between the integrated and average thickness are much larger in the summer than at other times of the year.

For the majority of years and sectors, the IT calculation yields the highest yearly maximum value by sector as well as the highest yearly minimum value by sector. ATOW and ITOW minimum values tend to be lower than the AT and IT minimum values due to averaging over the larger water area.

It is interesting to consider where there are agreements in the time of the minimum and maximum thickness values across calculation methods. The week of the year with the maximum ITOW value agrees within three weeks with the maximum ATOW for at least one year in every sector. However, the time of the year with maximum IT tends to occur earlier in the year than the peak AT. This finding reflects the time lag of peak seasons shown in the thickness results by sector.

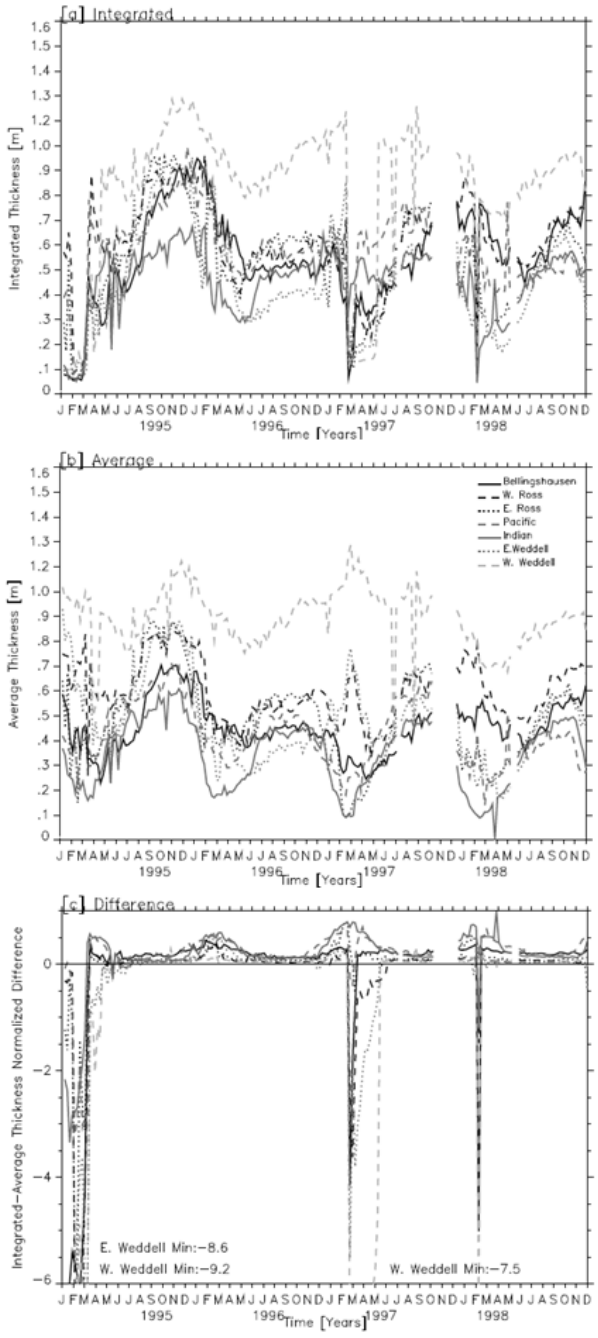

Figure 6.22: Sea ice thickness calculated by including the open water fraction for integrated thickness [a] and the average thickness [b]. The comparison as a difference is shown in [c].

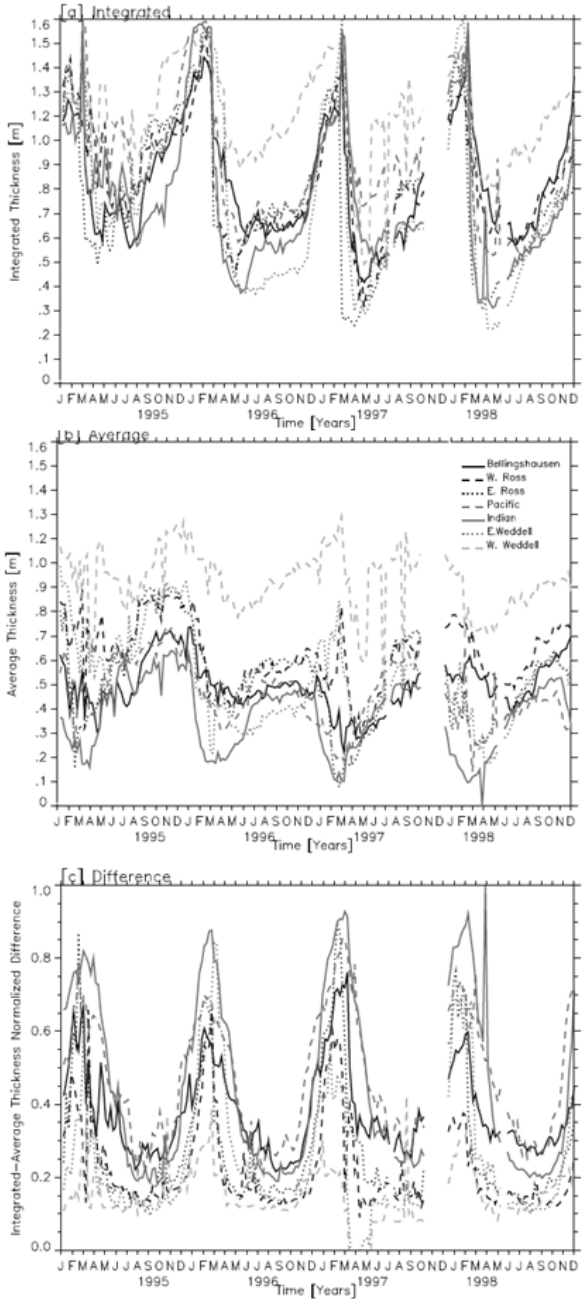

Figure 6.23: Sea ice thickness calculated by including only ice type fractions for integrated thickness [a] and the average thickness [b]. The comparison as a difference is shown in [c].

6.4 Chapter Summary

This chapter examines the effect of calculating integrated thickness versus average thickness for a grid value and considers the impact of including open water in the integrated thickness calculation. The average thickness is a value based on the spatially averaged thickness of the polygons within a grid cell. The integrated thickness is determined from the full thickness distribution for the model grid scaled by percent of sea ice in the model grid cell. There are clear differences in the variability of sea ice thickness based on the calculation method for the same data. Tracking of open water also alters the calculation. Open water refers to the water within the area of all known ice (ice extent), while ice area refers to the study area only including sea ice coverage. Accounting for open water leads to marked differences in thickness calculations, and only the integrated thickness allows tracking of the open water fraction. The evolution of the ice thickness distribution over time is strongly dependent on the open water fraction because that is where the new ice will form. The time lag of the peak sea ice thickness from the integrated thickness calculations with open water to those without suggests that when an accurate measure of the total ice area is available, the integrated thickness without open water per area calculation is the most appropriate method for examining sea ice variability.

Chapter 7

REGIONAL SEA ICE VOLUME IN THE SOUTHERN OCEAN

This chapter addresses the third science question raised in the introduction:

3. What is the overall implication in terms of quantifying sea ice volume over the entire Southern Ocean?

7.1 Sea Ice Volume by Region: Computation and Results

In a sea ice mass balance model, it is necessary to be able to quantify the sea ice volume, and to quantify it correctly. Sea ice volume is an important indicator of regional change in ice mass balance because it accounts for the changes in areal extent as well as thickness. Ice volume accounts for annual ice production and provides records of total ice mass stored a region. Accurate calculations of sea ice volume will help researchers improve their understanding of the rates of change of sea ice volume in the Southern Ocean to enable improved predictions of future sea ice conditions.

The physical area of sea ice in each grid cell may be determined from the NIC ice charts. Because the model grid is circumpolar and demarcated by latitude and longitude instead of equal area, the area of each cell varies with the latitude. The open water fraction of every sea ice polygon in the ice charts is tracked, so the fraction of a grid cell physically covered by ice is known. The area in square meters is the product of the area of the grid cell and the total fraction of the cell covered by ice of any thickness.

The volume is calculated two ways. The first way determines volume as the product of the area and the IT value, and the second way computes volume as the product of the area and the AT value. Unlike the last investigation where the impact of open water fraction on the averaging process was a consideration, in volume determination of ice thickness, the open water contribution plays no role. Thus, the method comparison from chapter six is reduced from a four-case comparison to a two-case comparison of the integrated versus average thickness in volume computations.

The previous calculations on the model grid cell are integrated to the regional scale. The PV-WAVE *where* function searches for all longitudes of cells within each of the seven sectors. A spatial-weighted-average of the grid cell values determines the sector bin values, sector integrated thickness, sector average thickness, and all sector weekly anomalies. These are the weighted-average values per sector area. The total sector volume is just the sum of all the grid cell volume records in the sector.

For plotting purposes, the year dimension is removed, and the week dimension is 208 weeks to reflect four years of data. Combinations of multi-line plots are created to visualize the differences between the methods of determining sea ice volume from NIC ice charts over all sectors.

Accurate sea ice volume is an interesting problem While sea ice area on a regional to basin scale is approximately on the order of millions of square kilometers, sea ice thickness is only on the order of about a meter. This simple fact leads to another question:

Can the large scale thickness variability preserved in the calculations of integrated thickness make a significant difference in the sea ice volume comparison? This question is explored through three graphics: a) the volume from the integrated

thickness and ice chart-derived area for all seven sectors, b) the volume from the average thickness and the same area over all sectors, and c) a normalized difference of volume from the integrated thickness and the volume from the average thickness divided by the integrated thickness. These three plots appear in figure **7.1**.

The graphs [a] and [b] show that volume from integrated thickness is almost always larger than the volume from the average thickness for all sectors. The integrated thickness is almost always larger than the average thickness, and since the area does not change, this volume result is expected. In the graphs of both volume calculations, the Eastern Weddell Sea volume tends to be the greatest for all sectors. This is due to the high fractions of thick ice in that sector, as well as the larger geographic area covered by the Eastern Weddell Sea than the Western Weddell Sea. The Pacific Ocean sector tends to have a lower volume throughout the year. Although this sector spans a wide range of longitude, the continent extends farther to the north in this sector so there is a smaller latitude range. Moreover, the Indian sector shares the same east to west range as the Pacific Ocean sector (70°), because of the continent shape, sea ice may form slightly more towards the south. In the Indian Ocean, maximum sea ice volume is near the maximum for all sectors, and the minimum is near the minimum for all sectors. This wide range in volume may be attributed to ice formation over a large area, but little thick ice retained in the summer. Conversely, sea ice volume in the Bellingshausen-Amundsen Seas exhibits a relatively small range between minimum and maximum volume, perhaps due to the large amount of multi-year thick ice retained in the summer. For all sectors, IT per area consistently peaks in the summer when the total ice area is minimized because mainly thick ice remains. However, AT per area peaks at different times of the year, and varies by sector (see

figure **6.23**). From figure **7.1** it is clear that volume peaks near October (after the winter) for all sectors using both method calculations.

Over large areas of the Southern Ocean, the differences in sea ice thickness by IT and AT calculations appear significant. However, because sea ice thickness and sea ice area are on drastically different scales, the obvious differences in volume from AT and volume from IT are not as apparent. To examine the differences, the normalized difference of the volume calculations is examined (figure **7.1 [c]**). From the normalized difference, it is clear that the effect of thickness calculation on volume may be enormous.

In the summer and early autumn, the normalized difference maximizes around 80-99% depending on the year and the sector. Summer differences in the Weddell Sea are also very large due to the typical large open water fraction in the summer. The integrated thickness tends to account for the higher thick ice fraction so there are large differences in the two calculations. The volume difference is only negative in the Weddell Sea near May 1997. Recall that this is near the time when a larger than normal polynya opened up in the Weddell Sea that has been tied to the strong El Niño year (Ackley et al 2001). Although the differences are greatest in the summer, even in the winter, when the differences are minimized, the normalized difference is still generally larger than 10%. The implication of these results is that the large scale thickness variability preserved in the IT calculations does make a significant difference in the regional sea ice volume.

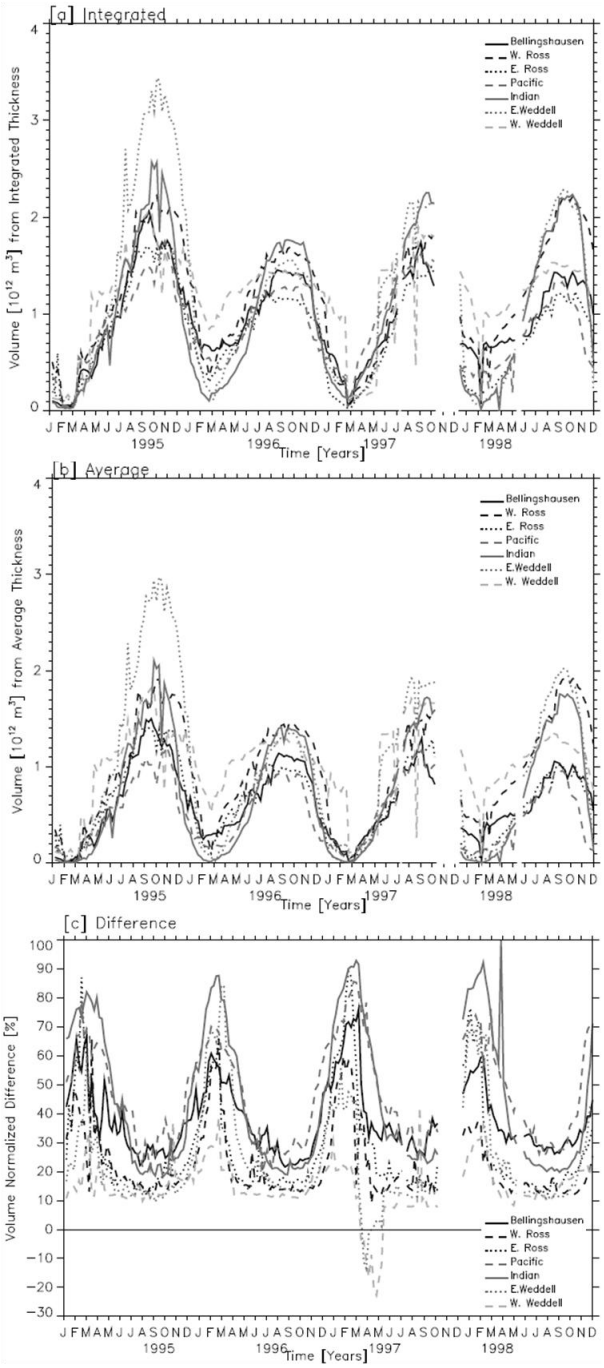

Figure 7.1: Sea ice volume by sector as determined by the integrated thickness [a] and the average thickness [b]. The comparison as a normalized difference of volume calculated from the integrated and average thickness values is shown in [c].

7.2 Chapter Summary

Sea ice volume is calculated as simply the product of the area of the ocean covered by sea ice and a value for sea ice thickness for that area. This work compares volume calculated from average thickness as determined from the mean ice chart thickness by polygon and the area of total ice coverage with volume calculated from integrated thickness of all ice ranges and the same area of total ice coverage.

Regional sea ice area is on the order of millions of square kilometers, but sea ice thickness is around a meter, so it is not immediately apparent that the method of calculating sea ice difference will significantly affect volume. From a normalized difference comparison of the two volume calculations, it is clear that the thickness calculation method has a large impact on volume, particularly in the summer. When the volume from IT is compared with volume from AT visually, the shapes of the volume by region are very similar, but the volume from average thickness is a little lower. The volume calculations have peaks closer to the time of maximum ice extent than maximum sea ice thickness, so it may be assumed that the similar shape of the volume calculations is due to the area value, which is the same for both methods. The normalized difference of the volume calculations, however, peaks in the summer, precisely when both volume calculations are minimized. In the future, it would be interesting to examine when the sea ice volume peaks in comparison to the thickness, area, and extent.

Chapter 8

SUMMARY AND CONCLUSIONS

Sea ice is an important component of the global climate system, yet it is not well parameterized in climate models today. This thesis addresses the need for improved thickness parameterization in sea ice models and studies and develops a framework and set of tools for a Southern Ocean sea ice diagnostic model. This model requires sea ice motion vectors that can be interpolated to the model grid, and static data on sea ice conditions from the NIC ice charts that can be processed, and both made ready as model input. Future work will use this diagnostic model to calculate volume and transport across flux gates on a basin scale.

Although sea ice extent and concentration data are readily available on a basin scale, there is no available archive of sea ice thickness and ice conditions for the entire Southern Ocean. Because accurate thickness measurements are a vital component to mass balance and volume calculations, this thesis focuses on creating a database of Southern Ocean model input-ready sea ice thickness distribution information derived from operational ice charts. The operational ice chart products are developed from composites of remotely sensed images classified by ice analysts, and the charts provide coverage of the Southern Ocean. This thesis details the process by which thickness may be transferred from a polygon GIS file format into more versatile gridded, model-ready data files.

Ice chart-derived sea ice thickness and associated distribution are evaluated by considering three main science questions. The first question asks how the sea ice data from NIC ice charts may be restructured into a format suitable for modeling. This thesis shows that, through geodatabase management and batch geoprocessing with Python scripts, the sea ice thickness data may be stored in a gridded format for models while retaining all of the thickness distribution and open water information as fractions on a sub-grid cell level. Sea ice thickness distribution examples on a weekly temporal scale and a model-grid spatial scale provide a visualization of the model input format. The information is propagated through scales to show the sea ice thickness distribution on a seasonal and regional scale and how it reflects anticipated cycles and patterns (Worby et al 2008).

The second question considers the impact of retaining the ice types and open water fractions through an integrated sea ice thickness calculation and how that differs from the average thickness value calculated directly from the ice charts. This question cannot be addressed without also considering the effect of the open water fraction on the thickness calculation. By tracking the concentration of ice types within the ice extent, the fraction of open water within the ice pack is also preserved. The analysis shows that the integrated thickness value preserves the detail and variability of the thickness distribution identified in the ice charts. The removal of open water from the integrated thickness calculation more accurately reflects the seasonal cycle of the thickness distribution as well as the time of year with he maximum average sea ice thickness per area.

The final question examines Southern Ocean regional sea ice volume. Accurate sea ice area data are available from the product of the fraction of ice in a

given region and the total area of that region, and sea ice thickness data are available from multiple thickness methods. The volume from average thickness is slightly less than the volume from integrated thickness (following the results of the thickness analysis), but the general shape of volume maximum and minimum values throughout the year are the same. Because the regional area is so large compared to the thickness, there is a question of whether the different thickness calculations cause significant variations in sea ice volume. The normalized difference of the two volume calculations shows a massive difference in volume in the summer, as well as differences of over 10% for every sector throughout the year.

This research provides the initial steps for future examination of the major unknown components of sea ice research. Further research to examine the effect of different calculations of thickness on regional volume is needed, but it is beyond the scope of the present study. However, this study frames further work to examine the volume in the Southern Ocean; by adopting the model framework developed for the master's thesis, a diagnostic data-driven Southern Ocean sea ice model will be run with the detailed thickness distribution as input thickness data and drift vectors from the Atlas of Antarctic Sea Ice Drift as sea ice motion data. Analysis of the diagnostic model output will be the initial effort for the doctoral study.

REFERENCES

Ackley, S.F., C.A. Geiger, J.C. King, E.C. Hunke, J. Comiso (2001), The Ronne polynya of 1999/98: observations of air-ice-ocean interaction, *Annals of Glaciology, 33*: 425-9.

Allison, I., 1997. Physical processes determining the Antarctic sea ice environment. Aust. J. Phys. 50 (4), 759–771.

Cavalieri, D. J., C. L. Parkinson, and K. Y. Vinnikov, 30-Year satellite record reveals contrasting Arctic and Antarctic decadal sea ice variability, *Geophys. Res. Lett*., *30*(18), 1970, doi:10.1029/2003GL018031, 2003.

Cavalieri, D. J., and C. L. Parkinson (2008), Antarctic sea ice variability and trends, 1979–2006, J. Geophys. Res., 113, C07004, doi:10.1029/2007JC004564.

Commiso, J.C. and C.W. Sullivan (1986), Satellite Microwave and In Situ Observations of the Weddell Sea Ice Cover and its Marginal Ice Zone, *Geophys. Res. Lett.,91*(C8), 9663-81.

Dedrick, K.R., K. Partington, M.L. Van Woert, C.A. Bertoia, and D. Benner F (2001), U.S. National/Naval digital sea ice data and climatology, Canadian Journal Remote Sensing, 27, 457-475.

Deliberty, T. D., C. A. Geiger, S. F. Ackley, A. P. Worby, M. VanWoert (2011), The annual cycle of sea ice thickness and volume in the Ross Sea, submitted to Deep Sea Research II-SIMBA/SIPEX IPY special volume.

Druker, Robert, Seelye Martin, Richard Moritz. Observations of ice thickness and frazil ice in the St. Lawrence Island polynya from satellite imagery, upward looking sonar, and salinity/ temperature moorings, Journal of Geophysical Research, 108(C5), 3149-3166, 2003.

Emery, W.J., C.W. Fowler, J.A. Maslanik (1997), Satellite-derived maps of Arctic and Antarctic sea ice motion: 1988 to 1994, *Geophys. Res. Lett*., *24*(8), 897-900.

Fetterer, F., compiler. (2006), A Selection of Documentation Related To National Ice Center Sea Ice Charts in Digital Format. NSIDC Special Report 13. Boulder, CO, USA: National Snow and IceData Center. http://nsidc.org/pubs/special/nsidc_special_report_13.pdf

Gloersen, P.; Campbell, W.J.; Cavalieri, D.J.; Comiso, J.C.; Parkinson, C.L.; Zwally, H.J. (1992). Arctic and antarctic sea ice, 1978-1987: Satellite passive-microwave observations and analysis. NASA: Washington, D.C, USA. 290 pp.

Henderson-Sellers, A and k. McGuffie (1987) *A Climate Modeling Primer*. John Wiley & Sons Ltd, pp. 16-102.

Heil, P., C.W. Fowler, J.A. Maslanik, W.J. Emery, I. Allison (2001), A comparison on East Antarctic sea-ice motion derived using drifting buoys and remote sensing, *International Glaciology Society, 33,* 139-44.

Hibler, W.D. (1980), Modeling a Variable Thickness Sea Ice Cover, *Monthly Weather Review, 108*(12), 1943-73.

Holland, M.M., C.M. Bitz, E.C. Hunke, W.H. Lipscomb, J.L. Schramm, 2006. Influence of the Sea Ice Thickness Distribution on Polar Climate in CCSM3, J. Climate 19, 2398-414.

IPCC, 2007: Summary for Policymakers. In: Climate Change 2007: The Physical Science Basis. Contribution of Working Group I to the Fourth Assessment Report of the Intergovernmental Panel on Climate Change [Solomon, S., D. Qin, M. Manning, Z. Chen, M. Marquis, K.B. Averyt, M.Tignor and H.L. Miller (eds.)]. Cambridge University Press, Cambridge, United Kingdom and New York, NY, USA.

Johannessen, O.M. Nansen Centre, Bergen, Norway; V. Alexandrov, Nansen Centre, St. Petersburg, Russia; I.Y. Frolov, S. Sandven, L.H. Pettersson, L.P. Bobylev, Nansen Centre, St. Petersburg, Russia; K. Kloster, V.G. Smirnov, Y.U. Mironov, N.G. Babich (2007), *Remote sensing of Sea Ice in the Northern Sea Route*. Springer, Praxis Publishing Ltd, Chicheser, UK, pp. 149-252.

Kwok, R., G. F. Cunningham, M. Wensnahan, I. Rigor, H. J. Zwally, and D. Yi (2009), Thinning and volume loss of the Arctic Ocean sea ice cover: 2003–2008, J. Geophys. Res., 114, C07005, doi:10.1029/2009JC005312.

Kwok, R., L. Toudal Pedersen, P. Gudmandsen, and S. S. Pang (2010), Large sea ice outflow into the Nares Strait in 2007, Geophys. Res. Lett., 37, L03502, doi:10.1029/2009GL041872.

Martin, Seelye. *An Introduction to Ocean Remote Sensing*. Cambridge University Press. 2004. Cambridge, UK .

Massom, R. A., S. E. Stammerjohn, W. Lefebvre, S. A. Harangozo, N. Adams, T. A. Scambos, M. J. Pook, and C. Fowler (2008), West Antarctic Peninsula sea ice in 2005: Extreme ice compactionand ice edge retreat due to strong anomaly with respect to climate, *J. Geophys. Res., 113*, C02S20, doi:10.1029/2007JC004239.

Parkinson, C.L., D.J. Cavalieri, P. Gloersen, H.J. Zwally, and J.C. Comiso (1999), Arctic sea ice extents, areas, trends, 1978-1996, Journal of Geophysical Research, 104(C9), 20837-20856.

Partington, K., T. Flynn, D. Lamb, C. Bertoia, K. Dedrick, (2003) Late twentieth century Northern Hemisphere sea-ice record from U.S. National Ice Center ice charts, Journal of Geophysical Research, 108(C11), 33343-33350.

Rothrock, D. A. "Ice thickness distribution—Measurement and theory," in *The Geophysics of Sea Ice*, ser. NATO ASI series, Series B: Physics , N. Untersteiner, Ed. New York: Plenum, 1986, vol. 146, pp. 551–575.

Rothrock, D.A., Y. Yu, G.A. Maykut, Thinning of the Arctic Sea Ice Cover, Geophysical Research Letters, 26, 3469-3472, 1999.

Schmitt, C., Ch. Kottmeier, S. Wassermann, M. Drinkwater: Atlas of Antarctic Sea Ice Drift, 2004.The work was performed at the Institut für Meteorologie und Klimaforschung, Universität Karlsruhe by funding of the Deutsche Forschungsgemeinschaft (DFG) Project Ko924/3-1. Published under: http://www.imk.uni-karlsruhe.de/seaiceatlas

Schutz, B. E., H. J. Zwally, C. A. Shuman, D. Hancock, and J. P. DiMarzio (2005), Overview of the ICESat Mission, Geophys. Res. Lett., 32, L21S01, doi:10.1029/2005GL024009.

Stammerjohn, S.E., D.G. Martinson, R.C. Smith, X. Yuan, and D. Rind. Trends in Antartic annual sea ice retreat and advance and their relation to El Nino – Southern Oscillation and Southern Annular Mode variability. JGR 113 C03S90 10.1029/2007JC004269, 2008.

Steig, E. J., D.P. Schneider, S.D. Rutherford, M.E. Mann, J.C. Comiso, D.T. Shindell (2009), Warming of the Antarctic ice-sheet surface since the 1957 International Geophysical Year. *Letters to Nature,457*(22) doi:10.1038/nature07669.

Stroeve, Julienne, Marika M. Holland, Walt Meier, Ted Scambos, and Mark Serreze (2007), Arctic sea ice decline: Faster than forecast. GRL 34, L09501, 10.1029/2007GL029703

Thorndike, A. S., D. A. Rothrock, G. A. Maykut, and R. Colony (1975), The thickness distribution of sea ice, J. Geophys. Res., 80, 4501-4513.

Thorndike, A. S. (1992), Estimates of Sea Ice Thickness Distribution Using Observations and Theory, J. Geophys. Res., 97, 9401-9410.

Vaughan, D. G., G. J. Marshall,W. M. Connolley, C. Parkinson, R. Mulvaney, D. A. Hodgson, J. C. King, C. J. Pudsey, and J. Turner (2003), Recent rapid regional climate warming on the Antarctic Peninsula, Clim. Change, 60,243–274.

Wadhams, Peter (2000), *Ice in the Ocean*. Gordon and Breach Science Publishers, Australia, 351 pages.

Wang, M., and J. E. Overland (2009), A sea ice free summer Arctic within 30 years?, Geophys. Res. Lett., 36, L07502, doi:10.1029/2009GL037820.

Washington, W.M and C.L. Parkinson (2004) *An Introduction to Three-Dimensional Climate Modeling*. 2nd ed. University Science Books, Sausalito, California. pp.353.

Wassermann, S., C. Schmitt, C. Kottmeier, and I. Simmonds (2006), Coincident vortices in Antarctic wind fields and sea ice motion, Geophys. Res. Lett., 33, L15810, soi:10.1029/2006GL026005.

Worby, A. P., C. A. Geiger, M. J. Paget, M. L. Van Woert, S. F. Ackley, and T. L. DeLiberty (2008), Thickness distribution of Antarctic sea ice, *J. Geophys. Res., 113,* C05S92, doi:10.1029/2007JC004254.

Worby, A.P., *Observing Antarctic Sea Ice: A practical guide for conducting sea ice observations from vessels operating in the Antarctic pack ice*. A CD-ROM produced for the Antarctic Sea Ice Processes and Climate (ASPeCt) program of the Scientific Committee for the Antarctic Research (SCAR) Global Change and the Antarctic (GLOCHANT) program, Hobart, Australia, 1999.

World Meteorological Organization (WMO) (1970), WMO Sea Ice Nomenclature, Volume 1: Terminology and Codes, World Meteorological Organization, report 259, Geneva, Switzerland